

# Oil & Natural Gas Technology

DOE Award No.: DE-FC26-06NT42666

## Final Technical Report

# Comparative Assessment of Advanced Gas Hydrate Production Methods

Submitted by:  
Battelle Pacific Northwest Division  
Richland , WA

Prepared for:  
United States Department of Energy  
National Energy Technology Laboratory

July, 2009



Office of Fossil Energy

# **Comparative Assessment of Advanced Gas Hydrate Production Methods**

**Final Technical Report  
Reporting Period March 1, 2006 through June 30, 2009**

M. D. White  
B. P. McGrail  
S. K. Wurstner

July 2009

Cooperative Agreement DE-FC26-06NT42666

Battelle Pacific Northwest Division  
P. O. Box 999  
Richland, Washington 99352

Prepared for  
National Energy Technology Laboratory  
3610 Collins Ferry Road  
P.O. Box 880  
Morgantown, WV 26507-0880





**DISCLAIMER**

This report was prepared as an account of activities sponsored by an agency of the United States Government. Neither the United States Government nor any agency thereof, nor any of their employees, makes any warranty or representation, express or implied, or assumes any legal liability or responsibility for the accuracy, completeness, or usefulness of any information, apparatus, product, or process disclosed, or represents that its use would not infringe privately owned rights. Reference herein to any specific commercial product, process, or service by trade name, trademark, manufacturer, or otherwise, does not necessarily constitute or imply its endorsement, recommendation, or favoring by the United States Government or any agency thereof. The views and opinions of authors expressed herein do not necessarily state or reflect those of the United States Government or any agency thereof.

Furthermore, Battelle assumes no liabilities with respect to the use of, or for damages resulting from the use of, any information, apparatus, process, or composition disclosed in this report.



This document was printed on recycled paper.

(9/2003)





## Abstract

Displacing natural gas and petroleum with carbon dioxide is a proven technology for producing conventional geologic hydrocarbon reservoirs, and producing additional yields from abandoned or partially produced petroleum reservoirs. Extending this concept to natural gas hydrate production offers the potential to enhance gas hydrate recovery with concomitant permanent geologic sequestration. Numerical simulation was used to assess a suite of carbon dioxide injection techniques for producing gas hydrates from a variety of geologic deposit types. Secondary hydrate formation was found to inhibit contact of the injected CO<sub>2</sub> regardless of injectate phase state, thus diminishing the exchange rate due to pore clogging and hydrate zone bypass of the injected fluids. Additional work is needed to develop methods of artificially introducing high-permeability pathways in gas hydrate zones if injection of CO<sub>2</sub> in either gas, liquid, or micro-emulsion form is to be more effective in enhancing gas hydrate production rates.



## Mathematical Symbols and Nomenclature

$D$  is the diffusion coefficient of component  $i$  in phase  $\gamma$ ,  $\text{m}^2/\text{s}$   
 $\mathbf{D}_h$  is the hydraulic dispersion coefficient tensor of phase  $\gamma$ ,  $\text{m}^2/\text{s}$   
 $\mathbf{F}$  is the diffusive heat flux vector,  $\text{W}/\text{m}^2$   
 $g$  is the acceleration of gravity,  $\text{m}/\text{s}^2$   
 $h$  is the enthalpy of phase  $\gamma$  or solid  $s$ ,  $\text{J}/\text{kg}$   
 $i$  is the mass component ( $w$  = water,  $a$  = carbon dioxide,  $o$  = methane,  $s$  = inhibitor)  
 $\mathbf{J}$  is the mass flux diffusive/dispersive flux rate vector of component  $i$ ,  $\text{kg}/\text{m}^2 \text{ s}$   
 $\mathbf{k}$  is the intrinsic permeability tensor,  $\text{m}^2$   
 $k$  is the thermal conductivity of phase  $\gamma$ ,  $\text{W}/\text{m K}$   
 $k_r$  is the relative permeability of phase  $\gamma$   
 $K_h$  is the kinetic guest molecule exchange rate constant,  $\text{kg}/\text{Pa s}$   
 $m$  is the volumetric mass generation rate of component  $i$ ,  $\text{kg}/\text{m}^3 \text{ s}$   
 $M$  is the molecular weight of phase  $\gamma$  or component  $i$ ,  $\text{kg}/\text{kmol}$   
 $\mathbf{n}$  is the surface-normal outward unit vector  
 $P$  is the pressure of phase  $\gamma$ ,  $\text{Pa}$   
 $q$  is the volumetric heat generation rate,  $\text{W}/\text{m}^3$   
 $s$  is saturation of phase  $\gamma$   
 $t$  is time,  $\text{s}$   
 $T$  is temperature,  $\text{C}$   
 $u$  is the internal energy of phase  $\gamma$  or solid  $s$ ,  $\text{J}/\text{kg}$   
 $V$  is volume,  $\text{m}^3$   
 $\mathbf{V}$  is volumetric flux vector of phase  $\gamma$ ,  $\text{m}/\text{s}$   
 $\mathbf{z}$  is the unit gravitational vector  
 $\beta$  is the interfacial scaling factor  
 $\gamma$  is the phase ( $l$  = aqueous,  $g$  = gas,  $n$  = liquid  $\text{CO}_2$ ,  $h$  = hydrate,  $i$  = ice,  $p$  = salt)  
 $\Gamma$  is the surface area,  $\text{m}^2$   
 $\mu$  is the viscosity of phase  $\gamma$ ,  $\text{Pa s}$   
 $\rho$  is density of phase  $\gamma$ ,  $\text{kg}/\text{m}^3$   
 $\sigma$  is the interfacial surface tension,  $\text{N}/\text{m}$   
 $\tau$  is the tortuosity factor of phase  $\gamma$   
 $\varphi$  is the gas mass fraction of  $\text{CH}_4$  of hydrate formers  
 $\phi$  is diffusive porosity  
 $\chi$  is the mole fraction of component  $i$  in phase  $\gamma$   
 $\Psi$  is the gas entry pressure,  $\text{Pa}$   
 $\omega$  is mass fraction of component  $i$  in phase  $\gamma$



## Table of Contents

Abstract .....	v
Mathematical Symbols and Nomenclature .....	vii
Executive Summary.....	xv
1.0 Introduction .....	1.1
1.1 Technical Assessment.....	1.2
1.1.1 Thermal Stimulation .....	1.3
1.1.2 Depressurization .....	1.3
1.1.3 Inhibitor Injection .....	1.4
1.1.4 Gas Injection .....	1.4
1.1.5 Classification of Gas Hydrate Deposits.....	1.6
1.2 Hydrate Guest Molecule Exchange.....	1.6
1.3 Report Organization .....	1.7
2.0 STOMP-HYD .....	2.1
2.1 Conservation Equations.....	2.1
2.2 Constitutive Equations .....	2.4
2.3 Specifications.....	2.8
2.3.1 Initial Conditions .....	2.8
2.3.2 Boundary Conditions.....	2.9
2.3.3 Output .....	2.10
2.4 Development Chronology .....	2.11
2.4.1 STOMP-HYD <sub>1</sub> .....	2.11
2.4.2 STOMP-HYD <sub>2</sub> .....	2.12
2.4.3 STOMP-HYD <sub>3</sub> .....	2.12
2.5 Kinetic Exchange Option.....	2.13
3.0 Class 1 and 2 Gas Hydrate Accumulations .....	3.1
3.1 Simulation Scenarios.....	3.3
3.1.1 System Initialization .....	3.4
3.1.2 Simulation Stages .....	3.4
3.2 Simulation Results.....	3.8
3.2.1 Combined Hydrate- and Gas-Zone Injection Scenarios .....	3.8
3.2.2 Hydrate-Zone Only Injection Scenarios [S19 through S36].....	3.19
4.0 Class 3 Gas Hydrate Accumulations.....	4.1
4.1 Simulation Scenarios.....	4.1
4.2 Simulation Results.....	4.2
4.2.1 Pure CO <sub>2</sub> Injection [R1 through R6] .....	4.4

4.2.2	50% Volumetric CO <sub>2</sub> Micro-emulsion Injection [R7 through R12] .....	4.6
4.2.3	Dissolved CO <sub>2</sub> Injection [R13 through R18] .....	4.8
5.0	Class 4 Gas Hydrate Accumulations.....	5.1
6.0	Conclusions.....	6.1
6.1	Conclusions for Class 1 and 2 Gas Hydrate Accumulations.....	6.1
6.2	Conclusions for Class 3 Gas Hydrate Accumulations .....	6.3
6.3	Conclusions for Class 4 Gas Hydrate Accumulations .....	6.3
7.0	References.....	7.1
	Appendix A.....	A.1

## Figures

2.1. CH <sub>4</sub> Hydrate Equilibrium Data Comparisons .....	2.6
2.2. CO <sub>2</sub> Hydrate Equilibrium Data and Hydrate Number Comparisons .....	2.7
2.3. Mixed CO <sub>2</sub> -CH <sub>4</sub> Hydrate Equilibrium Data.....	2.7
3.1 Gas hydrate saturation and thickness maps of the D (left) and C (right) gas-hydrate bearing sands. Faults are shown as map offsets (Zhu and Phale, 2005). .....	3.2
3.2. Produced water, produced methane, and evolved methane following depressurization at 4 MPa for 1 year across the hydrate and gas zones [S-0]. .....	3.6
3.3. Gas saturation after depressurization at 4 MPa for 6 months at both ends across the gas and hydrate zones [S0]......	3.9
3.4. Hydrate saturation after depressurization at 4 MPa for 6 months at both ends across the gas and hydrate zones [S0]. .....	3.9
3.5. Produced water, produced methane, and evolved methane during pure CO <sub>2</sub> injection at 6 MPa across the hydrate and gas zones, producing at 4 MPa across the hydrate zone only, initiated from the 6-month depressurization stage at 4 MPa [S1 and S4]......	3.11
3.6. Liquid CO <sub>2</sub> saturation profile in the hydrate and gas zones after pure CO <sub>2</sub> injection at 6 MPa at 20°C for 6 months across the hydrate and gas zones, producing at 4 MPa across the hydrate zone only after the 6-month depressurization stage at 4 MPa [S1]......	3.12
3.7. "CO <sub>2</sub> fraction of formers" profile in the hydrate and gas zones after pure CO <sub>2</sub> injection at 6 MPa at 50° for 6 months across the hydrate and gas zones, producing at 4 MPa across the hydrate zone only after the 6-month depressurization stage at 4 MPa [S4]......	3.12
3.8. Liquid CO <sub>2</sub> profile in the hydrate and gas zones after pure CO <sub>2</sub> injection at 10 MPa at 50°C for 0.3 days across the hydrate and gas zones, producing at 4 MPa across the hydrate zone only after the 6-month depressurization stage at 4 MPa [S6]......	3.13
3.9. Produced water, produced methane, and evolved methane during 50% volumetric CO <sub>2</sub> micro-emulsion injection at 6 MPa across the hydrate and gas zones, producing at 4 MPa across the hydrate zone only after the 6-month depressurization stage at 4 MPa [S7 and S10]......	3.14
3.10. Gas saturation profile in the hydrate and gas zones after 50% volumetric CO <sub>2</sub> micro-emulsion injection at 6 MPa at 50° C for 6 months across the hydrate and gas zones, producing at 4 MPa across the hydrate zone only after the 6-month depressurization stage at 4 MPa [S10]......	3.15
3.11. "CO <sub>2</sub> hydrate saturation" profile in the hydrate and gas zones after 50% volumetric CO <sub>2</sub> micro-emulsion injection at 6 MPa at 50° C for 6 months across the hydrate and gas zones, producing at 4 MPa across the hydrate zone only after the 6-month depressurization stage at 4 MPa [S10]. .....	3.15
3.12. "CO <sub>2</sub> fraction of formers" profile in the hydrate and gas zones after 50% volumetric CO <sub>2</sub> micro-emulsion injection at 6 MPa at 50° C for 6 months across the hydrate and gas zones, producing at 4 MPa across the hydrate zone only after the 6-month depressurization stage at 4 MPa [S10]. .....	3.16
3.13. Liquid-CO <sub>2</sub> saturation profile in the hydrate and gas zones after 50% CO <sub>2</sub> volumetric micro-emulsion injection at 10 MPa at 50° C for 0.15 years across the hydrate and gas zones, producing at 4 MPa across the hydrate zone only after the 6-month depressurization stage at 4 MPa [S12]......	3.16

3.14. Produced water, produced methane, and evolved methane during dissolved CO <sub>2</sub> injection at 6, 8, and 10 MPa across the hydrate and gas zones, producing at 4 MPa across the hydrate zone only after the 6-month depressurization stage at 4 MPa [S13, S14, S16, S17, and S18].....	3.18
3.15. Hydrate saturation profile in the hydrate and gas zones after dissolved CO <sub>2</sub> injection at 6 MPa at 20° C for 6 months across the hydrate and gas zones, producing at 4 MPa across the hydrate zone only after the 6-month depressurization stage at 4 MPa [S13] .....	3.19
3.16. Produced water, produced methane, and evolved methane during pure CO <sub>2</sub> injection at 6 MPa across the hydrate zone only, producing at 4 MPa across the hydrate zone only, initiated from the 6-month depressurization stage at 4 MPa [S19 and S22].....	3.20
3.17. "CO <sub>2</sub> hydrate saturation" profile in the hydrate and gas zones after 50% volumetric CO <sub>2</sub> micro-emulsion at 6 MPa at 50° C for 6 months across the hydrate zone only, producing at 4 MPa across the hydrate zone only after the 6-month depressurization stage at 4 MPa [S28].....	3.21
3.18. Produced water, produced methane, and evolved methane during dissolved CO <sub>2</sub> injection at 6, 8, and 10 MPa across the hydrate zone only, producing at 4 MPa across the hydrate zone only after the 6-month depressurization stage at 4 MPa [S31, S34, S35, and S36].....	3.22
4.1. Produced water, produced methane, and evolved methane following depressurization at 4 MPa for 1 year across the hydrate zone [R0].....	4.3
4.2. Gas saturation after depressurization at 4 MPa for 6 months across hydrate zone [R0]. .....	4.4
4.3. Hydrate saturation after depressurization at 4 MPa for 6 months at both ends across hydrate zone [R0].....	4.4
4.4. Produced water, produced methane, and evolved methane during pure CO <sub>2</sub> injection at 20° C, 6 MPa and 10 MPa, producing at 4 MPa, initiated from the 6-month depressurization stage at 4 MPa [R1 and R3].....	4.5
4.5. "CO <sub>2</sub> fraction of formers" profile after injection of pure CO <sub>2</sub> at 10 MPa at 20° C for 6 months, producing at 4 MPa, initiated from the 6-month depressurization stage [R3]. .....	4.6
4.6. "Hydrate saturation" profile after injection of pure CO <sub>2</sub> at 10 MPa at 20° C for 6 months, producing at 4 MPa, initiated from the 6-month depressurization stage [R3].....	4.6
4.7. Produced water, produced methane, and evolved methane during 50% volumetric CO <sub>2</sub> micro-emulsion at 20° C, 6 MPa, 8 MPa, and 10 MPa, producing at 4 MPa, initiated from the 6-month depressurization stage at 4 MPa [R7 – R11]. .....	4.7
4.8. "CO <sub>2</sub> hydrate saturation" profile after injection of 50% volumetric CO <sub>2</sub> micro-emulsion at 6 MPa at 50° C for 6 months, producing at 4 MPa, initiated from the 6-month depressurization stage [R10]. .....	4.8
4.9. "Hydrate saturation" profile after injection of 50% volumetric CO <sub>2</sub> micro-emulsion at 6 MPa at 50° C for 6 months, producing at 4 MPa, initiated from the 6-month depressurization stage [R10].	4.8
4.10. Produced water, produced methane, and evolved methane during dissolved CO <sub>2</sub> injection at 20° and 50° C, 6 MPa, 8 MPa, and 10 MPa, producing at 4 MPa, initiated from the 6-month depressurization stage at 4 MPa [R13 – R18].....	4.9
4.11. Gas saturation profile after injection of dissolved-CO <sub>2</sub> at 6 MPa at 50° C for 6 months, producing at 4 MPa, initiated from the 6-month depressurization stage [R16]. .....	4.10
4.12. "CO <sub>2</sub> hydrate saturation" profile after injection of dissolved-CO <sub>2</sub> at 6 MPa at 50° C for 6 months, producing at 4 MPa, initiated from the 6-month depressurization stage [R16].....	4.10

6.1. Summary of simulation results of class 1 hydrate accumulations.....	6.2
--	-----

## Tables

2.1 Primary variable sets and ancillary equations. ....	2.3
2.2. STOMP-HYDk primary variable sets and ancillary equations.....	2.15
3.1. Class 1 Gas Hydrate Accumulation Simulation Scenarios.....	3.7
4.1. Class 3 Gas Hydrate Accumulation Simulation Scenarios.....	4.1



## Executive Summary

The vast amounts of natural gas hydrates in geologic oceanic and permafrost accumulations make them an attractive hydrocarbon fuel resource for the future. The fraction of this resource that becomes available for utilization strongly depends on the production techniques used to extract natural gas from the clathrate structure. The petroleum industry has the technology to produce geologic accumulations of gas hydrates in both oceanic and permafrost settings, but the ratio of consumed energy from production to potential energy extracted from the gas at many locations could exceed one. This project was undertaken to explore alternative technologies for geologic gas hydrate production that could reduce the input energy required for commercial-scale operations. A technical assessment completed at the beginning of the project concluded that the more conventional technologies of thermal stimulation, depressurization, and inhibitor injection had shortcomings. Thermal stimulation suffers from poor recovery efficiencies and could possibly disrupt the hydraulic and mechanical properties of the produced reservoir. Depressurization is the most promising and efficient of the three, but ultimately requires heat transfer from the surrounding environment to support long-term production and could possibly disrupt the mechanical stability of the reservoir. Inhibitor injection, the least favorable option, is unattractive for economic, environmental, and mechanical stability reasons.

Displacing natural gas and petroleum with carbon dioxide is a proven technology for producing conventional geologic hydrocarbon reservoirs, and producing additional yields from abandoned or partially produced petroleum reservoirs. Extending this concept to natural gas hydrate production is attractive from four perspectives: 1) methane and carbon dioxide both form sl hydrates, providing opportunities for geomechanical stability; 2) thermodynamic equilibrium pressures for pure carbon dioxide and methane hydrates cross around 10.5° C, providing opportunities for innovative production concepts; 3) the heat of formation for pure carbon dioxide hydrates is greater than that for pure methane hydrates; making the guest molecule exchange thermodynamically favored; and 4) forming CO<sub>2</sub> hydrates provides geologic sequestration opportunities. This study used numerical simulation to assess a suite of carbon dioxide injection techniques (i.e., aqueous saturated, micro-emulsion, pure phase) for producing gas hydrates from a variety of geologic deposit types. The injection and production approaches were modeled after petroleum industry standards, using injection and extraction wells. There are two distinct approaches for producing geologic gas hydrates with CO<sub>2</sub> injection: 1) dissociation-reformation, and 2) direct guest molecule exchange. The dissociation-reformation approach uses elevated injectant temperatures to first dissociate the methane hydrate. Carbon dioxide hydrate is then reformed as the geologic formation returns to ambient temperatures. Whereas the dissociation-reformation approach ultimately results in carbon dioxide hydrate replacing methane hydrate, it requires an energy source to elevate the injectant temperature and requires maintenance of mechanical stability of the formation during the dissociation and reformation process. The direct-guest-molecule-exchange approach requires contact between the incoming guest and the resident gas hydrate. These numerical investigations have demonstrated how secondary hydrate formation inhibits this contact, thus diminishing the exchange rate. Straightforward application of petroleum industry approaches to implementing the guest-molecule-exchange production technology for geologic gas hydrates is hindered by secondary hydrate formation, pore clogging, and hydrate zone bypass of the injected fluids. The study did not address alternative injection concepts that could include formation fracturing and diffusive processes and allowances for post production gas separation (i.e., separation of produced methane and breakthrough carbon dioxide). Additional work is needed to develop methods of artificially introducing high-permeability pathways in gas hydrate zones if injection of CO<sub>2</sub> in either gas, liquid, or micro-emulsion form is to be more effective in enhancing gas hydrate production rates.



## 1.0 Introduction

In recognition of the technical challenges associated with producing natural gas hydrate accumulations, this project was devised to investigate and assess innovative production approaches. About one decade ago, publications by Ohgaki et al. (1996) for methane ( $\text{CH}_4$ ) hydrate and Nakano et al. (1998) for ethane ( $\text{C}_2\text{H}_6$ ) hydrates introduced a production concept that involved exchanging carbon dioxide ( $\text{CO}_2$ ) with the indigenous clathrate hydrate guest molecule. About five years ago, McGrail et al. (2004) broadened the guest molecule exchange concepts into a production process, termed the Enhanced Gas Hydrate Recovery (EGHR) process, that involved an innovative scheme for producing aqueous micro-emulsions of liquid  $\text{CO}_2$  and injecting the micro-emulsion into the gas hydrate formation. The scheme involves injecting the micro-emulsion at a temperature above the stability point for  $\text{CH}_4$  hydrate, decomposing its crystalline lattice and releasing the enclathrated gas. Formation of  $\text{CO}_2$  hydrate then occurred as the reservoir cooled through heat transfer to a point below the stability point for  $\text{CO}_2$  hydrate. A final report on the EGHR process was recently published (McGrail et al., 2007).

These EGHR process investigations (McGrail et al., 2007) included laboratory-scale experiments that demonstrated the micro-emulsion injection production concepts with  $\text{CH}_4$  hydrate-bearing sediments. Whereas these laboratory-based studies yielded encouraging results, the technology concepts would remain a laboratory curiosity unless work was performed to scale up the process and develop viable injection and production strategies. During the EGHR process, natural gas hydrate is dissociated via thermal stimulation, the produced gas is displaced by the injected micro-emulsion, and  $\text{CO}_2$  hydrate forms in the reservoir with restitution of the thermal environment. Whereas this process ultimately restores a sl (i.e., structure I (Sloan and Koh, 2007)) hydrate within the reservoir pore space, it leaves the production portion of the reservoir without hydrate for a period of time. Another option for implementing the guest-molecule-exchange-concept is to take advantage of the gas hydrate surface areas in geologic media, where the gas hydrate is pore filling, directly exchanging the gas hydrate guest molecules without dissociation. This option for production follows the original concepts of Ohgaki et al. (1996) and Nakano et al. (1998), where pure  $\text{CO}_2$  gas was injected. Alternatively, the direct guest-molecule-exchange approach could be implemented for  $\text{CO}_2$  concentrations ranging from aqueous solutions with dissolved  $\text{CO}_2$ , through increasing volume ratios of aqueous micro-emulsions, to pure  $\text{CO}_2$ . Likewise, the state of the pure phase  $\text{CO}_2$  can vary from liquid  $\text{CO}_2$ , to subcritical gaseous  $\text{CO}_2$ , to supercritical gaseous  $\text{CO}_2$ .

The principal objectives of this project were to compare and contrast EGHR and other  $\text{CO}_2$ -based processes for the production of gas hydrates with each other and the more conventional methods (i.e., thermal stimulation and depressurization) at field scales. To accomplish these objectives without conducting expensive pilot-scale production tests or using laboratory-scale analogs, the investigations were strictly computational, using numerical simulation. In developing this project, it was envisioned that the numerical simulation results would form the basis for an evaluation of the merits and drawbacks to the various production processes, from an energy balance (i.e., consumed versus produced energy) and reservoir engineering perspectives. We view this as an essential intermediate step that is required before substantial U.S. Department of Energy (DOE) and industry investment is made in the design, engineering, manufacturing, and testing of a full-scale down-hole tool suitable for field deployment in pilot-scale production tests.

During the course of these investigations simulation results were generated that were not fully anticipated at the start of the project. In particular, the importance of secondary hydrate formation

during the production process was not foreseen. In the research management plan developed for this project, the stated objectives were to:

1. evaluate optimum injection strategies to produce methane from natural gas hydrate deposits using the newly developed EGHR process and other production concepts utilizing CO<sub>2</sub>,
2. compare and contrast energy balance and gas production rates of the unconventional methods with conventional methods of depressurization and thermal stimulation, and
3. provide sufficient information on which to judge whether proceeding into pilot phase demonstrations with any of the innovative production methods is warranted on a gas hydrate prospect.

Having conducted this research, a fourth objective of exploring alternative injection strategies, such as those involving advective flow through induced fractures and diffusive flow through the hydrate-bearing matrix, has become evident. A preliminary project task was to perform a technology status assessment and submit a summary report describing the current state of information and/or technology relevant to the proposed work. The text of this report is included in the Technical Assessment sections that follow.

## 1.1 Technical Assessment

Vast quantities of natural gas are held in hydrate form in geologic reservoirs in sub-oceanic sediments and arctic permafrost zones (Kvenvolden, 1988; Sloan, 1997), where conditions of high pressure and low temperature are within the hydrate stability region. In 1995, the U.S. Geological Survey (USGS) conducted a study to assess the quantity of natural gas hydrate resources in the United States and found that the estimated quantity exceeded known conventional domestic gas resources (Collett, 2004). Recovery of natural gas from these hydrate-bearing deposits has the potential for being economically viable (Circone et al., 2005b; Collett, 2004; Moridis et al., 2004), but there remain significant technical challenges in converting these natural deposits into useable reserves (Collett, 2004). In conventional reservoirs, natural gas migrates to the recovery point via pressure gradients. For these reservoirs the recovery rate is a function of the formation permeability and pressure gradients between the reservoir and recovery point. Natural gas recovery from hydrate-bearing deposits requires the additional energetic cost of dissociating the hydrate structure. A variety of methods have been proposed for producing natural gas from hydrate deposits: 1) thermal stimulation, where the temperature is increased above the hydrate stability region; 2) depressurization, where the pressure is decreased below the hydrate stability region; 3) chemical injection of inhibitors, where the temperature and pressure conditions for hydrate stability are shifted; and 4) CO<sub>2</sub> or mixed CO<sub>2</sub> and N<sub>2</sub> exchange, where CO<sub>2</sub> and N<sub>2</sub> replace CH<sub>4</sub> in the hydrate structure. It is critical to note that although recent estimates (Milkov et al., 2003) put the global accumulations of natural gas hydrate at 3,000 to 5,000 trillion cubic meters (TCM), compared against 440 TCM estimated (Collett, 2004) for conventional natural gas accumulations, none have speculated how much gas could be produced from these vast natural gas hydrate deposits. What is needed to convert these gas-hydrate accumulations to energy reserves are technological innovations, sparked through sustained scientific research and development. As with other unconventional energy resources, the challenge is to first understand the resource, its coupled thermodynamic and transport properties, and then to address its production challenges.

A critical consideration for the production of gas hydrates is the thermal self-regulation of hydrate dissociation. If the hydrate-bearing reservoir is above the freezing point of the formation water, then the temperature in the vicinity of dissociation will decrease because heat flow into the region is insufficient to offset the endothermic heat of dissociation. With continued dissociation, the tem-

perature will decrease until the hydrate is exhausted or the temperature reaches a phase boundary. In the absence of other heat sources (e.g., advective, electromagnetic), the system becomes thermally self-regulating, the temperature remains constant, and the dissociation rate is controlled by diffusive heat transfer. For pressures above the quadruple point (the intersection of the hydrate stability boundary and the formation water freezing point temperature) the lower temperature limit will be that of the hydrate equilibrium boundary. For lower pressures, temperature is limited by the freezing point of the formation water. Laboratory experiments (Circone et al., 2005a) have shown that under these conditions, dissociation rates are not slowed by ice formation and are dependent on heat flow into the dissociation zone from the surroundings, and the exothermic heat of formation of the ice contributes to the heat flow into the dissociation area. When the hydrate-bearing formation is below the freezing point of the formation water, however, the dissociation rates are considerably slower (Circone et al., 2005a).

### **1.1.1 Thermal Stimulation**

Gas hydrate production via thermal stimulation recently has been investigated experimentally (Tang et al., 2005) and numerically (Moridis, 2003, 2004; Moridis et al., 2004; Pooladi-Darvish, 2004; Tsyphkin, 2000). Technologies for implementing thermal stimulation include hot brine injection, steam injection, cyclic steam injection, fire flooding, and electromagnetic heating. Steam injection, cyclic steam injection and fire flooding suffer from high heat losses and the by-products of fire flooding can dilute the produced natural gas. Hot brine injection involves the injection of a saline aqueous solution at an elevated temperature into a gas hydrate-bearing geologic reservoir. The energy of the injected brine is used to heat the geologic media, heat dissociated gas and aqueous phases, and dissociate gas hydrate. In general, brine flow rates yield a heating process that is dominantly advective. In addition to raising the boiling temperature of the saline solution, the dissolved salt lowers the gas hydrate dissociation temperature. Visual experiments of the dissociation process (Tohidi et al., 2001) in glass micro-models indicate that during the dissociation process the hydrate becomes colloidal and migrates advectively with the injected brine. Production experiments of Tang et al. (2005) indicate that the efficiency of the hot brine injection production methodology is dependent on the inlet brine temperature, injection rate, and initial hydrate saturation; where the measure of efficiency is the energy ratio, defined as the ratio of combustion heat of the produced gas over the inlet heat. Tang et al. (2005) concluded that lower temperatures and injection rates yield higher recovery energy ratios, as did higher initial hydrate saturations. The downside of higher energy ratios realized through lower inlet temperatures and injection rates, however, are the lower production rates. Energy ratios for moderate to high temperatures and injection rates are on the order of 1.0, which means 50% of the recovered energy would be used to heat the injected brine. Numerical simulations of Moridis (2002, 2003) have demonstrated that the appeal of the thermal stimulation technology increases from Class 1 to Class 3 hydrate deposits (see Classification of Gas Hydrate Deposits). Another class of thermal stimulation technologies involves the injection of two fluids that react exothermally when mixed, such as the acidic- and basic-liquid approach proposed by Chatterji and Griffith (1988). The reaction of these two aqueous solutions would yield a hot salt solution.

### **1.1.2 Depressurization**

Gas hydrate production via depressurization is considered to be the most economically promising technology (Collett, 2004). The Messoyakha field in northern Russia is a natural gas accumulation, containing both free gas and hydrate-bearing formations, which has been produced by simple depressurization. The sustained production of natural gas from this field is due to the dissociation of

gas hydrate into an underlying free-gas formation, and has demonstrated that gas hydrates are immediately producible using conventional methods. However, production rates are ultimately controlled by heat transfer toward the hydrate dissociation region. Gas production using depressurization at the Mallik site was numerically simulated (Moridis et al., 2004) as part of a study to analyze various production methods. These simulations assumed a geothermal gradient of  $0.03^{\circ}\text{C}/\text{m}$  across the hydrate-bearing formation. The simulation results for a single vertical production well show temperatures dropping in response to depressurization of the formation and hydrate dissociation. The temperature decrease, however, is reversed as deeper warmer water is drawn to the well, providing the needed energy to sustain hydrate dissociation in the depressurized system. When augmented with either steam or hot methane ( $\text{CH}_4$ ) gas injection from a second well, natural gas production is superior in terms of the ratios of produced gas to water and fraction of produced hydrate  $\text{CH}_4$ . Numerical depressurization studies for a one-dimensional radial confined reservoir with a central well were conducted using a linearization model (Ji et al., 2001). These studies represent depressurization in its most basic configuration. As expected, simulation results indicate that hydrate dissociation rates and associated gas production rates are controlled by the far-field reservoir pressure and temperature, via energy supplied by natural gas advected from the far field to the dissociation front. Laboratory experimental studies of gas hydrate production via depressurization (Liu et al., 2002; Sung et al., 2003) have been limited in number and scope. Because of the thermal self-regulation of gas hydrates, pure depressurization is a viable option for natural accumulations of gas hydrates, but may suffer from slow production rates. Sustained production using depressurization additionally requires a heat source. At the Messoyakha field, that energy source is likely heat transfer into the dissociation zone via thermal conduction and advection, which ultimately controls the production rate.

### **1.1.3 Inhibitor Injection**

Thermodynamic inhibitors lower the hydrate formation temperature, which can result in hydrate dissociation when injected into a gas-hydrate-bearing formation. The most common thermodynamic organic inhibitors are methanol, monoethylene glycol (MEG) and di-ethylene glycol (DEG) commonly referred to as glycol. Dissolved salts (e.g.,  $\text{NaCl}$ ,  $\text{CaCl}_2$ ,  $\text{KCl}$ ,  $\text{NaBr}$ ) can also be inhibitors. Whereas gas hydrate inhibitors are an effective methodology for preventing hydrate formation in engineering applications, their use in the production of natural gas hydrates is prohibitive from three perspectives: 1) environmental impact, 2) economic costs, and 3) thermal self-regulation of gas hydrates.

### **1.1.4 Gas Injection**

The world's energy consumption is expected to increase by 40% (Goel, 2006) from 2006 to 2025, with 80% being produced using fossil fuels: oil, gas, and coal, which emit  $\text{CO}_2$  when combusted. Over the last one hundred years, the atmospheric  $\text{CO}_2$  level has risen from 280 to 370 ppm, contributing greatly to the increase in global temperature. One option for mitigating the amount of anthropogenic  $\text{CO}_2$  emitted into the atmosphere is capture and sequestration. Conventional sequestration options for  $\text{CO}_2$  include deep saline formations, depleted or partially depleted oil and gas reservoirs, and coal beds. An additional geologic sequestration option is gas hydrates, where  $\text{CO}_2$  is exchanged with the clathrated (caged in water molecules)  $\text{CH}_4$  in natural gas hydrate accumulations. This hydrate production technology offers two benefits: 1) reducing  $\text{CO}_2$  emissions through sequestration as hydrates, and 2) maintaining the mechanical stability of the reservoir with the production of gas hydrates. Ohgaki et al. (1996) first advanced the concept of exchanging  $\text{CO}_2$  with  $\text{CH}_4$ , through experiments that showed  $\text{CO}_2$  to be preferentially clathrated over  $\text{CH}_4$  in the hydrate phase and dem-

onstrated the possibility of producing CH<sub>4</sub> gas from hydrate by injecting CO<sub>2</sub> gas. During the exchange process, Ohgaki et al. (1996) observed that the mole fraction of CO<sub>2</sub> in the hydrate phase was greater than that in the gas phase. Seo et al. (2001) quantified this effect by noting that gas phase mole fractions of the hydrate formers (i.e., CH<sub>4</sub> and CO<sub>2</sub>) above 40% CO<sub>2</sub> yielded hydrate phase mole fractions of CO<sub>2</sub> in the hydrate phase greater than 90%. In addition to equilibrium considerations, the heat of CO<sub>2</sub> hydrate formation (-57.98 kJ/mol) is greater than the heat of dissociation of CH<sub>4</sub> hydrate (54.49 kJ/mol), which is favorable for the natural exchange of CO<sub>2</sub> with CH<sub>4</sub> hydrate, because the exchange process is exothermic (Goel, 2006).

Pure CH<sub>4</sub> and CO<sub>2</sub> form structure I (sI) type hydrates (Sloan, 1997) and their mixtures also form sI type hydrates (Lee et al., 2003). In forming mixed CH<sub>4</sub> and CO<sub>2</sub> hydrates, the CH<sub>4</sub> molecules occupy both the large and small cages of type sI hydrates, whereas the CO<sub>2</sub> molecules only occupy the large cages. Without hydrate dissociation there is an upper limit to the substitution of CO<sub>2</sub> for CH<sub>4</sub> in hydrates. Lee et al. (2003) estimated that approximately 64% of the CH<sub>4</sub> could be released via exchange with CO<sub>2</sub>. The process of CO<sub>2</sub> exchange with CH<sub>4</sub> in hydrates is complex and to be better understood will require fundamental knowledge about mixed CH<sub>4</sub> and CO<sub>2</sub> hydrates. When gaseous CO<sub>2</sub> is injected into a CH<sub>4</sub> hydrate-bearing formation, the thermodynamic conditions favor CO<sub>2</sub> cage occupancy in the hydrate over CH<sub>4</sub>. For liquid CO<sub>2</sub> injection, thermodynamic conditions can either favor CO<sub>2</sub> or CH<sub>4</sub> cage occupancy. This transition occurs where the pure CO<sub>2</sub> and CH<sub>4</sub> temperature-versus-pressure equilibrium functions cross with increasing pressure above the gas-liquid CO<sub>2</sub> phase boundary. Hydrate equilibrium conditions for liquid CO<sub>2</sub> generally are not well understood (Wilder et al., 2002). Therefore, quantification of the CO<sub>2</sub> exchange process for liquid CO<sub>2</sub> at high pressures is difficult.

Natural deposits of gas hydrates occur in porous media. Equilibrium conditions for hydrates differ between bulk conditions (ex-situ) and in porous media (in-situ). In-situ equilibrium pressures at a given temperature are greater and equilibrium temperatures at a given pressure are lower compared with ex-situ values. Differences between in-situ and ex-situ conditions increase with decreasing pore radius. Hydrate formation in geologic media that have a distribution of pore sizes will begin in the largest pore spaces and then continue into smaller pore spaces until the in-situ equilibrium condition is reached for a particular pore radius (Clennell et al., 1999) and residual salt content in the pore water (McGrail et al., 2007). In addition to the equilibrium condition, porous media may affect other thermodynamic properties of hydrates. For example, in Goel's (2006) review of CH<sub>4</sub> production with CO<sub>2</sub> sequestration, a number of contrasting observations were revealed concerning the in-situ enthalpy of dissociation of CO<sub>2</sub> and CH<sub>4</sub> hydrates. Some research indicated that there was an increase in the heat of dissociation between in-situ and ex-situ conditions; whereas, other research indicated the opposite. Another example is the value of the lower quadruple point (ice-water-hydrate-gas) temperature and pressure for CH<sub>4</sub> and CO<sub>2</sub>, and the upper quadruple point (water-hydrate-gas-liquid CO<sub>2</sub>) for CO<sub>2</sub> hydrate between in-situ and ex-situ conditions; where, the in-situ conditions were determined for a porous media of limited pore-size distribution. In geologic media that have a distribution of pore sizes, hydrates would form and dissociate over a range of temperatures and pressures according to the distribution of pore radii. The critical conclusion from Goel's (2006) review with respect to hydrates in porous media, is that to understand the gas exchange technology there is a need for quantitative estimates of formation and dissociation processes in geologic media core samples.

### 1.1.5 Classification of Gas Hydrate Deposits

Moridis and Collett (2003) developed a convenient classification system for geologic deposits of gas hydrates with respect to their production strategy and behavior, involving four main classes. Class 1 hydrate deposits have a permeable hydrate interval overlying a hydrate-free unsaturated interval with mobile aqueous and gas phases. Class 2 hydrate deposits have a permeable hydrate interval overlying a hydrate-free saturated interval with a mobile aqueous phase, but no mobile gas phase. Class 3 hydrate deposits are characterized by the lack of a hydrate-free zone beneath the permeable hydrate interval. Class 4 hydrate deposits are dispersed, low-saturation accumulations in marine geologic media.

## 1.2 Hydrate Guest Molecule Exchange

The conventional concept behind producing natural gas from geologic accumulations of gas hydrates is to somehow alter the reservoir environment from being thermodynamically stable to unstable for methane hydrates. Thermodynamic stability of gas hydrates depends on temperature, pressure of guest molecules, and aqueous solute concentrations. Approaches for producing gas hydrates have focused on elevating the reservoir environment temperature (thermal stimulation), lowering the system pressure (depressurization), or raising the aqueous solute concentration (inhibitor injection). These more conventional approaches shift the environment to one that is thermodynamically unstable for methane hydrates, resulting in dissociation of the gas hydrate and liberation of natural gas. An alternative approach is to lower the partial pressure of the guest molecule by introducing a substitute guest molecule. Methane ( $\text{CH}_4$ ) and carbon dioxide ( $\text{CO}_2$ ) both form structure I hydrates (Sloan and Koh, 2007). Introducing carbon dioxide into geologic media filled with methane hydrate results in the displacement of methane with carbon dioxide as the guest molecule, without the dissociation of the gas hydrate (Graue et al., 2006; Stevens et al., 2008).

The concept of exchanging carbon dioxide with methane in geologic accumulations of natural gas hydrates as a production technology was first advanced by Ohgaki et al. (1996). This concept was then extended to ethane hydrates by Nakano et al. (1998). The original concept proposed by Ohgaki et al. (1996) involved injecting carbon dioxide gas into an aqueous-gas-hydrate system and allowing the carbon dioxide and methane to equilibrate. The greater chemical affinity for carbon dioxide over methane in the hydrate structure, as evidenced by the higher heat of formation and equilibrium temperature, yields a mixed carbon dioxide-methane hydrate. Resulting equilibrium concentrations of carbon dioxide are greater than methane in the hydrate phase and less than methane in the gas phase. Since the original studies by Ohgaki et al. (1996), Hirohama et al. (1996), and Komai et al. (1997), the carbon dioxide-methane exchange technology has been investigated by others. Smith et al. (2001) assessed the feasibility of exchanging carbon dioxide with methane in geologic accumulations of gas hydrate by examining the thermodynamic potential for the exchange as a function of pore sizes. This study concluded that the replacement of methane by carbon dioxide in geologic accumulations of gas hydrate is less thermodynamically favored as pore size decreases.

Following these laboratory investigations of guest-molecule exchange for gas hydrates in geologic media, several researchers explored concepts for developing field production technologies. Rice (2003, 2006) proposed a methane hydrate production scheme for sub-oceanic deposits that yields hydrogen and carbon dioxide. In this scheme, methane hydrate is produced using the more conven-

tional technologies (e.g., thermal stimulation, depressurization) and the captured carbon dioxide is sequestered on the ocean floor or in the sub-oceanic sediments in hydrate form. Whereas Rice's scheme involves carbon dioxide sequestration in hydrate form, the carbon dioxide-methane molecular exchange is indirect, requiring hydrate dissociation and subsequent reformation. McGrail et al. (2004) proposed a concept for exchanging carbon dioxide with methane in geologic deposits of gas hydrate by injecting a micro-emulsion of liquid carbon dioxide and water. The micro-emulsion is designed to provide sensible heat to dissociate the methane hydrate, taking advantage of the higher heat of formation for the carbon dioxide hydrate versus the methane hydrate. This technology was demonstrated in laboratory columns and numerically simulated (White and McGrail, 2006). Castaldi et al. (2007) investigated the technical feasibility of a down-hole combustion method for producing natural gas hydrate and sequestering carbon dioxide. The details of replacing carbon dioxide with methane in the hydrate structure were left unspecified, other than to require a balance in the rates of methane hydrate dissociation and carbon dioxide hydrate formation.

The Korean Institute of Geosciences and Mineral Resources (KIGAM) has conducted a series of experimental studies (KIGAM, 2006): 1) transport properties of hydrate-bearing sediments with various grain-size distributions and gas hydrate contents; and 2) core-scale analysis of production techniques, using conventional and methane replacement approaches. The methane-replacement experiments involved the injection of gaseous mixtures of  $\text{CO}_2\text{-N}_2$  into  $\text{CH}_4$  hydrate bearing soil columns that were generated from drained water columns, yielding a mobile gas phase in the column. The experimental results show nearly immediate breakthrough of  $\text{CO}_2$  in the effluent stream when the  $\text{CO}_2\text{-N}_2$  gases were injected at high pressures and high flow rates. At lower pressures  $\text{CO}_2$  breakthrough was more gradual, regardless of the flow rate. These results indicate that exchange of hydrate guest molecules is a kinetic process and that the time scales for the exchange process needs to be considered against the transport time scales before attempting to reproduce the experimental results using numerical simulation. These experiments represent a numerical simulation challenge, in that it requires capabilities for a ternary hydrate mixture and kinetic exchange of guest molecules. Currently, we are not aware of a numerical simulator with these capabilities. A numerical solution scheme for simulating binary hydrate mixtures with kinetic exchange of hydrate guest molecules has been demonstrated, as described below for the STOMP-HYD simulator, but this scheme has not been extended to ternary hydrate systems.

### 1.3 Report Organization

This report documents the work performed by Battelle Pacific Northwest Division under the Comparative Assessment of Advanced Gas Hydrate Production Methods project, funded by the U.S. Department of Energy, National Energy Technology Laboratory. Numerical simulations conducted for these studies were executed with the STOMP-HYD simulator. The application and development of STOMP-HYD has been an iterative process, where simulation results have guided new developments, which are then applied to new evaluations. This project has been ongoing for approximately three years, which has provided time for the iterative development and application of the simulator, and maturation in understanding the hydrate guest molecule exchange production technology. Four publications resulted from this work (White and McGrail, 2006; White and McGrail, 2008a, b; White et al., 2009). This report includes results from the later two publications on Class 1 and 2 gas hydrate accumulations, plus previously unreported simulation results for Class 3 gas hydrate accumulations. This report first describes the STOMP-HYD simulator, beginning with descriptions of the governing and constitutive equations and numerical solution schemes. Also included in the simulator section are guides on input and output specifications that are unique to the STOMP-HYD operational mode of the STOMP suite of simulators. The simulator section concludes with an over-

view of the numerical solution scheme developed to model the kinetic exchange of hydrate guest molecules for the CH<sub>4</sub>-CO<sub>2</sub> binary hydrate system. Following the simulator section are two sections that report the assessment of using CO<sub>2</sub> injection to produce Class 1 and 2 gas hydrate accumulations (i.e., those with mobile fluid layers beneath the hydrate zone) and Class 3 gas hydrate accumulations (i.e., those with the hydrate layer bound between two impermeable layers). The report then concludes with an overall assessment of producing Class 1, 2, and 3 gas hydrate accumulations using CO<sub>2</sub> injection and comments on alternative hydrate guest molecule exchange approaches that may have merit.

## 2.0 STOMP-HYD

Numerical simulations executed for this report were conducted with the STOMP-HYD simulator (White and McGrail, 2008a, b). STOMP-HYD solves conservation equations for water mass, methane mass, carbon-dioxide mass, water-soluble inhibitor (salts or alcohols) mass, and thermal energy. The conservation equations for carbon dioxide and inhibitor mass are optional. The simulator considers mass and energy transport over three mobile phases (i.e., aqueous, gas, and liquid carbon dioxide) and four immobile phases (i.e., hydrate, ice, precipitated salt, and geologic media). Hydrate properties, including cage occupancies and equilibrium conditions, are functions of the guest molecule concentrations (i.e., methane and carbon dioxide). Hydrate dissociation/formation are assumed to be equilibrium processes, as is the exchange mechanism for gas hydrate guest molecules. The STOMP-HYD simulator solves the governing conservation equations using integral volume differencing on structured orthogonal grids for spatial discretization and a fully implicit formulation for temporal discretization. Nonlinearities in the discretized governing equations are resolved using Newton-Raphson iteration with continuous property updating. Phase transitions (i.e., appearances and disappearances) are handled using a primary variable switching scheme.

### 2.1 Conservation Equations

Expressed in integral form, the mass conservation equations solved by STOMP-HYD equate the rate of change of mass within a volume with the net flux of mass into the volume over the volume surface plus the rate of mass generation within the volume, see Mathematical Symbols and Nomenclature:

$$\frac{d}{dt} \int_V \sum_{\gamma=l,n,g,h,i,p} (\phi \omega_\gamma^i \rho_\gamma s_\gamma) dV = \int_{\Gamma} \sum_{\gamma=l,n,g} \omega_\gamma^i \rho_\gamma \mathbf{V}_\gamma \cdot \mathbf{n} d\Gamma + \int_{\Gamma} \sum_{\gamma=l,n,g} \mathbf{J}_\gamma^i \cdot \mathbf{n} d\Gamma + \int_V m^i dV \quad (2.1)$$

The volumetric flux of a mobile phase is computed according to Darcy's law:

$$\mathbf{V}_\gamma = -\frac{k_{r\gamma} \mathbf{k}}{\mu_\gamma} (\nabla P_\gamma + \rho_\gamma g \mathbf{z}) \quad (2.2)$$

The diffusive/dispersive component mass fluxes through the mobile phases are computed from gradients in molar concentration:

$$\mathbf{J}_\gamma^i = -\phi \rho_\gamma s_\gamma \frac{M^i}{M_\gamma} (\tau_\gamma D_\gamma^i + \mathbf{D}_{h\gamma}) \nabla \chi_\gamma^i \quad (2.3)$$

As with the mass conservation equations, the conservation of energy equation solved by STOMP-HYD equates the rate of change of energy within a volume with the net flux of heat into the volume over the volume surface, plus the rate of heat generated within the volume:

$$\begin{aligned} \frac{d}{dt} \int_V \left\{ \sum_{\gamma=l,n,g,h,i,p} (\phi u_\gamma \rho_\gamma s_\gamma) + (1-\phi) u_s \rho_s \right\} dV &= \int_\Gamma \sum_{\gamma=l,n,g} h_\gamma \rho_\gamma \mathbf{V}_\gamma \cdot \mathbf{n} d\Gamma \\ + \int_\Gamma \sum_{i=w,a,o} h_g^i \mathbf{J}_g^i \cdot \mathbf{n} d\Gamma &+ \int_\Gamma \mathbf{F} \cdot \mathbf{n} d\Gamma + \int_V q dV \end{aligned} \quad (2.4)$$

The diffusive heat flux is computed from a linear combination of phase conductivity and gradients in temperature:

$$\mathbf{F} = - \left\{ \sum_{\gamma=l,n,g,h,i,p} (\phi k_\gamma s_\gamma) + (1-\phi) k_s \right\} \nabla T \quad (2.5)$$

Although salinity could play an important role in inhibiting secondary hydrate formation with the injection of carbon dioxide, the gas hydrate reservoir was assumed to be salt free. Without the salt component, there were four coupled conservation equations solved at each grid cell (i.e., water mass, carbon dioxide mass, methane mass, and energy). Primary unknowns for the conservation equations must be chosen to be independent and able to define the system state (i.e., compute the suite of secondary variables). Phase transitions, including phase appearances and disappearances, preclude the use of a single set of primary variables throughout the simulation. To overcome this numerical difficulty, a primary variable switching scheme was implemented that switches primary variable sets with phase transitions. Phase transitions and primary variable switching occurs between Newton-Raphson iterations within a single time step, which often leads to slow convergence rates. Without the liquid-CO<sub>2</sub> phase there are 15 phase combinations for the 4 possible phases (i.e., aqueous, gas, hydrate, and ice) in the geologic gas-hydrate system. When the liquid-CO<sub>2</sub> phase is added as a potential phase there are 31 phase combinations in the geologic gas-hydrate system. If the assumption is made that the aqueous phase never completely disappears, the number of phase combinations is reduced to 14 for the geologic gas-hydrate system with liquid-CO<sub>2</sub> phase. By assuming equilibrium conditions between the hydrate and the vapor partial pressure of the guest molecules and equilibrium conditions between liquid-CO<sub>2</sub> and the vapor partial pressure of carbon dioxide, the number of sets of primary variables needed for the 14 phase conditions is 4; where the phase conditions are distinguished by the absence or presence of hydrate and liquid-CO<sub>2</sub> phases. Primary variable sets and ancillary equations are shown in Table 2.1 versus the phase condition sets.

**Table 2.1** Primary variable sets and ancillary equations.

<b>Phase Condition #1 ( No Hydrate, No Liquid-CO<sub>2</sub> )</b>		
Energy - $T$		
H <sub>2</sub> O Mass - $P_l$	$P_g = \max \left[ \left( P_l + \frac{\beta_{gl}}{\psi} \right), \left( P_g^{CO_2} + P_g^{CH_4} + P_g^{H_2O} \right) \right]$	$P_h^{eq} = P_g^{CO_2} + P_g^{CH_4}$
CH <sub>4</sub> Mass - $P_g^{CH_4}$		
CO <sub>2</sub> Mass - $P_g^{CO_2}$	$P_n = P_n^c$	
<b>Phase Condition #2 ( Hydrate, No Liquid-CO<sub>2</sub> )</b>		
Energy - $T$		
H <sub>2</sub> O Mass - $P_l$	$P_g = \max \left[ \left( P_l + \frac{\beta_{gl}}{\psi} \right), \left( P_g^{CO_2} + P_g^{CH_4} + P_g^{H_2O} \right) \right]$	$P_h^{eq} = \text{func} \left[ T_h^{eq}, \varphi_g^{CH_4} \right]$
CH <sub>4</sub> Mass - $s_h$		
CO <sub>2</sub> Mass - $\psi_g^{CH_4}$	$P_n = P_n^c$	
<b>Phase Condition #3 ( No Hydrate, Liquid CO<sub>2</sub> )</b>		
Energy - $T$		
H <sub>2</sub> O Mass - $P_l$	$P_g = \max \left[ \left( P_l + \frac{\beta_{gl}}{\psi} \right), \left( P_g^{CO_2} + P_g^{CH_4} + P_g^{H_2O} \right) \right]$	$P_g^{CO_2} = P_{sat}^{CO_2}$
CH <sub>4</sub> Mass - $P_g^{CH_4}$		
CO <sub>2</sub> Mass - $P_n$	$P_h^{eq} = P_g^{CO_2} + P_g^{CH_4}$	
<b>Phase Condition #4 ( Hydrate, Liquid CO<sub>2</sub> )</b>		
Energy - $T$		
H <sub>2</sub> O Mass - $P_l$	$P_g = \max \left[ \left( P_l + \frac{\beta_{gl}}{\psi} \right), \left( P_g^{CO_2} + P_g^{CH_4} + P_g^{H_2O} \right) \right]$	$P_g^{CO_2} = P_{sat}^{CO_2}$
CH <sub>4</sub> Mass - $s_h$		
CO <sub>2</sub> Mass - $P_n$	$P_h^{eq} = \text{func} \left[ T_h^{eq}, \varphi_g^{CH_4} \right]; P_g^{CH_4} = P_h^{eq} \varphi_g^{CH_4}$	

## 2.2 Constitutive Equations

Constitutive equations relate primary variables to secondary variables. Typically these equations are nonlinear, requiring an iterative solution scheme for the primary variables. Most of the constitutive equations in STOMP-HYD are described in detail in the STOMP Theory Guide (White and Oostrom, 2000). Those constitutive equations unique to STOMP-HYD will be described here. The properties of carbon dioxide (e.g., density, viscosity, internal energy, enthalpy, thermal conductivity) are computed using tabulated data generated from the Span and Wagner (1996) formulations. The properties of methane (e.g., density, viscosity, internal energy, enthalpy, thermal conductivity) are computed using tabulated data generated from the Setzmann and Wagner (1991) formulations. The hydrate properties (e.g., density, enthalpy, cage occupancies) for mixed hydrates are computed from the formulations of Sloan and Koh (2007). Changes to the equilibrium pressure and temperature relationships with respect to inhibitor concentrations are computed using tabular data and formulations published by Herriot-Watt Institute of Petroleum Engineering (Ostergaard et al., 2005).

Relationships between phase pressures and phase saturations, and phase saturations and phase relative permeabilities, are additionally required to compute the transport properties of the system. In the subject version of the simulator, hydrate saturation is assumed to be independent of pore radii and capillary pressure. In previous versions of the simulator (White and McGrail, 2006) hydrate was assumed to be totally occluded by the aqueous phase and the hydrate saturation was computed as a function of the pore-size distribution and the difference between the temperature and bulk equilibrium temperature for the hydrate. The dependence of hydrate equilibrium conditions on pore-size has been ignored. For no-liquid-CO<sub>2</sub> conditions the aqueous saturation is a function of the capillary pressure between the gas and aqueous phases and the hydrate and ice saturations:

$$s_l = \frac{\left[ \frac{s_l}{(1 - s_h - s_i)} \right]^{-s_{lr}}}{(1 - s_{lr})} = \text{func} \left[ \beta_{gl} (P_g - P_l) \right]; \text{ where } \beta_{gl} = \frac{\sigma_{ref}}{\sigma_{gl}} \quad (2.6)$$

This approach assumes that the form of the moisture retention characteristic curve is maintained as the immobile hydrate and ice phases fill the pore space. Moreover, for no-liquid-CO<sub>2</sub> conditions, the liquid-CO<sub>2</sub> pressure is set to the critical phase pressure:

$$P_n = \frac{\beta_{nl} P_l + \beta_{ng} P_g}{\beta_{nl} + \beta_{ng}}; \text{ where } \beta_{nl} = \frac{\sigma_{ref}}{\sigma_{nl}} \text{ and } \beta_{ng} = \frac{\sigma_{ref}}{\sigma_{ng}} \quad (2.7)$$

For liquid-CO<sub>2</sub> conditions the aqueous saturation is a function of the capillary pressure between the liquid-CO<sub>2</sub> and the aqueous pressure:

$$s_l = \frac{\left[ \frac{s_l}{(1-s_h-s_i)} \right]^{-s_{lr}}}{(1-s_{lr})} = \text{func} \left[ \beta_{nl} (P_n - P_l) \right] \quad (2.8)$$

The liquid-CO<sub>2</sub> saturation is computed indirectly from the total-liquid (i.e., aqueous + liquid CO<sub>2</sub>) saturations; where the total-liquid saturation is a function of the capillary pressure between the gas and liquid-CO<sub>2</sub> phases:

$$s_n = s_t - s_l; \text{ where } s_t = \frac{\left[ \frac{s_t}{(1-s_h-s_i)} \right]^{-s_{lr}}}{(1-s_{lr})} = \text{func} \left[ \beta_{gn} (P_g - P_n) \right] \quad (2.9)$$

Permeabilities are required for the three mobile phases (i.e., gas, liquid-CO<sub>2</sub>, and aqueous). Phase permeabilities are computed as the product of the intrinsic permeability and the phase relative permeability. There are two conventional approaches to addressing the impact of the immobile phases (i.e., hydrate and ice) on the phase permeabilities: 1) variable intrinsic permeability, and 2) constant intrinsic permeability. In the variable intrinsic permeability approach, the immobile phases are considered to alter the intrinsic permeability of the geologic media via the Kozeny-Carman equation (McCabe et al., 2005) or alternative function. The phase relative permeability is then computed as a function of the effective phase saturations. In the constant intrinsic permeability approach, the intrinsic permeability is considered to be a constant, and the phase relative permeabilities are computed using effective phase saturations defined from the actual saturations. In the constant intrinsic permeability approach, the effect of the immobile phases is incorporated indirectly through the use of the actual phase saturations. The constant intrinsic permeability approach was applied for the simulations documented in this report.

A critical component of the STOMP-HYD simulator is the representation of hydrate equilibrium as a function of the concentrations of hydrate formers. Both CH<sub>4</sub> and CO<sub>2</sub> form sl hydrates and their mixtures also form sl hydrates. The hydrate equilibrium functions are implemented in STOMP-HYD through tabular data. To reduce the computational effort for interpolating these tabular data, STOMP-HYD uses two equilibrium data sets: 1) pressure as a function of temperature and hydrate former composition and 2) temperature as a function of pressure and hydrate former composition. In the earlier versions of STOMP-HYD, these tabular data were provided from the fugacity-based model of Klauda and Sandler (2003), which was shown to be an improvement over the classical van der Waals and Platteeuw (vdWP) model. For single guest hydrates, the Klauda and Sandler (2003) model had an improved percent absolute average deviation (%AAD) for all the equilibrium data of 5.7% compared with 15.1% for the vdWP model. Anderson et al (2005) have developed a cell potential (CellPot) method to the solution of the vdWP model, improving the %AAD for both single and multiple guest hydrate thermodynamic equilibria. Using this model, Anderson generated both temperature and pressure gas hydrate equilibrium data sets for the binary CH<sub>4</sub>-CO<sub>2</sub> system. A comparison of experimental equilibrium data, Klauda and Sandler equilibrium data, and Anderson equilibrium data are shown for CH<sub>4</sub> hydrate in Figure 2.1, and for CO<sub>2</sub> hydrate in Figure 2.2. Also shown

on Figure 2.2 are the hydrate number (number of water molecules per guest molecule) model predictions for the pure CO<sub>2</sub> hydrate. Recently, Anderson has been using molecular-dynamics modeling to determine the lattice expansion or contraction that occurs with changes in temperature or guest molecule composition and to determine the impact of mixed hydrate lattice strain on the large and small cage occupancies of mixed CO<sub>2</sub>-CH<sub>4</sub> hydrates. Equilibrium data for mixed CO<sub>2</sub>-CH<sub>4</sub> hydrate from Anderson's model applied in STOMP-HYD are shown in Figure 2.3.

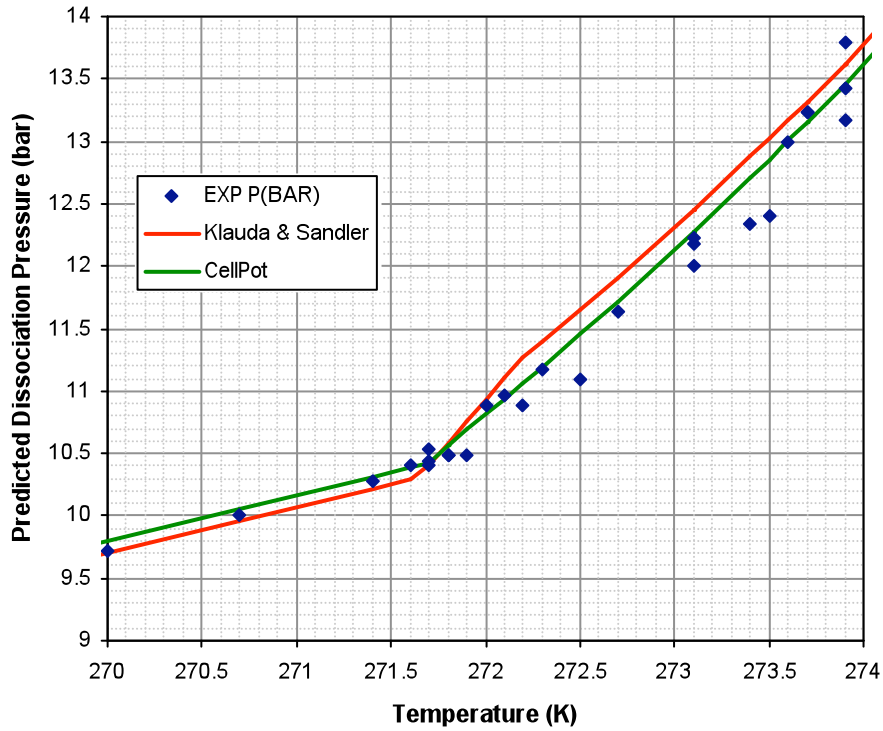


**Figure 2.1.** CH<sub>4</sub> Hydrate Equilibrium Data Comparisons

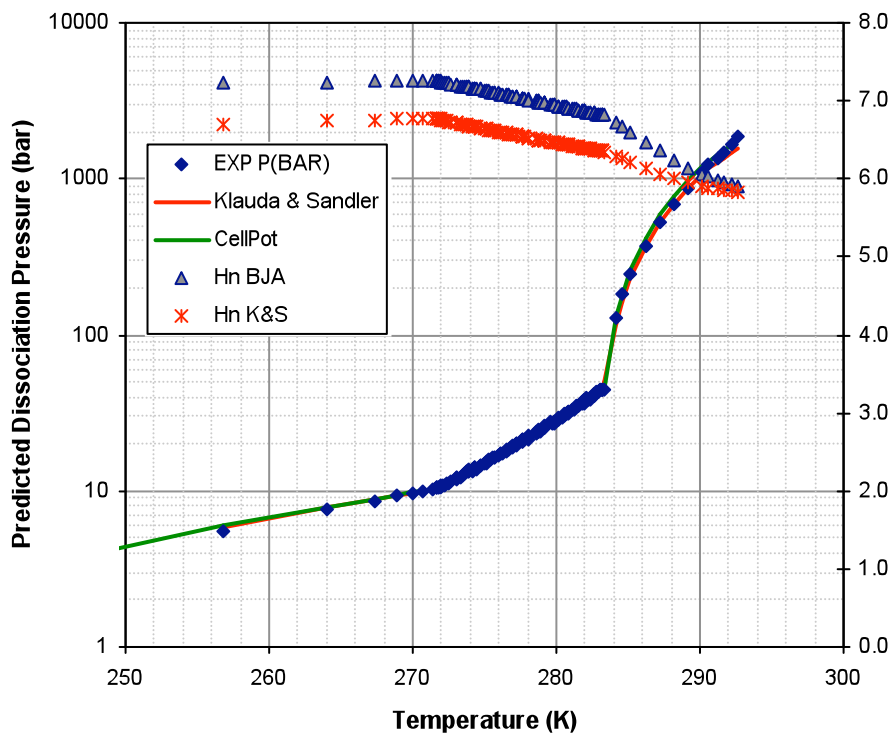


Figure 2.2. CO<sub>2</sub> Hydrate Equilibrium Data and Hydrate Number Comparisons

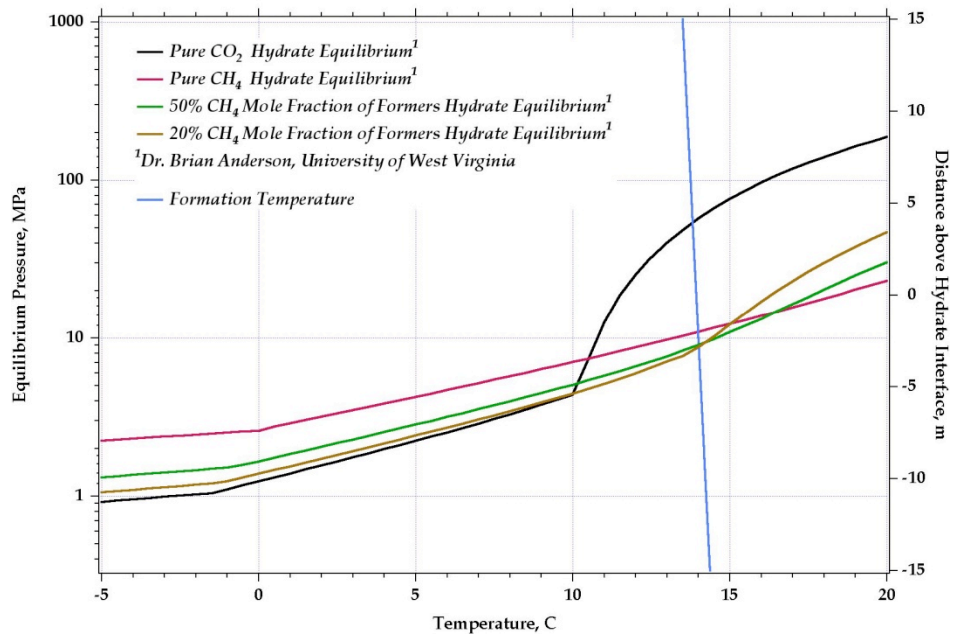


Figure 2.3. Mixed CO<sub>2</sub>-CH<sub>4</sub> Hydrate Equilibrium Data

## 2.3 Specifications

A fundamental assumption incorporated into STOMP-HYD is thermodynamic equilibrium between phases. Gibb's phase rule states the number of degrees of freedom is equal to the number of components minus the number of phases in thermodynamic equilibrium plus two:

$$F = C - P + 2 \quad (2.10)$$

A porous media, however, has  $P$  distinct phase pressures, compared with a single pressure in a nonporous media, resulting in  $(P - 1)$  additional variables (Bear and Nitao, 1995):

$$F = C + 1 \quad (2.11)$$

This results in the phase rule for porous media being independent of the number of phases. Ignoring inhibitors, STOMP-HYD considers three components (i.e., H<sub>2</sub>O, CH<sub>4</sub>, and CO<sub>2</sub>), which implies four independent variables must be specified to define the system state. Ignoring salt inhibitors, STOMP-HYD considers three mobile phases (i.e., aqueous, gas, and liquid CO<sub>2</sub>) and two immobile phases (i.e., hydrate and ice). When the liquid CO<sub>2</sub> phase is present CO<sub>2</sub> vapor pressure and aqueous CO<sub>2</sub> concentrations are fixed by equilibrium expressions. When the hydrate phase is present the vapor pressures of hydrate formers (i.e., CH<sub>4</sub> and CO<sub>2</sub>) and aqueous concentrations of the hydrate formers are fixed by the hydrate phase mole fractions and equilibrium expressions. The aqueous phase is assumed to always be present, which means the water vapor pressure is fixed by equilibrium expressions. The porous-media phase rule and equilibrium expressions impose restrictions on specifying initial and boundary conditions for STOMP-HYD. To resolve the number of primary variable options for specifying initial and boundary conditions, flash calculation subroutines are used to convert user initial condition and boundary condition specifications into the standard primary variable set for the specified phase condition.

### 2.3.1 Initial Conditions

For initial conditions, STOMP-HYD permits the user to specify values for the variables shown below:

Aqueous Pressure	Gas Pressure
Liquid-CO <sub>2</sub> Pressure	Temperature
Hydrate Saturation	Hydrate CO <sub>2</sub> Mass Fraction of Formers
Hydrate CO <sub>2</sub> Mole Fraction of Formers	Gas CO <sub>2</sub> Mass Fraction of Formers
Gas CO <sub>2</sub> Mole Fraction of Formers	Aqueous CO <sub>2</sub> Relative Saturation
Aqueous CO <sub>2</sub> Mass Fraction	Aqueous CO <sub>2</sub> Concentration
Hydrate CH <sub>4</sub> Mass Fraction of Formers	Hydrate CH <sub>4</sub> Mole Fraction of Formers
Gas CH <sub>4</sub> Mass Fraction of Formers	Gas CH <sub>4</sub> Mole Fraction of Formers
Aqueous CH <sub>4</sub> Relative Saturation	Aqueous CH <sub>4</sub> Mass Fraction
Aqueous CH <sub>4</sub> Concentration	Aqueous Salt Relative Saturation
Aqueous Salt Mass Fraction	Aqueous Salt Concentration

This approach provides the user with considerable flexibility in setting initial conditions, but it also requires that the user not over or under specify the system. Over specification implies that more independent variables are set in a grid cell than needed to fix the system state and under specification implies that not enough independent variables are set in a grid cell to fix the system state. Initial condition specifications are converted to phase conditions and primary variables through three subroutines in STOMP-HYD: 1) RDIC (read initial condition card), 2) CHK (check initial conditions), and 3) FLH (initial conditions flash calculations). The RDIC subroutine reads in user specifications from the input file with the Initial Conditions Card. This subroutine is only responsible for reading initial condition values without any consideration of the system state. The CHK subroutine checks that the initial condition values are within set limits, determines the phase condition for each grid cell, checks that the system state is not over- or under- specified and calls the appropriate flash calculation subroutine. FLH routines are a series of flash-calculation subroutines that convert the specified initial condition inputs into the set of four primary variables for a particular phase condition (i.e., No Hydrate-No Liquid CO<sub>2</sub>, No Hydrate-Liquid CO<sub>2</sub>, Hydrate-No Liquid CO<sub>2</sub>, or Hydrate-Liquid CO<sub>2</sub>), according to Table 2.1. The FLH subroutines solve for the primary variables either directly or indirectly through numerical iteration and are mathematically based on the assumption of thermodynamic equilibrium between phases. One example of an initial condition specification conflict is the specification of hydrate saturation, gas pressure, and hydrate CO<sub>2</sub> or CH<sub>4</sub> fraction of formers. The gas pressure of the system is defined by the sum of the water vapor partial pressure, CO<sub>2</sub> partial pressure, and CH<sub>4</sub> partial pressure. Under all phase conditions the water vapor pressure is determined from the temperature and gas-aqueous capillary pressure. Under hydrate phase conditions, the partial pressure of CO<sub>2</sub> and CH<sub>4</sub> is defined by the temperature and gas mass fraction of formers, which is determined indirectly from the hydrate mass fraction of formers, making specification of the gas pressure redundant.

### 2.3.2 Boundary Conditions

Boundary conditions in STOMP-HYD are specified independently for thermal energy, aqueous phase, gas phase, liquid-CO<sub>2</sub> phase and salt (inhibitor). This approach provides the user with flexibility to specify boundary conditions that are in thermodynamic equilibrium or not. Because of this flexibility there are no checks on boundary condition specifications, which places more onus on the user for developing equilibrium conditions across the boundary phases. All boundary conditions in STOMP-HYD can be constant or time varying. Thermal energy boundary conditions are one of three types: 1) Dirichlet, 2) Neumann, or 3) Advective. The Dirichlet boundary condition is a specified temperature on the boundary surface. A special version of the Dirichlet boundary is the initial condition option, which imposes the initial temperature of the adjacent grid cell to the boundary surface. The Neumann boundary condition is a specified heat flux across the boundary surface. A special version of the Neumann boundary condition is the zero flux or adiabatic boundary. The Advective boundary condition is a modified Dirichlet boundary condition where the temperature is specified on the boundary surface, but heat is only allowed to flow across the surface by advective transport in the mobile phases (i.e., aqueous, gas, liquid CO<sub>2</sub>).

Boundary conditions for the mobile phases generally are the same as those for thermal boundaries (i.e., Dirichlet, Neumann, and Advective), but with different variables and special versions. The Dirichlet boundary condition is a specified phase pressure (i.e., aqueous, gas, liquid CO<sub>2</sub>). The initial-condition special version of the Dirichlet boundary condition imposes the initial phase pressure at the grid-cell centroid plus any gravitational changes between the grid-cell and boundary-surface centroids to the boundary surface. The hydraulic-gradient special version of the Dirichlet boundary condition uses a specified phase pressure at the lowest indexed boundary surface centroid, and

then computes the phase pressure across the boundary surfaces, accounting for gravitational changes between the boundary-surface centroids. The Neumann boundary condition is a specified phase flux (i.e., phase volume/time/boundary surface area =  $\text{m}^3/\text{s m}^2$ ). For both the Dirichlet and Neumann boundaries, phase components (i.e., water,  $\text{CH}_4$ ,  $\text{CO}_2$ ) can diffuse and advect across the boundary surface. The Advective boundary condition is a modified Dirichlet boundary condition, where the phase pressure is specified on the boundary surface, but phase components are only allowed to flow across the surface by advective transport. In addition to the phase pressure or surface flux, the aqueous-phase boundaries require the specification of the dissolved  $\text{CO}_2$  and  $\text{CH}_4$  concentrations as relative saturations; where, a relative saturation of 1.0 implies the aqueous phase is saturated with the component under the phase pressure and temperature conditions. The gas-phase boundaries additionally require the specification of the  $\text{CO}_2$  gas mass fraction and water-vapor relative humidity. The  $\text{CH}_4$  gas mass fraction is computed from the gas pressure and the  $\text{CO}_2$  and water-vapor partial pressures. The liquid- $\text{CO}_2$  phase boundary condition requires no additional specifications as the liquid- $\text{CO}_2$  phase is assumed to comprise only  $\text{CO}_2$  (i.e., no dissolved water or  $\text{CH}_4$ ). All boundary conditions require a specification of hydrate saturation on the boundary surface.

Because STOMP-HYD was designed to consider the injection of micro-emulsions of  $\text{CO}_2$ , a special boundary condition specification is available for this application. For this boundary condition, a micro-emulsion volume fraction is specified. A non-zero volume fraction transforms the aqueous phase boundary into a micro-emulsion boundary, where the state of the  $\text{CO}_2$  (i.e., subcritical gas, subcritical liquid, or supercritical gas) is determined by the aqueous pressure and temperature conditions on the boundary. This boundary condition specifies the mass flux ( $\text{kg}/\text{s m}^2$ ) at which  $\text{CO}_2$  crosses the boundary surface, but the concept of migration within the geologic media in the form of a micro-emulsion is dropped. Once the  $\text{CO}_2$  enters the geologic media, it is assumed to be in thermodynamic equilibrium with all of the  $\text{CO}_2$  within the grid cell and flows across internal grid surfaces as a component in the aqueous, gas, or liquid- $\text{CO}_2$  phases. Whereas the micro-emulsion boundary condition can be applied in conjunction with independent gas and liquid- $\text{CO}_2$  boundary conditions and it can be applied to an outflow aqueous surface, its application is generally restricted to inflowing aqueous boundary conditions with zero flux gas and liquid- $\text{CO}_2$  boundary conditions. Finally, STOMP-HYD (nor any other reservoir simulator) has capability to analyze stability of a micro-emulsion undergoing high shear rate transport as the two-phase fluid migrates in the porous medium.

### 2.3.3 Output

Output specification for STOMP-HYD follows the general protocol for the STOMP suite of simulators. Field variables can be output at selected grid cells at specified time step intervals (e.g., every time step, every five time steps) or for all grid cells at specified times (e.g., 1 day, 0.5 years, 40 weeks). Additionally, surfaces can be defined and fluxes across those surfaces can be output as rates and integrals at every time step. To track the exchange of  $\text{CO}_2$  and  $\text{CH}_4$  differential integrated mass outputs were created that track the difference in integrated mass from the initial time for total  $\text{CO}_2$  and hydrate mass (e.g., differential integrated  $\text{H}_2\text{O}$  hydrate mass, differential integrated total  $\text{CO}_2$  mass). Because these outputs are differential integrals, they preserve small changes in the distributions of integrated mass, and the total quantities can be reconstructed from the integrated masses reported at the initial time step.

## 2.4 Development Chronology

Numerical simulators for multifluid subsurface flow and transport are founded on conservation equations, constitutive equations, and the conceptual models associated with those equation sets. During its development, the STOMP-HYD simulator underwent changes in its conceptual models and numerical solution approaches. This section highlights significant changes that occurred during the development of STOMP-HYD. Prior to developing STOMP-HYD, scoping simulations for the Enhanced Gas Hydrate Recovery (EGHR) process were conducted (McGrail et al., 2004) using a modified version of STOMP-CO<sub>2</sub>, a multifluid flow and reactive transport simulator for geologic sequestration of CO<sub>2</sub>. For these studies, an equation of state module was added to STOMP-CO<sub>2</sub> for calculating equilibrium stability, physical, and thermodynamic properties of gas hydrates in the H<sub>2</sub>O-NaCl-CO<sub>2</sub>-CH<sub>4</sub> system. A full kinetic model for gas hydrate formation and decomposition is used to compute mass balance at each grid node. Early results confirm that the injectant plume does not have to cover the entire area of review containing gas hydrate to be dissociated; heat transfer destabilizes more than twice the injected emulsion volume.

### 2.4.1 STOMP-HYD<sub>1</sub>

The first conceptual design for the STOMP-HYD simulator occurred in collaboration with Dr. Zhu and his graduate students at the University of Alaska, Fairbanks. The initial simulator design was founded on a set of conservation equations which have not changed over the course of development: 1) thermal energy, 2) water mass, 3) CH<sub>4</sub> mass, 4) CO<sub>2</sub> mass, and 5) salt or inhibitor mass. Whereas the conservation equations were fixed early in the development process, the numerical solution approach has changed significantly over time. The initial hydrologic conceptual model for this simulator was based on the micro-emulsion being a distinct mobile phase in the geologic media and used four phase conditions: 1) wetting fluid saturated w/o micro-emulsion, 2) wetting fluid saturated w/ micro-emulsion, 3) wetting fluid unsaturated w/o micro-emulsion, and 4) wetting fluid unsaturated w/ micro-emulsion. This phase distribution concept was quickly abandoned for one where the aqueous, liquid-CO<sub>2</sub>, and gas phases migrated in response to pressure gradients and gravitational body forces acting on the individual phases. The concept of micro-emulsion was restricted to defining flows on boundary surfaces. This hydrologic conceptual model formed the basis for the first version of STOMP-HYD (STOMP-HYD<sub>1</sub>). The operational version of STOMP-HYD<sub>1</sub> also used four phase conditions, but was based on a three-phase scheme: 1) aqueous saturated w/o liquid CO<sub>2</sub>, 2) aqueous unsaturated w/o liquid CO<sub>2</sub>, 3) total-liquid saturated w/ liquid CO<sub>2</sub>, and 4) total-liquid unsaturated w/ liquid CO<sub>2</sub>.

For this version of the simulator (STOMP-HYD<sub>1</sub>), hydrate saturation was considered to be a secondary variable that was independent of the phase condition. The driving idea behind this approach was to minimize the number of phase conditions by taking advantage of the difference in hydrate phase equilibria between bulk conditions and in situ geologic media conditions as documented by (Klauda and Sandler, 2001). Hydrate saturation was calculated by first computing the bulk equilibrium pressure for hydrate as a function of temperature and concentration of hydrate formers. Next an equilibrium pressure ratio was computed from the bulk equilibrium pressure and the partial pressures of the hydrate formers. The equilibrium pressure ratio was then converted to a hydrate-aqueous interface radius, which was in turn converted to a hydrate-aqueous capillary pressure. The effective aqueous saturation was then determined from the hydrate-aqueous capillary pressure and the apparent aqueous saturation was determined from the gas-aqueous capillary pressure; where, hydrate was assumed to be totally occluded by the aqueous phase. The conceptual approach was modeled after the constitutive equations describing trapped NAPL saturation; where hydrate is

substituted for NAPL in the wettability order (i.e., aqueous > NAPL > gas). The constitutive equations and numerical solution approach for STOMP-HYD<sub>1</sub> are described in Appendix A. Simulations with STOMP-HYD<sub>1</sub> were published by Phale et al. (2006).

#### 2.4.2 STOMP-HYD<sub>2</sub>

The second version of the STOMP-HYD simulator (STOMP-HYD<sub>2</sub>) principally differed from the first (STOMP-HYD<sub>1</sub>) in the calculation approach for hydrate and additionally included an ice phase. As with STOMP-HYD<sub>1</sub> the concept of the hydrate-aqueous capillary pressure was maintained and extended to the ice phase. The calculation scheme, however, was altered. The approach implemented in STOMP-HYD<sub>2</sub> was one where the radius of curvature for the aqueous-hydrate and aqueous ice interfaces were computed as a function of the ratio of the actual temperature to the equilibrium temperature, which is computed as a function of the partial pressure of hydrate formers. The hydrate- and ice-aqueous capillary pressures are computed from the hydrate- and ice-aqueous interfacial tensions and radii of curvature, respectively:

$$P_h - P_l = \frac{2 \sigma_{hl}}{r_{hl}}; P_i - P_l = \frac{2 \sigma_{il}}{r_{il}} \quad (2.12)$$

where the hydrate-aqueous radius of curvature is computed from the difference in ex-situ hydrate equilibrium temperature and the system temperature (Jiang et al., 2001) and the ice-aqueous radius of curvature is computed from the difference in freezing point temperature and system temperature (Jiang et al., 2001):

$$r_{hl} = r_c \left[ 1 + \frac{(1 - \alpha)}{\log \left( \frac{T}{T^{ex}} \right)} \right]; r_{il} = r_c \left[ 1 + \frac{(1 - \alpha)}{\log \left( \frac{T}{T_{fp}^{ex}} \right)} \right]; r_c = 3.6 \times 10^{-9} \text{ m}; \alpha = 1.66 \quad (2.13)$$

Simulations with STOMP-HYD<sub>2</sub> were published by White and McGrail (2006).

#### 2.4.3 STOMP-HYD<sub>3</sub>

The first and second versions of STOMP-HYD relied on the shift in gas hydrate phase equilibria between bulk and geologic media conditions to compute phase capillary pressures and saturations. The equilibrium shift expression developed by Klauda and Sandler (2001) is a function of pore radius and is fairly weak except for relatively small pore radii. Turner and Sloan (2002) verified the form of the equilibrium shift curve, noting that for pore radii of 600 Å, the equilibria temperature shifts only -0.2% for methane hydrates. Whereas the numerical scheme implemented in STOMP-HYD<sub>1</sub> and STOMP-HYD<sub>2</sub> for computing hydrate saturations included the impact of pore structure on hydrate equilibria, the weak dependence on pore radii larger than 1000 Å, yielded an inefficient numerical solution scheme. The results of Turner and Sloan (2002) and poor numerical performance of these versions of STOMP-HYD suggested the need for a new approach.

In the third, and hence, current, version of the simulator (STOMP-HYD<sub>3</sub>), hydrate saturation was converted to a primary variable and the notion of gas hydrate phase equilibria being dependent on pore radii was abandoned. In STOMP-HYD<sub>1</sub> the partial pressures of hydrate formers were not equal to the hydrate equilibria pressure in the presence of gas hydrate, and in STOMP-HYD<sub>2</sub> the temperature was not equal to the hydrate equilibria temperature in the presence of gas hydrate. In STOMP-HYD<sub>3</sub> the partial pressure of hydrate formers equals the gas hydrate equilibria pressure and the temperature equals the hydrate equilibria temperature, when gas hydrate occurs. As indicated in Table 2.1, phase conditions for STOMP-HYD<sub>3</sub> are dependent on the occurrence of gas hydrate. Simulations with STOMP-HYD<sub>3</sub> were published by White and McGrail (2008a, b) and White et al. (2009).

## 2.5 Kinetic Exchange Option

In STOMP-HYD, it is assumed that the hydrate formers (i.e., guest molecules) are in thermodynamic equilibrium between phases. This implies that the CH<sub>4</sub> or CO<sub>2</sub> concentrations in the aqueous, gas, and hydrate phases can be computed from the known concentrations in one of these phases through expressions of thermodynamic equilibrium. When the time scales for transport between grid cells are longer than the time scales for phase partitioning, the assumption of thermodynamic equilibrium is appropriate. Low intrinsic permeabilities, large interphase surface areas, and thin fluid thickness characteristic of mobile fluid transport in geologic media generally create conditions where the equilibrium assumption is valid. Migration times for exchanging guest molecules in gas hydrates are characteristically slower versus the mobile fluid phases. If the time scales for transporting hydrate formers between grid cells is shorter than those for partitioning the hydrate formers between the fluid and solid phases, then equilibrium conditions do not model the system and thermodynamic equilibrium expressions cannot be used to determine phase concentrations.

An alternative to assuming thermodynamic equilibrium between phases is to rewrite the governing conservation equations with respect to the component masses in each phase with kinetic exchange terms for transport across phases. The drawback to this approach is the increased computational effort required to solve the coupled system of equations. Currently STOMP-HYD solves 4 (5 with salt or inhibitor) conservation equations at each grid cell. If the hydrate former component concentrations in each phase were treated as independent variables, then there would be 9 (10 with salt or inhibitor), assuming that the liquid-CO<sub>2</sub> phase was pure CO<sub>2</sub> and the inhibitor was soluble only in the aqueous phase. Increasing the number of primary unknowns from 4 to 9 would result in an increase in computational effort of nearly 8 times. A kinetic version of STOMP-HYD, referred to as STOMP-HYDk, has been developed that assumes thermodynamic equilibrium between hydrate-former components in the mobile phases (i.e., aqueous, gas, and liquid CO<sub>2</sub>) and nonequilibrium conditions between the hydrate-former components in the mobile and immobile phases, with a kinetic rate controlling the exchange of hydrate forming components between the mobile and immobile phases. This kinetic version of the simulator solves 6 (7 with salt or inhibitor) conservation equations at each grid cell: 1) thermal energy, 2) water mass, 3) mobile CH<sub>4</sub> mass, 4) mobile CO<sub>2</sub> mass, 5) hydrate CH<sub>4</sub> mass, and 6) hydrate CO<sub>2</sub> mass. The water and salt components are assumed to be in thermodynamic equilibrium across both mobile and immobile phases.

The mass conservation equations for the hydrate former components in STOMP-HYD are shown in Eqn. (2.1). For STOMP-HYDk, these equations are split into mobile and immobile fractions:

$$\begin{aligned} \frac{d}{dt} \int_V \sum_{\gamma=l,n,g} \left( \phi \omega_\gamma^i \rho_\gamma s_\gamma \right) dV &= \int_\Gamma \sum_{\gamma=l,n,g} \omega_\gamma^i \rho_\gamma \mathbf{V}_\gamma \cdot \mathbf{n} d\Gamma \\ &+ \int_\Gamma \sum_{\gamma=l,n,g} \mathbf{J}_\gamma^i \cdot \mathbf{n} d\Gamma + \int_V m^i dV - K_h \left( P_g^i - \varphi_g^i P_h^{eq} \right); \text{ for } i = CO_2, CH_4 \end{aligned} \quad (2.14)$$

$$\frac{d}{dt} \int_V \sum_{\gamma=h} \left( \phi \omega_\gamma^i \rho_\gamma s_\gamma \right) dV = K_h \left( P_g^i - \varphi_g^i P_h^{eq} \right); \text{ for } i = CO_2, CH_4 \quad (2.15)$$

where, the mobile and immobile fractions of the hydrate-former components are linked through a kinetic exchange term. In the limit, the kinetic exchange term yields equilibrium conditions between the mobile and immobile fractions, by formulating the kinetic term as a function of the difference between the component partial pressure and equilibrium partial pressure. Currently we are not aware of an expression for the kinetic exchange coefficient, shown in Eqns. (2.14-2.15), but estimates could be made from gas hydrate guest molecule exchange experiments. Whereas the number of primary variables is greater for STOMP-HYDk compared with its equilibrium counterpart, STOMP-HYD, only 2 primary variable sets are needed in STOMP-HYDk to define the system state, as shown in Table 2.2. The STOMP-HYDk simulator has been demonstrated on simple code verification problems, but is currently considered as being under development and has not been applied to field-scale production problems.

**Table 2.2.** STOMP-HYDk primary variable sets and ancillary equations.

Phase Condition #1 (no liquid CO2) - $s_l \leq 1, s_g \geq 0, s_n = 0, s_h \geq 0, s_i \geq 0$					
Energy - $T$	H2O Mass - $P_l$	Mobile CH4 Mass - $P_g^{CH_4}$	Mobile CO2 Mass - $P_g^{CO_2}$	Hydrate CH4 Mass - $P_{heq}^{CH_4}$	Hydrate CO2 Mass - $P_{heq}^{CO_2}$
$P_g = \max \left[ \left( P_l + \frac{\beta_{gl}}{\psi} \right), \left( P_g^{CO_2} + P_g^{CH_4} + P_g^{H_2O} \right) \right], P_n = P_n^c,$ $P_h^{eq} = P_{heq}^{CO_2} + P_{heq}^{CH_4}, T_h^{eq} = \text{func} \left[ P_h^{eq}, \varphi_g^{CH_4} \right]$					
Phase Condition #2 (liquid CO2) - $s_l \leq 1, s_g \geq 0, s_n > 0, s_h \geq 0, s_i \geq 0$					
Energy - $T$	H2O Mass - $P_l$	Mobile CH4 Mass - $P_g^{CH_4}$	Mobile CO2 Mass - $P_n$	Hydrate CH4 Mass - $P_{heq}^{CH_4}$	Hydrate CO2 Mass - $P_{heq}^{CO_2}$
$P_g = \max \left[ \left( P_l + \frac{\beta_{gl}}{\psi} \right), \left( P_g^{CO_2} + P_g^{CH_4} + P_g^{H_2O} \right) \right], P_g^{CO_2} = P_{sat}^{CO_2},$ $P_h^{eq} = P_{heq}^{CO_2} + P_{heq}^{CH_4}, T_h^{eq} = \text{func} \left[ P_h^{eq}, \varphi_g^{CH_4} \right]$					



### 3.0 Class 1 and 2 Gas Hydrate Accumulations

Class 1 gas hydrate accumulations are characterized by a permeable hydrate-bearing interval overlying a permeable interval with mobile gas, sandwiched between two impermeable intervals. Depressurization-induced dissociation is currently the favored technology for producing gas from Class 1 gas hydrate accumulations. The depressurization production technology requires heat transfer from the surrounding environment to sustain dissociation as the temperature drops toward the hydrate equilibrium point, and leaves the reservoir void of gas hydrate. Production of gas hydrate accumulations by exchanging carbon dioxide with methane in the clathrate structure has been demonstrated in laboratory experiments and proposed as a field-scale technology. The carbon dioxide exchange technology has the potential for yielding higher production rates and mechanically stabilizing the reservoir by maintaining hydrate saturations. We used numerical simulation to investigate the disadvantages and advantages of using carbon dioxide injection to enhance the production of methane from Class 1 gas hydrate accumulations. Numerical simulations in this study were primarily concerned with the mechanisms and approaches for production enhancements with carbon dioxide injection. To avoid excessive simulation execution times, a five-spot well pattern with a 500-m well spacing was approximated using a two dimensional domain, having well boundaries on the vertical sides and impermeable boundaries on the horizontal sides. Impermeable over- and under burden were included to account for heat transfer into the production interval. Simulation results indicate that low injection pressures can be used to reduce secondary hydrate formation and that direct contact of injected carbon dioxide with the formation methane hydrate is limited due to bypass through the higher permeability gas zone.

The U.S. Department of Energy (DOE) and British Petroleum Exploration Alaska, Inc. (BPXA) have been conducting a joint research project to explore and characterize the Alaska North Slope (ANS) gas hydrate accumulations with the perspective of developing this potential unconventional energy resource (Hunter et al., 2008). USGS estimates a mean value of 16.7 trillion cubic meters (TCM) of natural gas in gas hydrate accumulations on the ANS, of which 0.93 TCM were estimated to occur within the shallow sand reservoirs beneath the ANS production infrastructure within the Eileen trend (Hunter et al., 2008). The Eileen and Tarn trends are gas hydrate accumulations beneath the petroleum industry infrastructure within the Milne Point Unit (MPU), Prudhoe Bay Unit (PBU), and Kuparuk River Unit. A key component of this gas hydrate resource assessment project was the drilling of and data acquisition from the Mount Elbert-01 stratigraphic test well, completed in February 2007, and the subsequent numerical simulation of the pumping experiments conducted with the Modular Dynamics Testing (MDT) downhole tool (Anderson et al., 2008). These simulations were conducted as part of the DOE sponsored international code comparison activities for gas hydrate simulators (Wilder et al., 2008).

Gas hydrate saturation logs from the Mount Elbert-01 well, based on combinable magnetic resonance data, indicate two gas-hydrate bearing sands of 7.9 to 22.9 meters thick. Both the upper zone (D) and lower zone (C) show variable gas-hydrate saturations, reaching maximum values of 0.85 with the remaining pore space being filled with water. Figure 3.1 shows hydrate saturation and thickness maps of the D and C zones, estimated from seismic surveys<sup>1</sup>. Boswell et al. (2008) reports slightly different numbers: 16m of hydrate rich sand (65% saturation) for C-sand and 14m of hydrate bearing sand (65% saturation) for the D sand. These two onshore ANS gas-hydrate bearing

---

<sup>1</sup> Zhu, T, and H Phale. 2005, "Personal Communication of Data from University of Alaska, Fairbanks, Ak."

sands are target reservoirs for developing and demonstrating production technologies. The knowledge and experience gained from onshore investigations will be an important component in assessing the potential of the marine gas hydrate resource. Whereas depressurization is the leading candidate technology for producing gas hydrates from the ANS reservoirs, there is insufficient evidence from pilot-scale experiments to determine whether production is commercially feasible.

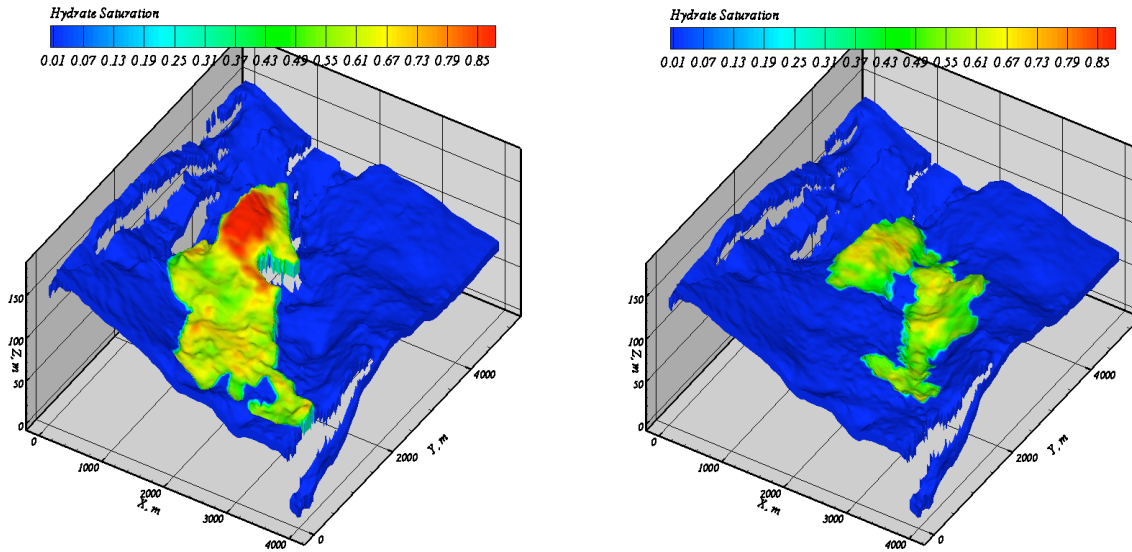


**Figure 3.1** Gas hydrate saturation and thickness maps of the D (left) and C (right) gas-hydrate bearing sands. Faults are shown as map offsets (Zhu and Phale, 2005).

To support the objectives of the joint research project by DOE and BPXA on assessing the resource potential of gas hydrates on the ANS, this section of the report investigates the benefits of using carbon dioxide injection as a component of a production strategy. Dissociation-based production technologies (i.e., depressurization, thermal stimulation, and inhibitor injection) convert solid gas hydrate into gas and liquid, changing the mechanical strength of the hydrate-bearing interval. Rudqvist and Moridis (2007) demonstrated through numerical simulation the potential for subsidence when producing a Class 3 hydrate accumulation using depressurization. Carbon dioxide injection has the potential of maintaining gas hydrate saturation during production through the guest molecule exchange process. Depressurization results in rapid initial gas production rates with rapid cooling of the reservoir at the dissociation front as the temperature near the front drops to the gas hydrate equilibrium temperature at the reduced reservoir pressure. After this initial stage, gas hydrate production is dependent on heat transfer into the dissociation front. An economic drawback to gas hydrate production through depressurization is the cost of co-producing water. Carbon dioxide injection has the potential of increasing production rates and decreasing production costs by avoiding further dissociation at the production front (Wilder et al., 2008). The greatest potential drawback to carbon dioxide injection is secondary hydrate formation and reduced formation permeability, including clogging. This section of the report explores both the benefits and disadvantages of using carbon dioxide injection in producing a Class 1 hydrate accumulation.

### 3.1 Simulation Scenarios

The production of Class 1 through 4 hydrates using depressurization and thermal stimulation have been numerically investigated by Moridis and Collett (2003), Moridis et al. (2007), Moridis (2004), and Moridis and Sloan (2007). The Class 1 gas hydrate reservoir considered for this section of the report is identical to the Class 1W, Reference Case, defined by Moridis et al. (2007), which is representative of a permafrost accumulation. This reservoir comprises three 30-m-thick strata; a permeable sandstone overlain and underlain by impermeable shale layers. The upper half of the permeable sandstone layer is gas hydrate bearing without free gas, whereas the lower half is a variably saturated gas-aqueous system. Initially the gas and gas-hydrate comprise only methane. To maintain stable initial conditions, preventing the downward migration of aqueous phase and upward migration of gas phase across the gas-hydrate lower boundary, a gas hydrate saturation dependent entry pressure model was implemented, following Moridis et al. (2007). The Moridis model for capillary-pressure function used a variant of the Brooks-Corey function (Brooks and Corey, 1966) which included an effective-aqueous saturation dependent smoothing function, based on the *error function*, and a gas-hydrate saturation dependent entry pressure function, based on the *regularized incomplete beta function*:

$$\bar{s}_l = \frac{s_l - s_{lr}}{1 - s_{lr}} = \left( \frac{\psi}{(h_{gl}) H(s_h) F(\bar{s}_l)} \right)^\lambda;$$

$$F(\bar{s}_l) = \text{erf} \left[ 60(1 - \bar{s}_l) \right]; H(s_h) = 1 + 9.28 \left( \frac{B(s_h; 2.1, 2.2)}{B(2.1, 2.2)} \right) \quad (3.1)$$

The capillary-pressure function used for this section of the report altered the Moridis model by eliminating the smoothing function and replacing the *regularized incomplete beta function* with a *sinusoid function*:

$$s_l = \frac{\left[ \frac{s_l}{(1 - s_h - s_i)} \right]^{-s_{lr}} - s_{lr}}{(1 - s_{lr})} = \left( \frac{\psi}{(h_{gl}) \beta_{gl} H(s_h)} \right)^\lambda;$$

$$H(s_h) = 1 + 9.28 \left( 5.6075 + 4.6567 \sin \left[ 3.1275 s_h - 1.5166 \right] \right) \quad (3.2)$$

Formation properties for the permeable (sandstone) and impermeable (shale) intervals are shown in Table 3.1.

Protocols for injecting carbon dioxide into natural gas-hydrate bearing formations to enhance gas production have not been established. Previous numerical simulation studies (White and McGrail, 2008a, b) have demonstrated the benefits of depressurizing the formation prior to injecting carbon dioxide, by increasing the formation permeability to the mobile phases and inhibiting the creation of secondary gas hydrate. The numerical simulations executed for this section of the report were focused on quantifying the benefits of injecting carbon dioxide into a Class 1 gas hydrate accumulation after depressurizing the system to 4 MPa for a period of 6 months. The vertical geometry and initial conditions prior to the depressurization stage is based on earlier studies of Class 1 gas hy-

drate accumulations of Moridis et al. (2007) that used conditions and hydrologic parameters representative of ANS accumulations. Moridis et al. (2007) used a 2D cylindrical grid with a reservoir radius of 567.5 m and permeable interval thickness of 30 m. For this investigation, a 2D Cartesian grid was used with a 500-m spacing between the injection "well" and production "well," where for the 2-dimensional Cartesian geometry the wells are line sources and sinks. As in the Moridis et al. (2007) geometry, the reservoir thickness was 30 m.

### 3.1.1 System Initialization

As noted by Moridis et al. (2007) the initial condition state for a Class 1 gas hydrate accumulation cannot be generated using conventional functions for the relative permeability-saturation-capillary pressure (k-s-P) characteristics. In using conventional functions, the gas pressure below the overlying gas hydrate-bearing zone would exceed the entry pressure, causing the aqueous phase to drain and gas to enter the zone. We know, however, that Class 1 gas-hydrate configurations occur in nature. To reconcile this issue, Moridis et al. (2007) proposed three hypotheses for altering the conventional k-s-P functions to account for these observations. The first hypothesis was that gas hydrates alter the irreducible aqueous saturation, making the aqueous phase immobile. This hypothesis is contradicted, however, by the moderate aqueous phase permeability measured for sandstones with hydrate saturations of 0.8 (Kurihara et al., 2005). The second hypothesis was that a thin impermeable zone of high gas hydrate saturation formed at the interface between the gas-hydrate bearing and free-gas intervals. This approach has two numerical drawbacks. The more important drawback is that when using conventional k-s-P functions the system is not stable and only delays drainage of the aqueous phase from the hydrate-bearing interval by temporarily creating an ultra-low permeability layer.

The third hypothesis was that gas hydrate alters the capillary pressure or non-wetting fluid entry pressure characteristic. This approach is conventional for multifluid systems, as shown in Equations 2.6 through 2.9, where the capillary pressure is scaled by fluid-pair interfacial tensions. This allows use of k-s-P functions that are experimentally determined on one fluid pair (e.g., water-air) to be extended to other fluid pairs (e.g., water-liquid CO<sub>2</sub>). It's reasonable to expect that gas-hydrates would alter capillarity in geologic media. Field data from the ANS of Kurihara et al. (2005) support this notion. In application, this hypothesis suggests that the non-wetting fluid (i.e., gas) entry pressure increases with increasing gas hydrate saturation. The functional forms developed to describe this relationship developed by Moridis et al. (2007) include a smoothing factor and an evaluation of an incomplete beta function, as shown in Equation 3.1. For the numerical simulation in this study, the smoothing factor was eliminated and the hydrate scaling factor for capillary pressure of Moridis et al. (2007) was matched using a sinusoidal function, as shown in Equation 3.2.

### 3.1.2 Simulation Stages

Numerical simulations were conducted in three stages: 1) initialization, 2) depressurization, and 3) carbon dioxide injection. The initialization stage was used to establish phase pressure and saturation profiles. These simulations used a hydrologically closed system (no fluid migration across the boundaries) with fixed temperatures along the top (11.65° C) and bottom (15.42° C) of the impermeable shale layers. The 30-m permeable sandstone reservoir was divided into two intervals; a hydrate and aqueous phase saturated interval (hydrate zone) overlying a gas and aqueous saturated interval (gas zone). The boundary between the hydrate and gas zones was defined by hydrate stability for pure methane hydrate. In the hydrate zone the initial gas-hydrate saturation was 0.7. In both the hydrate and gas zones, the aqueous pressure was initiated with a hydrostatic gradient, as-

signing a pressure of 10.54 MPa at the hydrate-gas interface. In the hydrate zone the methane gas pressure is determined from the methane hydrate equilibrium pressure, which is less than the aqueous pressure, yielding a hydrate-aqueous saturated system. In the gas zone the gas pressure was initiated with a uniform pressure of 10.60 MPa, yielding partially aqueous saturated conditions at the top of the gas zone and fully aqueous saturated conditions at the bottom of the interval. Initialization simulations were executed to establish steady conditions, prior to executing the transient depressurization and carbon dioxide injection simulation stages.

Depressurization of a methane gas-hydrate reservoir yields rapid production of methane gas with an associated drop in temperature at the dissociation front. Further dissociation requires heat transport from surrounding regions to the dissociation front. As production continues, the entire reservoir temperature drops toward the equilibrium temperature for the production-well pressures. The evolution of methane gas production, methane gas release from gas-hydrate dissociation, and water production is shown in Figure 3.2, where the boundary pressure over both the hydrate and gas zones was reduced to 4 MPa for a period of 1 year. Comparison between these simulation results and those generated by Moridis et al. (2007) were not made due to the differences in the grid configurations. The simulations of Moridis et al. (2007) used a single production well within a cylindrical domain with a 500-m radius, whereas, the simulations reported here used two line production wells with a 500-m spacing. After 6 months, methane production rates are declining, which opens the question as to whether carbon dioxide injection can improve production rates over the next 6 months of production, while maintaining hydrate saturations for mechanical stability.

Carbon dioxide can be injected into a gas-hydrate reservoir using various forms, temperatures, and strategies. A series of 36 simulations were conducted that considered three variations in the injectant form (i.e., pure CO<sub>2</sub>, 50% volumetric aqueous micro-emulsion, and aqueous dissolved CO<sub>2</sub>), two variations in the injectant temperature (i.e., 20° and 50° C), three variations in the injection pressure (i.e., 6 MPa, 8 MPa, and 10 MPa), and two variations in the injection strategy (i.e., inject across the hydrate zone only, and inject across both the hydrate and gas zones). During the carbon dioxide injection stage, the production well was closed across the gas zone and only produced from the hydrate zone. A matrix showing the simulation scenarios for the carbon dioxide injection stage is shown in Table 3.1. The suite of injection scenarios selected for this numerical investigation represents a straightforward approach to using carbon dioxide injection to enhance the production of gas hydrate from Class 1 accumulations following an initial depressurization production stage. Other innovative approaches, such as those involving hydraulic fracturing of the formation or dormant pumping periods, are not considered in the suite of scenarios.

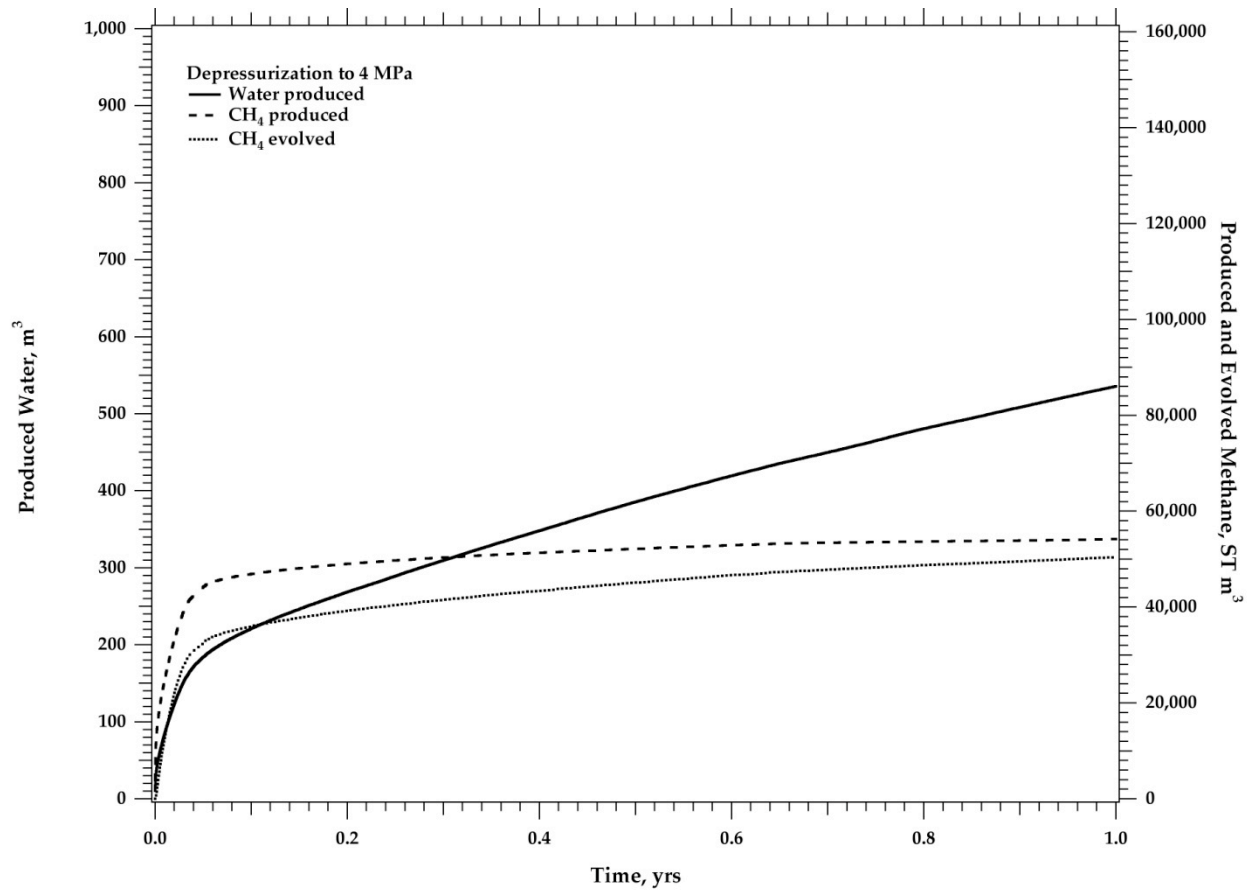


**Figure 3.2.** Produced water, produced methane, and evolved methane following depressurization at 4 MPa for 1 year across the hydrate and gas zones [S-0].

**Table 3.1.** Class 1 Gas Hydrate Accumulation Simulation Scenarios

Injection Zone	Injectant	CO <sub>2</sub> State	Injection Press.,MPa	Injection Temp., C	Injectant Density, kg/m <sup>3</sup>	CO <sub>2</sub> Arrival, yr	Average Time Step, s	Simulation ID
Gas and Hydrate Zones	Pure CO <sub>2</sub>	Liquid	6	20	778.8	0.567	4.7E+2	S1
		Liquid	8	20	829.0		1.1E+0	S2
		Liquid	10	20	856.4		7.0E-1	S3
		Gas	6	50	135.0	0.566	2.0E+2	S4
		Supercritical	8	50	217.3		6.0E-1	S5
		Supercritical	10	50	383.3		9.0E-1	S6
	50% Micro-emulsion	Liquid	6	20	389.4	0.681	3.4E+2	S7
		Liquid	8	20	414.5		2.3E+0	S8
		Liquid	10	20	428.2		2.4E+0	S9
		Gas	6	50	67.5	0.618	7.0E+2	S10
		Supercritical	8	50	108.7		7.0E-1	S11
		Supercritical	10	50	191.7		1.1E+1	S12
	Aqueous Dissolved CO <sub>2</sub>	Dissolved	6	20	66.1	none	2.0E+3	S13
		Dissolved	8	20	69.5	0.885	2.4E+2	S14
		Dissolved	10	20	72.6		1.0E+0	S15
		Dissolved	6	50	37.0	none	8.2E+3	S16
		Dissolved	8	50	44.8	0.864	5.9E+3	S17
		Dissolved	10	50	50.2	0.731	5.7E+2	S18
Hydrate Zone	Pure CO <sub>2</sub>	Liquid	6	20	778.8	0.565	1.3E+3	S19
		Liquid	8	20	829.0		1.2E+0	S20
		Liquid	10	20	856.4		1.2E+0	S21
		Gas	6	50	135.0	0.557	2.4E+2	S22
		Supercritical	8	50	217.3		4.0E-1	S23
		Supercritical	10	50	383.3		1.3E+1	S24
	50% Micro-emulsion	Liquid	6	20	389.4		1.4E+1	S25
		Liquid	8	20	414.5		3.4E+0	S26
		Liquid	10	20	428.2		2.5E+0	S27
		Gas	6	50	67.5	0.607	3.3E+2	S28
		Supercritical	8	50	108.7		6.0E-1	S29
		Supercritical	10	50	191.7		2.0E-1	S30
	Aqueous Dissolved CO <sub>2</sub>	Dissolved	6	20	66.1	none	2.4E+3	S31
		Dissolved	8	20	69.5		1.6E+1	S32
		Dissolved	10	20	72.6		1.9E+1	S33
		Dissolved	6	50	37.0	none	7.5E+3	S34
		Dissolved	8	50	44.8	0.882	5.7E+3	S35
		Dissolved	10	50	50.2	0.744	1.3E+3	S36

## 3.2 Simulation Results

Prior to injecting carbon dioxide into the formation, the reservoir was produced by depressurizing both ends of the domain across both the hydrate and gas zones. A plot of the produced methane and water (i.e., extracted from the reservoir) and evolved methane (i.e., released from the hydrate) is shown in Figure 3.2 as the three black lines. Initially the reservoir contains 160,000 ST m<sup>3</sup> of methane in gas hydrate, free gas, and dissolved form. Methane and water are produced rapidly for the first 0.05 years. Then as the pressure and temperature drop in the formation, production rates diminish as the dissociation process becomes dependent on heat transfer into the hydrate zone. To serve as a benchmark, the depressurization process was simulated for a one-year period. During the six-month depressurization stage, approximately 34% of the initial methane is produced from the reservoir and 31% is evolved; where, produced refers to the methane that enters the production well, and evolved refers to the methane liberated from the hydrate structure.

Injection of carbon dioxide was started from the depressurization conditions at 0.5 years, using the restarting capabilities of the simulator. Carbon dioxide in one of three forms (i.e., pure CO<sub>2</sub>, 50% volumetric CO<sub>2</sub> micro-emulsion, or dissolved CO<sub>2</sub>) was injected along the left-hand boundary, with the right-hand boundary being maintained at 4 MPa across the hydrate zone only. This differs from the depressurization simulation, where production pressures were maintained across both the hydrate and gas zones. The injection simulations were halted when one of three conditions was realized: 1) total simulation time reached 1 year, 2) gas mass fraction of CO<sub>2</sub> in the production well exceeded 5%, or 3) secondary hydrate development clogged the injection. The gas saturation and hydrate saturation profiles after the depressurization period of 0.5 years are shown in Figures 3.3 and 3.4, respectively. Depressurization causes dissociation of the gas hydrate and creation of gas saturation both within the hydrate and gas zones. Hydrate saturations in the hydrate zone are reduced to zero near the top of the hydrate zone where heat transfer from the upper impermeable shale interval is rapid. Lower in the hydrate zone, hydrate saturations are reduced from the initial value of 0.7 to 0.55 through dissociation. Secondary hydrate is predicted to form during the depressurization near both ends of the gas zone.

### 3.2.1 Combined Hydrate- and Gas-Zone Injection Scenarios

The initial depressurization stage was designed to extract the readily available methane and to increase the effective permeability of the hydrate zone to mobile fluids. Exchanging carbon dioxide for methane as the guest molecule in gas hydrates occurs where carbon dioxide comes in contact with methane gas hydrates. A series of carbon dioxide injection scenarios [S1 through S18] were studied that varied the form of the injected fluid and the injection screened interval. To promote carbon dioxide contact with the resident methane hydrate, the production well was only screened over the hydrate zone. Injection over two different screened intervals was considered: 1) combined hydrate and gas zones [S1 through S18], and 2) hydrate zone only [S19 through S36]. Carbon dioxide injections into the gas zone only were additionally simulated but not reported, because the simulation results indicated little contact of carbon dioxide with the residual methane hydrate, and flow patterns that were predominately through the gas zone. This section describes the simulation results for the injection scenarios for the combined hydrate- and gas-zone screened interval.

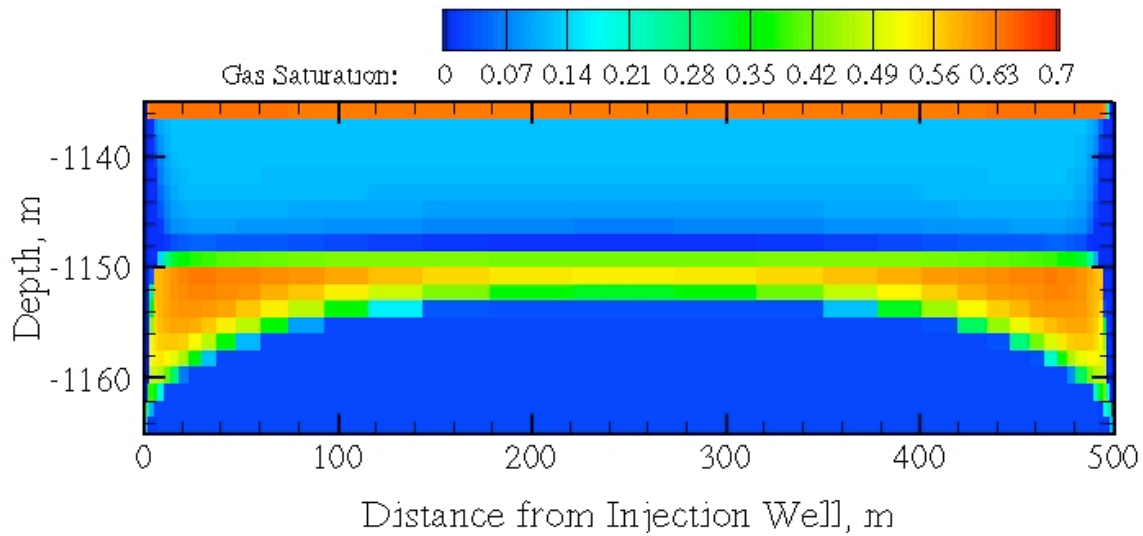


**Figure 3.3.** Gas saturation after depressurization at 4 MPa for 6 months at both ends across the gas and hydrate zones [S0].

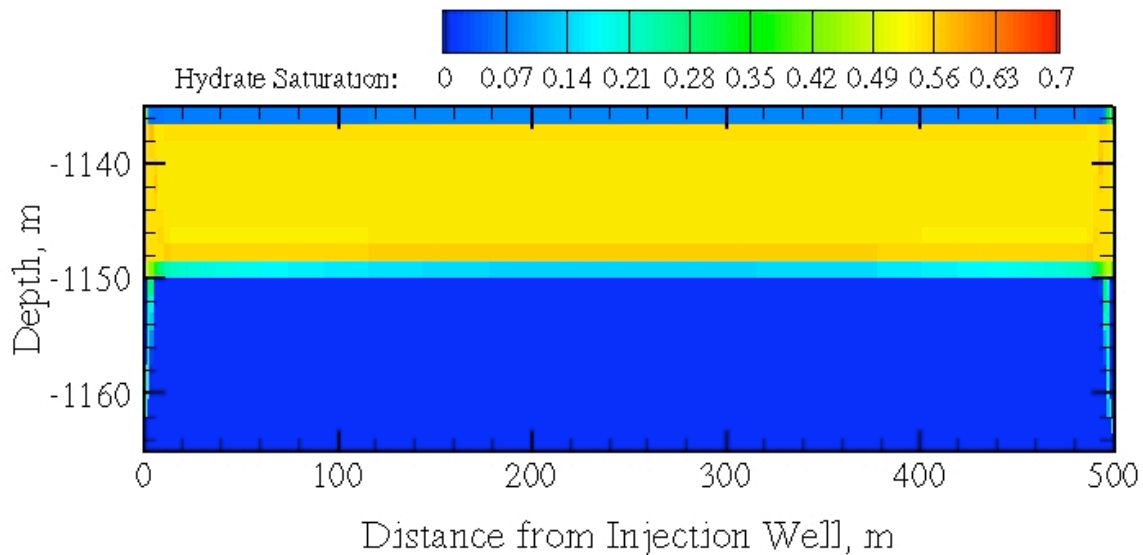


**Figure 3.4.** Hydrate saturation after depressurization at 4 MPa for 6 months at both ends across the gas and hydrate zones [S0].

### 3.2.1.1 Pure CO<sub>2</sub> Injection [S1 through S6]

A series of six simulations [S1 through S6] were executed that investigated the injection of carbon dioxide directly into the reservoir through well-casing screens across both the hydrate and gas zones. For the range of conditions at the injection point (i.e., pressures of 6 MPa, 8 MPa, and 10 MPa; and temperatures of 20° C and 50° C), the thermodynamic state of the carbon dioxide varied

from being liquid CO<sub>2</sub>, to subcritical gas, to supercritical gas, as shown in Table 3.1. Simulation results for the produced water, produced methane, and evolved methane for the injection of pure CO<sub>2</sub> at 6 MPa indicate nearly identical results for the 20° C [S1] and 50° C [S4] injectant for the first month of injecting, as shown in Figure 3.5. After the first month, the 50°C injectant [S4] yields additional evolved and produced methane from the exchange of carbon dioxide with methane in the hydrate near the production well. The net effect of injecting pure CO<sub>2</sub> at 6 MPa for 6 months after a 6-month depressurization period is the production of additional 11.5% [S1] or 13.1% [S4] of the original methane mass in the reservoir.

Breakthrough of the carbon dioxide, however, occurs only after 26 days of injecting pure CO<sub>2</sub> at 6 MPa at both 20° C [S1] and 50° C [S4], significantly reducing these additional production quantities. The principal mechanism for the enhanced methane production is not via carbon dioxide and methane exchange, as shown in Figure 3.5 from the lack of additional evolved methane from hydrate, but by the displacement of the gaseous methane in the gas zone from the injection of pure gaseous or liquid CO<sub>2</sub>. Regardless of the original state of injected CO<sub>2</sub> at 6 MPa, liquid CO<sub>2</sub> forms in the reservoir, as shown in Figure 3.6 [S1]. Because the injected CO<sub>2</sub> principally circumvents the hydrate zone, exchange of carbon dioxide with methane as the hydrate guest molecule is limited to regions where hydrate is exposed to carbon dioxide. An indicator of the carbon dioxide distribution is the fraction of carbon dioxide of hydrate formers in all phases, which will be referred to as the CO<sub>2</sub> fraction of formers. Figure 3.7 shows the CO<sub>2</sub> fraction of formers after injecting pure CO<sub>2</sub> for 6 months at 6 MPa at 50° C [S4], which indicates a lack of carbon dioxide within the core of the hydrate zone.

Simulations for pure CO<sub>2</sub> injection at higher pressures (i.e., 8 MPa [S2, S5] and 10 MPa [S3, S6]) require small time steps to resolve the complex phase states and transitions; average time step lengths, calculated for the injection period, are shown in Table 3.1. Although the higher pressure simulations were halted prior to reaching the stopping criteria, results at early times provide sufficient data to understand the processes. Injection of pure CO<sub>2</sub> at the higher pressure yielded secondary hydrate formation around the well in both the hydrate and gas zones, forcing the injected fluid to circumvent the hydrate zone and migrate through the gas zone. Liquid CO<sub>2</sub> formed in the gas zone, as shown in Figure 3.8 [S6], and would be anticipated to continue migrating across the gas zone to the producing well, displacing gaseous methane and exchanging carbon dioxide with methane hydrate along the gas- and hydrate-zone interface.

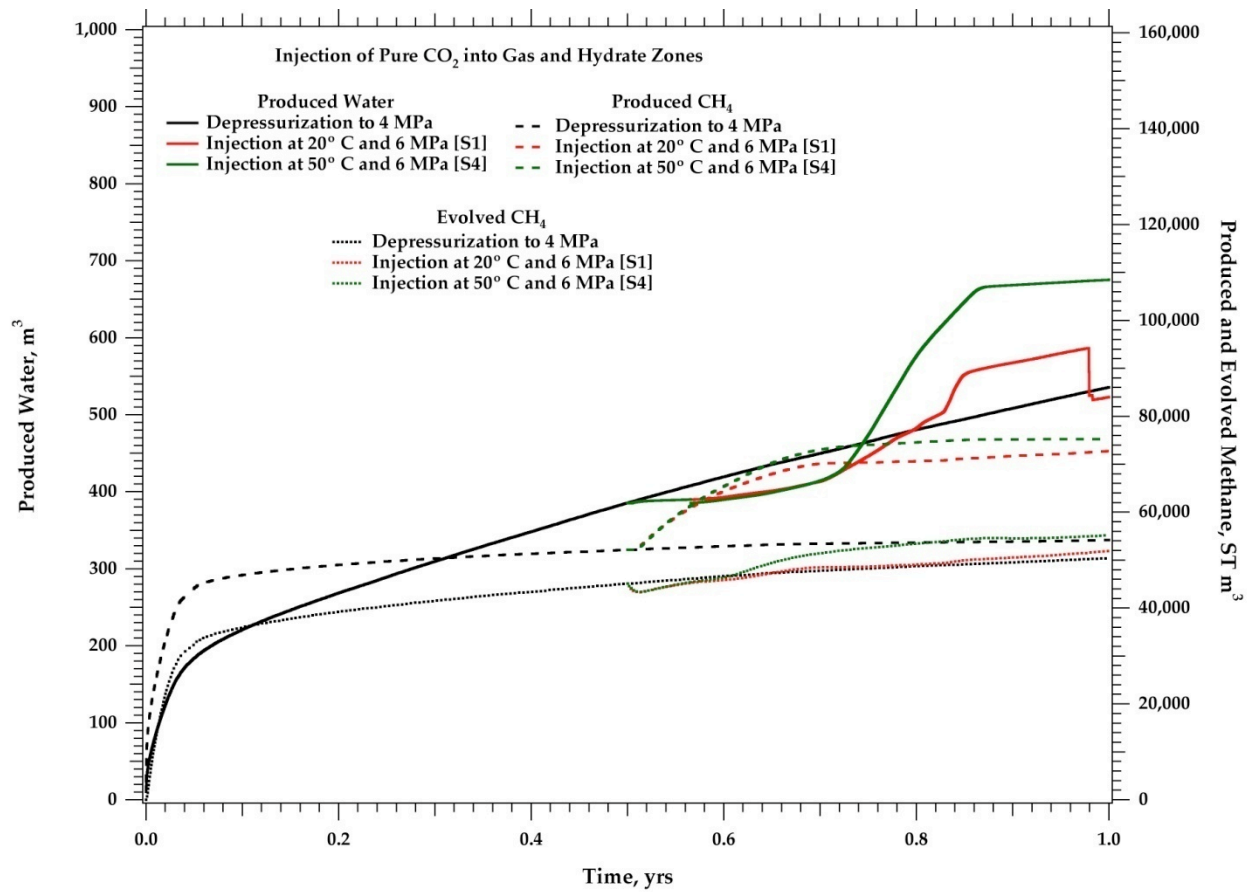


**Figure 3.5.** Produced water, produced methane, and evolved methane during pure CO<sub>2</sub> injection at 6 MPa across the hydrate and gas zones, producing at 4 MPa across the hydrate zone only, initiated from the 6-month depressurization stage at 4 MPa [S1 and S4].

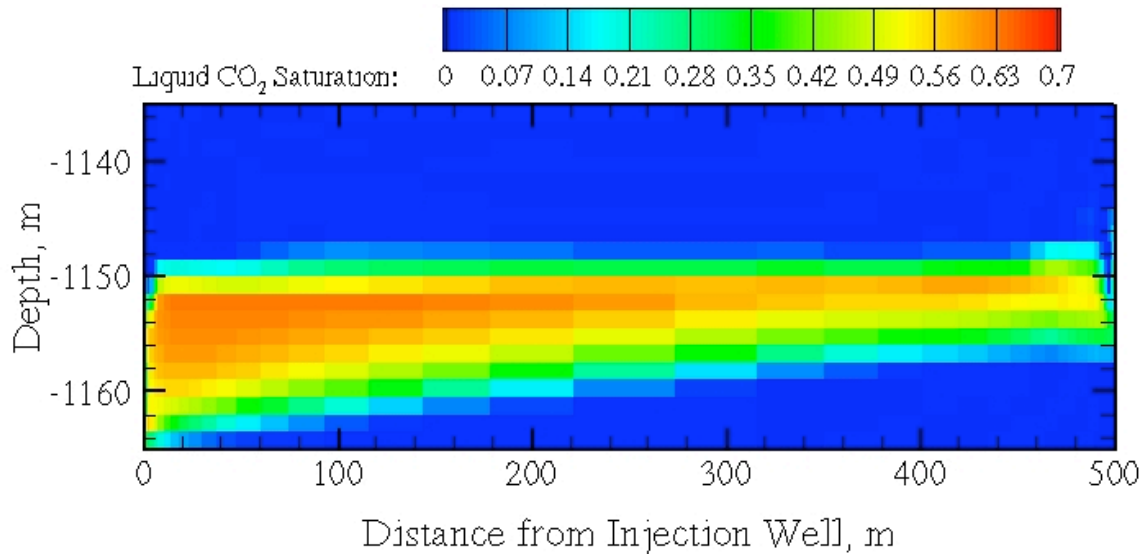


**Figure 3.6.** Liquid CO<sub>2</sub> saturation profile in the hydrate and gas zones after pure CO<sub>2</sub> injection at 6 MPa at 20°C for 6 months across the hydrate and gas zones, producing at 4 MPa across the hydrate zone only after the 6-month depressurization stage at 4 MPa [S1].

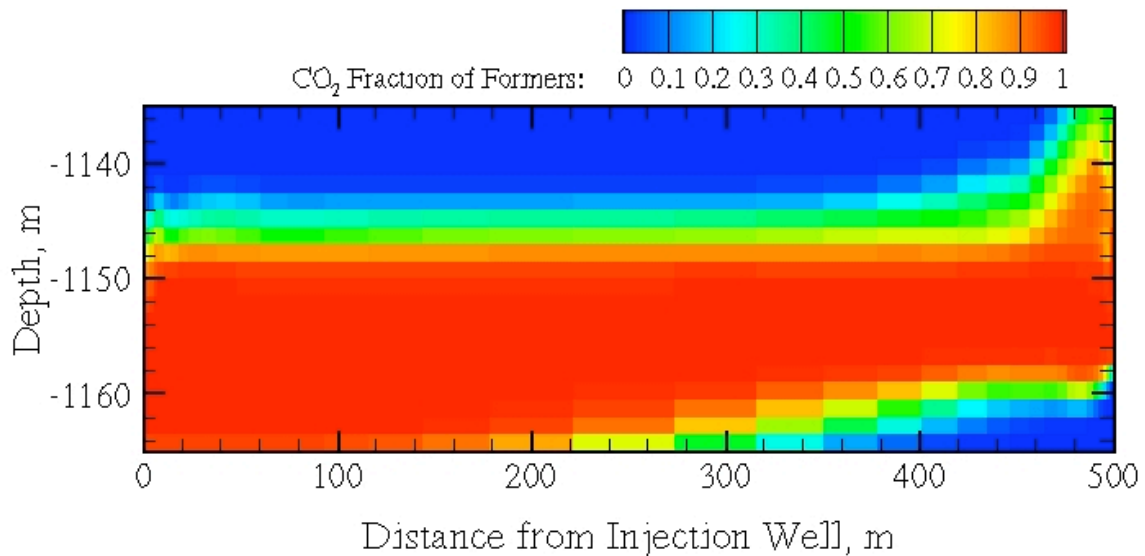


**Figure 3.7.** "CO<sub>2</sub> fraction of formers" profile in the hydrate and gas zones after pure CO<sub>2</sub> injection at 6 MPa at 50° for 6 months across the hydrate and gas zones, producing at 4 MPa across the hydrate zone only after the 6-month depressurization stage at 4 MPa [S4].

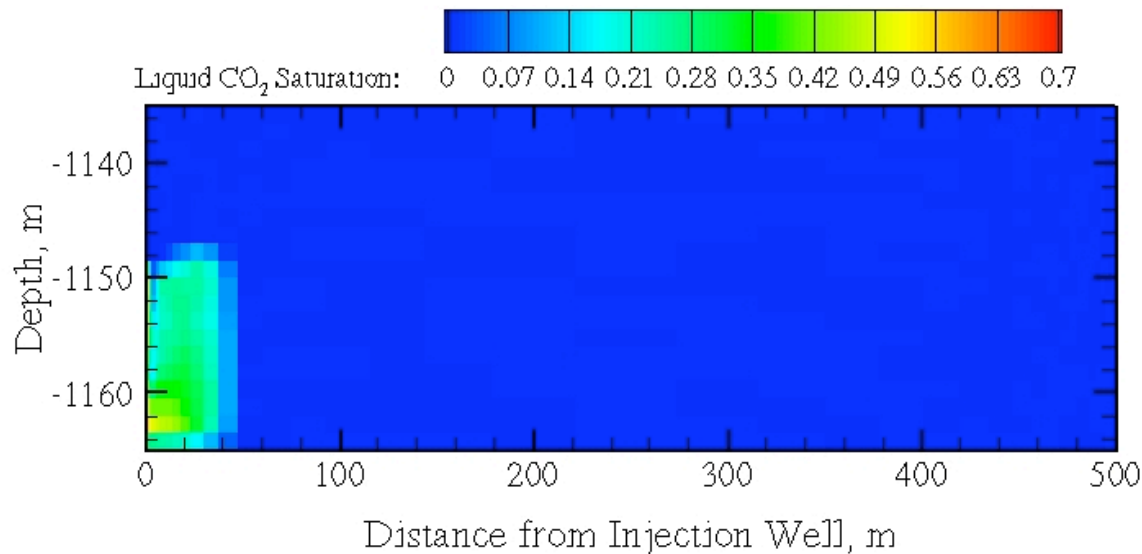


**Figure 3.8.** Liquid CO<sub>2</sub> profile in the hydrate and gas zones after pure CO<sub>2</sub> injection at 10 MPa at 50°C for 0.3 days across the hydrate and gas zones, producing at 4 MPa across the hydrate zone only after the 6-month depressurization stage at 4 MPa [S6].

### 3.2.1.2 50% Volumetric CO<sub>2</sub> Micro-emulsion Injection [S7 through S12]

This section discusses the series of six simulations [S7 through S12] that investigated the injection of carbon dioxide as a 50% volumetric micro-emulsion into the reservoir through well-casing screens across both the hydrate and gas zones. Injection of carbon dioxide as a micro-emulsion was assumed to occur through an in-well micro-emulsion generator, in a closed loop with the produced water, decreasing the pumping costs for the liquid water carrier fluid. Whereas a micro-emulsion is formed in the well casing, the STOMP-HYD simulator assumes that phase separation occurs immediately in the formation (i.e., the micro-emulsion moves through the pore space as aqueous, liquid CO<sub>2</sub>, and gas phases). For the range of injection conditions, the thermodynamic state of the carbon dioxide in the micro-emulsion varied across the scenarios from being liquid CO<sub>2</sub>, to subcritical gaseous CO<sub>2</sub>, to supercritical CO<sub>2</sub>. The thermodynamic state of the carbon dioxide in the micro-emulsion affects the density of carbon dioxide in the injectant, for the constant volumetric ratio of 50% emulsion and 50% liquid water, as shown in Table 3.1. Simulation results for produced water, produced methane, and evolved methane with the injection of a 50% (volumetric) carbon dioxide micro-emulsion indicate that an additional 12% of original methane mass is produced for the injection pressures of 6 MPa, as shown in Figure 3.9 [S7, S10]. A majority of the additional produced gas results from displacement of the gas phase in the gas zone as shown by comparing the gas saturation profile after depressurization (Figure 3.3) [S0] with that after injecting 50% carbon dioxide micro-emulsion for 6 months (Figure 3.10) [S10].

A small fraction of the injected carbon dioxide forms gas hydrate or replaces methane in the hydrate structure as the guest molecule. Figure 3.11 [S10] shows the product of the CO<sub>2</sub> mass fraction of formers in the hydrate times the hydrate saturation at 6 months after the start of the 50% carbon dioxide micro-emulsion injection. Breakthrough of carbon dioxide in the production well occurs a 0.18 and 0.12 years after the start of injection for an injection pressure of 6 MPa and temperatures

of 20°C [S7] and 50°C [S10], respectively. A profile of the carbon dioxide distribution is shown in Figure 3.12 [S10] at 6 months after the start of carbon dioxide injection by plotting the CO<sub>2</sub> fraction of formers, which is the sum of the CO<sub>2</sub> mass fraction of hydrate formers times saturation for the aqueous, gas, liquid CO<sub>2</sub>, and hydrate phases. This profile shows the principal migration path of the injected carbon dioxide is through gas zone to the production well.

At higher injection pressures [S8, S9, S11, and S12] the injected carbon dioxide forms secondary hydrate in the hydrate zone, forcing flow through the gas zone. At higher temperatures, secondary hydrate formation in the gas zone is reduced and the injected carbon dioxide flows principally as liquid CO<sub>2</sub>, as shown in Figure 3.13 [S12] at 0.15 years after the start of carbon dioxide injection. Because of the complex phase conditions, simulations involving higher pressure injections [S8, S9, S11, and S12] proceed with small time steps, leading to long execution times, as shown in Table 3.1. Simulation results after roughly 0.1 years for all high pressure scenarios, indicate secondary hydrate formation in both the hydrate and gas zones, resulting in low mobile phase permeabilities in the hydrate zone. These simulations [S8, S9, S11, and S12] were halted prior to completing 6-month injection period because of the negligible enhancement of methane production and slow execution progress.

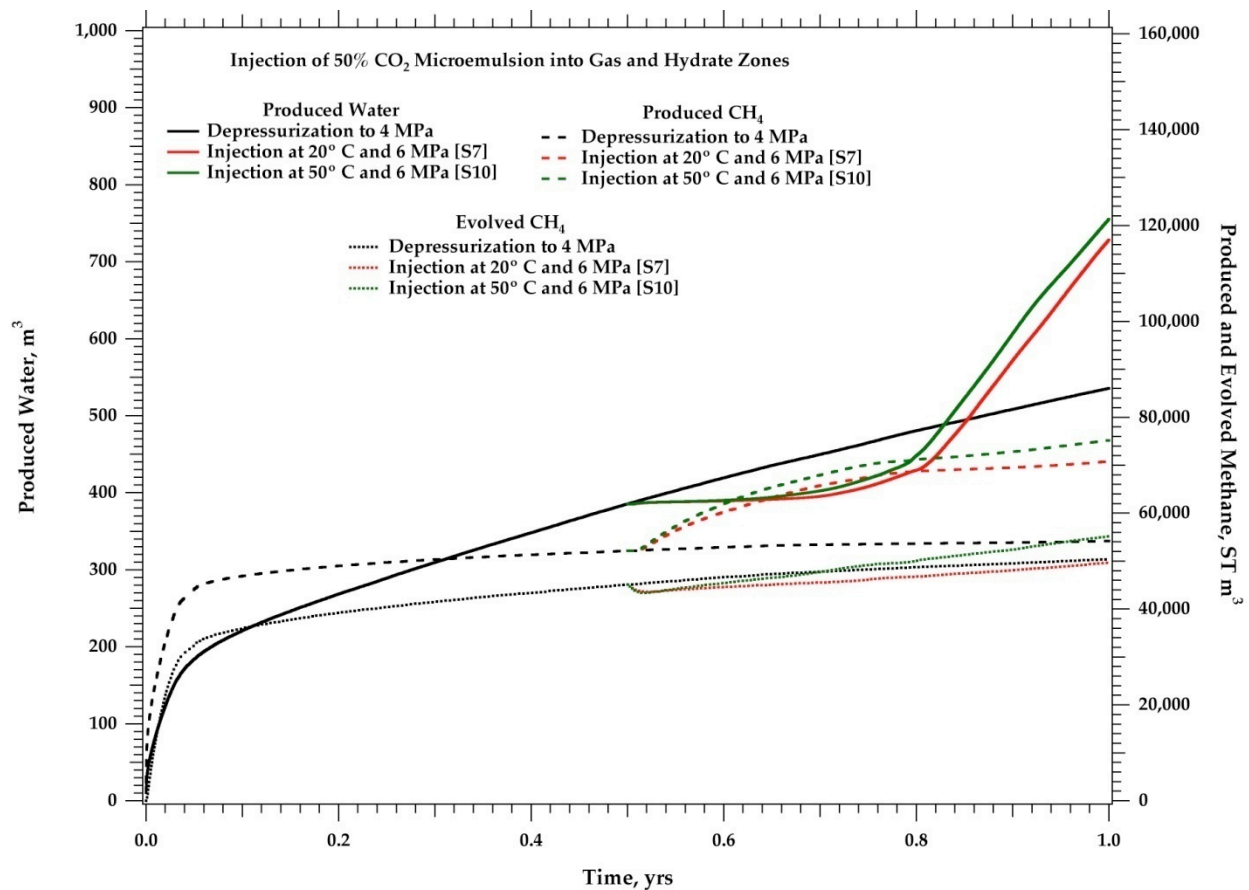


**Figure 3.9.** Produced water, produced methane, and evolved methane during 50% volumetric CO<sub>2</sub> micro-emulsion injection at 6 MPa across the hydrate and gas zones, producing at 4 MPa across the hydrate zone only after the 6-month depressurization stage at 4 MPa [S7 and S10].

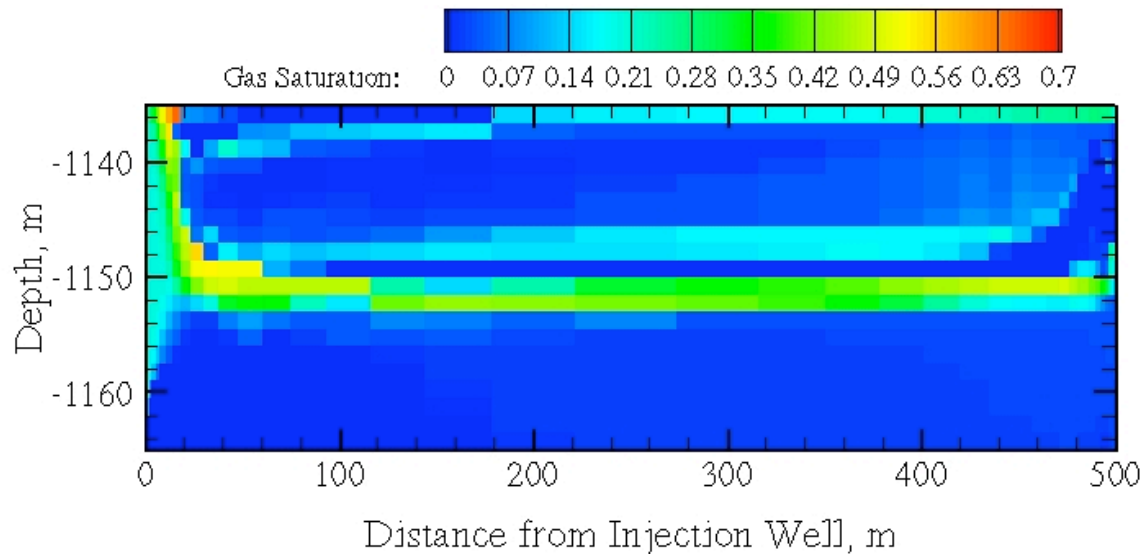


**Figure 3.10.** Gas saturation profile in the hydrate and gas zones after 50% volumetric CO<sub>2</sub> micro-emulsion injection at 6 MPa at 50° C for 6 months across the hydrate and gas zones, producing at 4 MPa across the hydrate zone only after the 6-month depressurization stage at 4 MPa [S10].

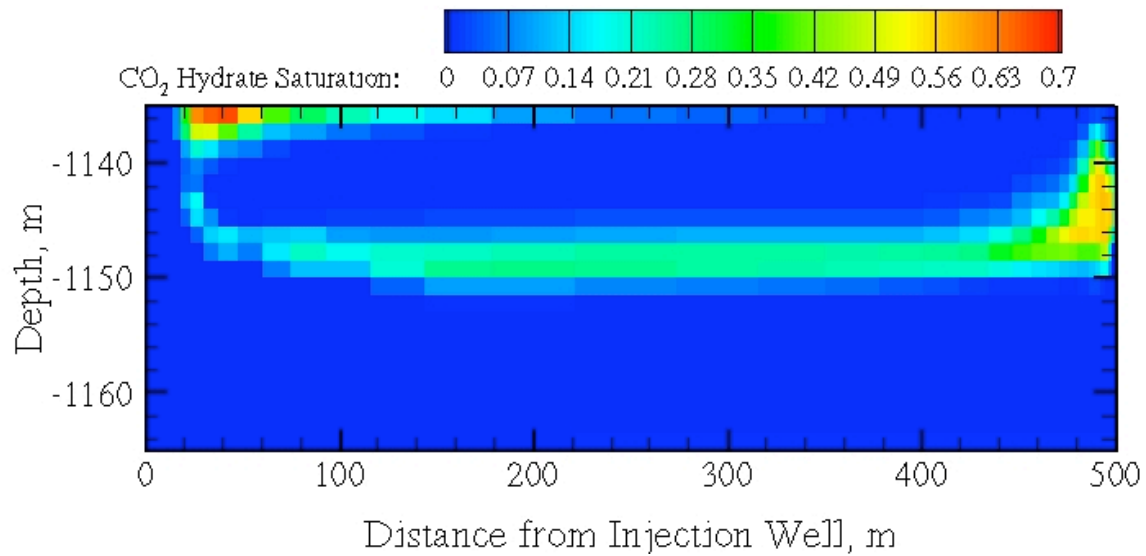


**Figure 3.11.** "CO<sub>2</sub> hydrate saturation" profile in the hydrate and gas zones after 50% volumetric CO<sub>2</sub> micro-emulsion injection at 6 MPa at 50° C for 6 months across the hydrate and gas zones, producing at 4 MPa across the hydrate zone only after the 6-month depressurization stage at 4 MPa [S10].

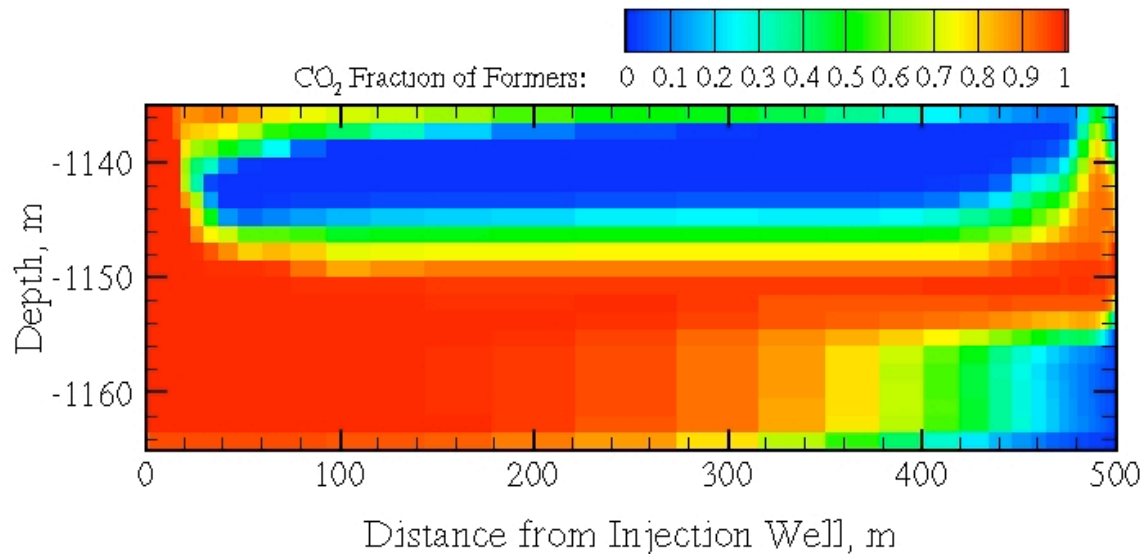


**Figure 3.12.** "CO<sub>2</sub> fraction of formers" profile in the hydrate and gas zones after 50% volumetric CO<sub>2</sub> micro-emulsion injection at 6 MPa at 50° C for 6 months across the hydrate and gas zones, producing at 4 MPa across the hydrate zone only after the 6-month depressurization stage at 4 MPa [S10].

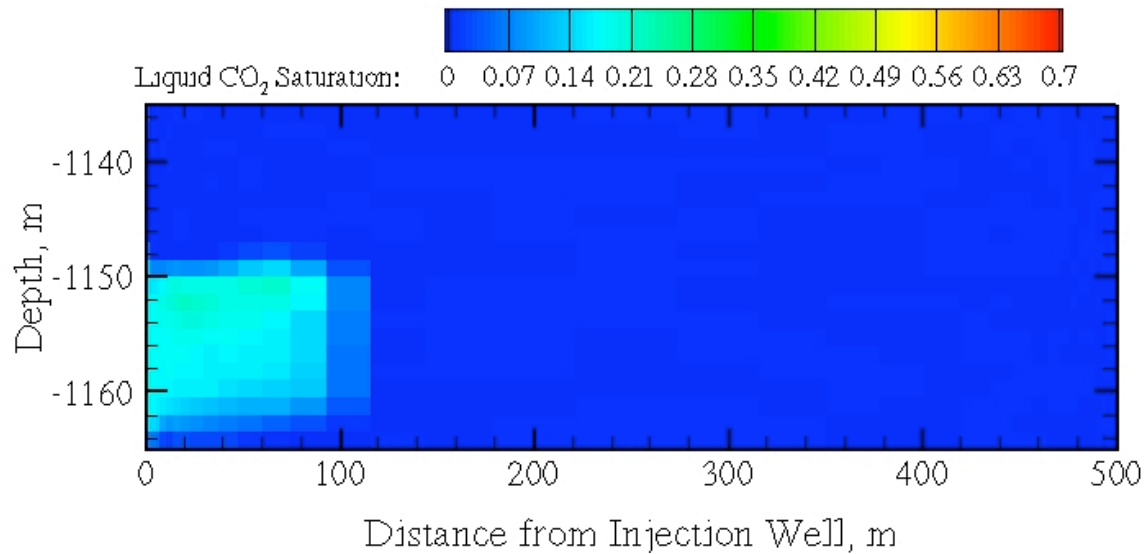


**Figure 3.13.** Liquid-CO<sub>2</sub> saturation profile in the hydrate and gas zones after 50% CO<sub>2</sub> volumetric micro-emulsion injection at 10 MPa at 50° C for 0.15 years across the hydrate and gas zones, producing at 4 MPa across the hydrate zone only after the 6-month depressurization stage at 4 MPa [S12].

### 3.2.1.3 Dissolved CO<sub>2</sub> Injection [S13 through S18]

The carbon dioxide density of dissolved CO<sub>2</sub> is roughly an order of magnitude lower than injecting pure CO<sub>2</sub>, as shown in Table 3.1. To increase the effective injection density of carbon dioxide, the concept for this injection strategy was to re-circulate the water carrier fluid, using the produced water. Injection of dissolved carbon dioxide has been suggested as a technology for geologically sequestering carbon dioxide in saline reservoirs to reduce the displacement of formation brines. This section discusses the series of six simulations [S13 through S18] that investigated the injection of dissolved carbon dioxide into the reservoir through well-casing screens across both the hydrate and gas zones. As shown in Table 3.1, the injectant density of dissolved carbon dioxide goes up with injection pressure and down with injection temperature.

Simulation results for produced water, produced methane, and evolved methane, with the injection of dissolved carbon dioxide at three pressures (i.e., 6 MPa, 8 MPa, and 10 MPa) and two temperatures (i.e., 20° C and 50° C) are shown in Figure 3.14 [S13, S14, S16, S17, and S18]. At the lower injection pressure of 6 MPa [S13, S16] injection of dissolved carbon dioxide rapidly yields an additional 10% of produced methane with a reduction in evolved methane, indicating some of the previously evolved methane reformed hydrate. The saturation profiles throughout the simulation indicate that the primary mechanism for the added methane production is one of displacing free gas methane to the production wells. At 6 MPa the injected water and dissolved carbon dioxide dissociate hydrate near the injection well within the hydrate zone. This creates a flow path that principally circumvents the hydrate zone as shown by the gas hydrate saturation profile in Figure 3.15 [S13]. Results from these simulations indicate that injecting carbon dioxide in dissolved form across the hydrate and gas zones does not meet the objectives of the exchange technology. This approach results in little assimilation of the injected carbon dioxide into hydrate and only a slight increase in produced methane. In addition injecting dissolved carbon dioxide at 10 MPa and 20° C yields high hydrate saturation in the hydrate zone around the well, choking off flow through the hydrate zone.

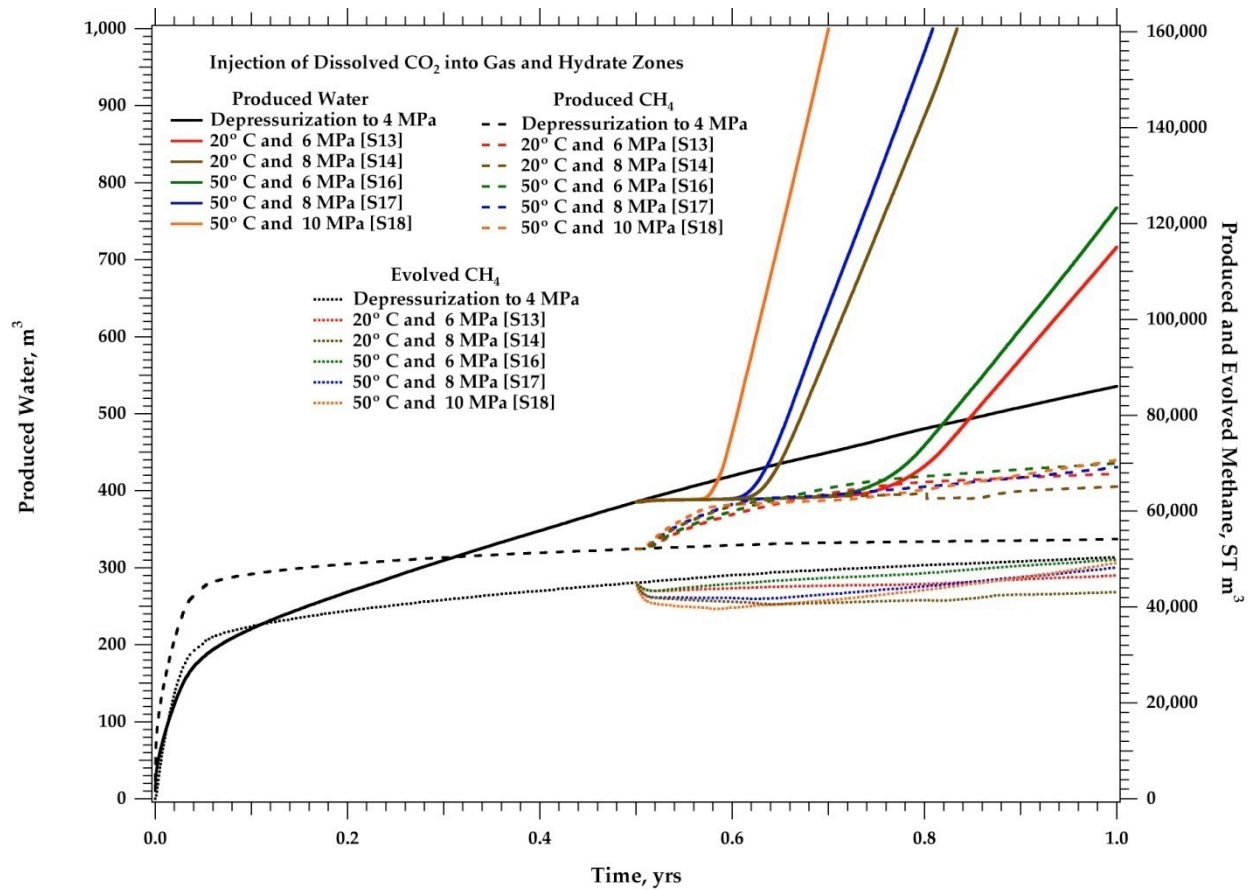


**Figure 3.14.** Produced water, produced methane, and evolved methane during dissolved CO<sub>2</sub> injection at 6, 8, and 10 MPa across the hydrate and gas zones, producing at 4 MPa across the hydrate zone only after the 6-month depressurization stage at 4 MPa [S13, S14, S16, S17, and S18].

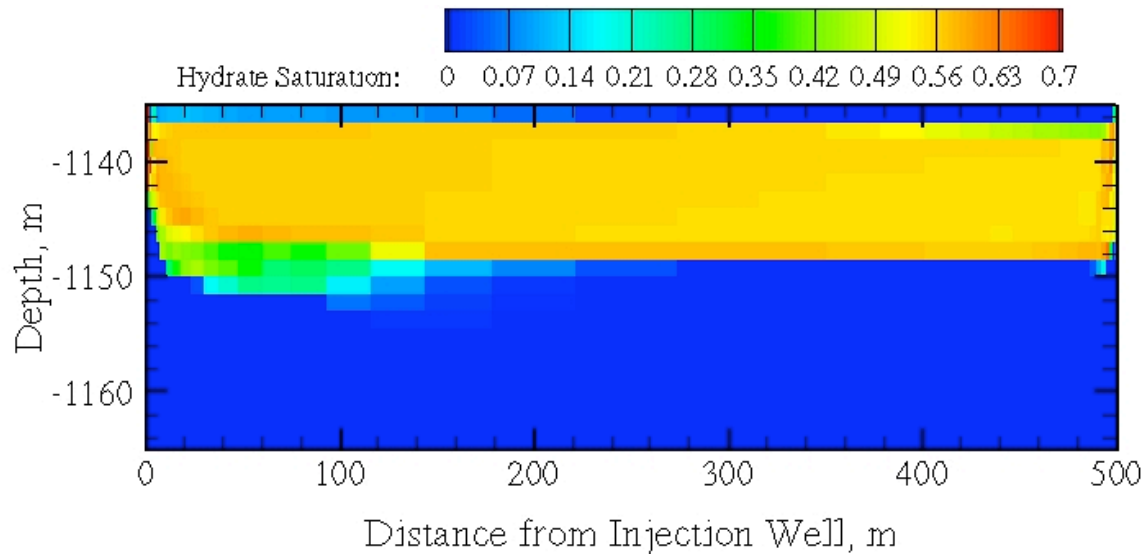


**Figure 3.15.** Hydrate saturation profile in the hydrate and gas zones after dissolved CO<sub>2</sub> injection at 6 MPa at 20° C for 6 months across the hydrate and gas zones, producing at 4 MPa across the hydrate zone only after the 6-month depressurization stage at 4 MPa [S13]

### 3.2.2 Hydrate-Zone Only Injection Scenarios [S19 through S36]

The combined hydrate- and gas-zone injection scenarios yielded moderate increases in the production of methane, but not from the exchange of carbon dioxide with methane as the hydrate guest molecule. The increased production was due to the flushing of methane gas toward the production well in the gas zone, as the residual hydrate in the hydrate zone was largely bypassed. To promote flow through the hydrate zone and increase the contact of carbon dioxide with methane hydrate, a series of simulations [S19 through S36] were executed that investigated injecting carbon dioxide through well-casing screens located in the hydrate zone only and producing through screened intervals in the hydrate zone only. This section describes the simulation results for the hydrate-zone only injection scenarios, where the objective for injecting only into the hydrate zone was to increase carbon dioxide exchange, increased methane evolution, and increased methane production compared with the scenarios for combined hydrate- and gas-zone injection.

#### 3.2.2.1 Pure CO<sub>2</sub> Injection [S19 through S24]

Injecting pure CO<sub>2</sub> into the hydrate zone yielded nearly identical amounts of produced and evolved methane at an injection pressure of 6 MPa [S19 and S22], as seen by comparing the plots of these quantities in Figures 3.5 and 3.16. Breakthrough times were also nearly identical between the two injection configurations, as shown in Table 3.1. The differences in produced water between the hydrate-zone only [S19 and S22] and combined hydrate- and gas-zone [S1 and S4] injection scenarios at 6 MPa are due to the reduced hydrate saturation levels around the injection well and increased hydrate saturation levels around the production well for the hydrate-zone only simulations [S19 and S22]. As with the combined hydrate- and gas-zone scenarios at higher pressures [S2, S3, S5, and S6], the hydrate-zone only injections at higher pressures [S20, S21, S23, and S24] suffered from poor execution performance (see Table 3.1) and were halted before completing the 6-month injection period.

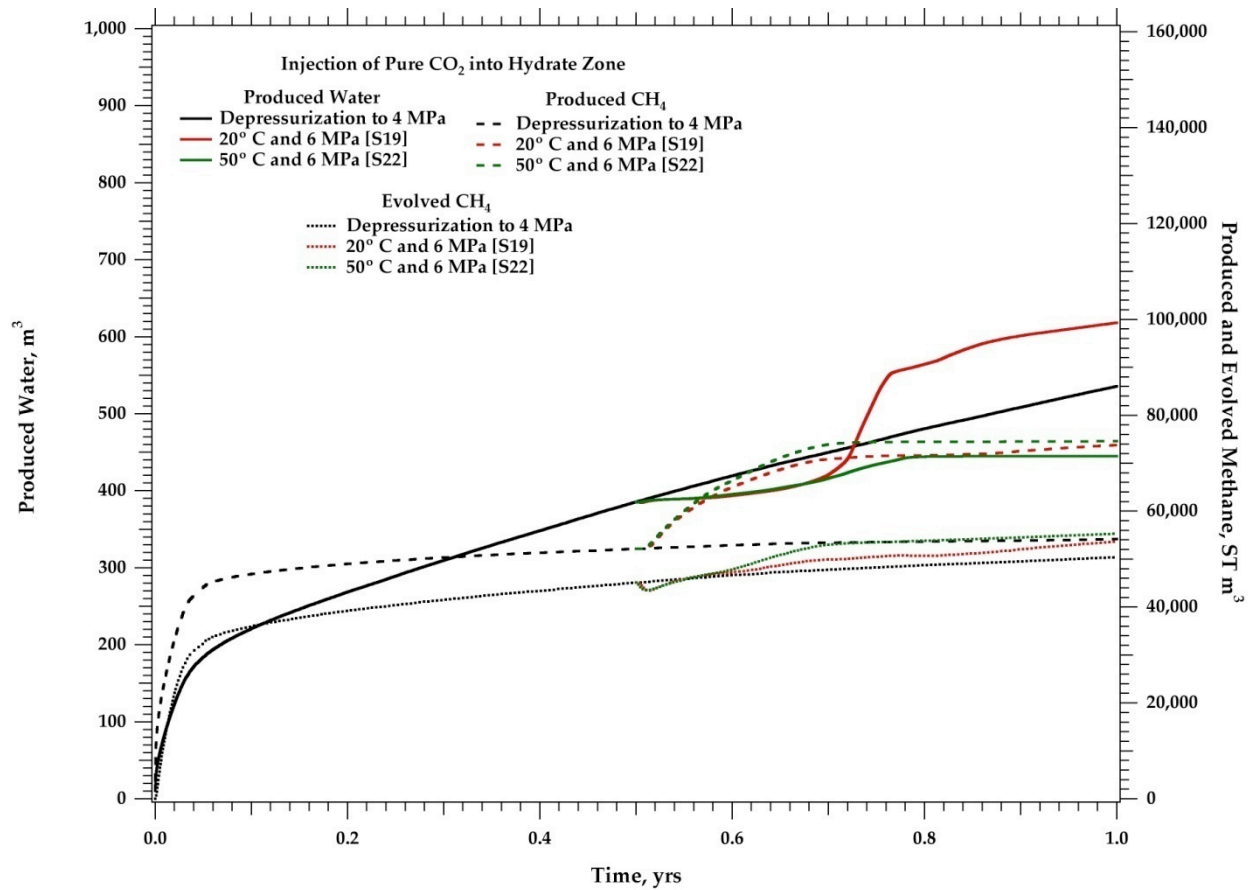


**Figure 3.16.** Produced water, produced methane, and evolved methane during pure CO<sub>2</sub> injection at 6 MPa across the hydrate zone only, producing at 4 MPa across the hydrate zone only, initiated from the 6-month depressurization stage at 4 MPa [S19 and S22].

### 3.2.2.2 50% Volumetric CO<sub>2</sub> Micro-emulsion Injection [S25 through S30]

Injecting carbon dioxide as a 50% volumetric micro-emulsion over the hydrate zone only [S25 through S30] did not significantly alter the contact of the injected fluid with the residual hydrate, nor alter the produced methane, compared with injecting over the combined hydrate and gas zones [S7 through S12]. Both injection scenarios yielded the formation of secondary hydrate along the top of the hydrate zone and along the interface between the gas and hydrate zones. This secondary hydrate principally comprised carbon dioxide. We anticipated that injecting the micro-emulsion at 50° C at 6 MPa [S28] would produce flow across the hydrate zone, encouraging the exchange of carbon dioxide and methane as guest molecules. Instead, the simulations indicate an initiation of a cross flow pattern, and the formation of secondary carbon dioxide hydrate at the gas hydrate perimeters. This impermeable carbon dioxide hydrate layer forces the flow through the gas zone, as shown in Figure 3.17 [S28].

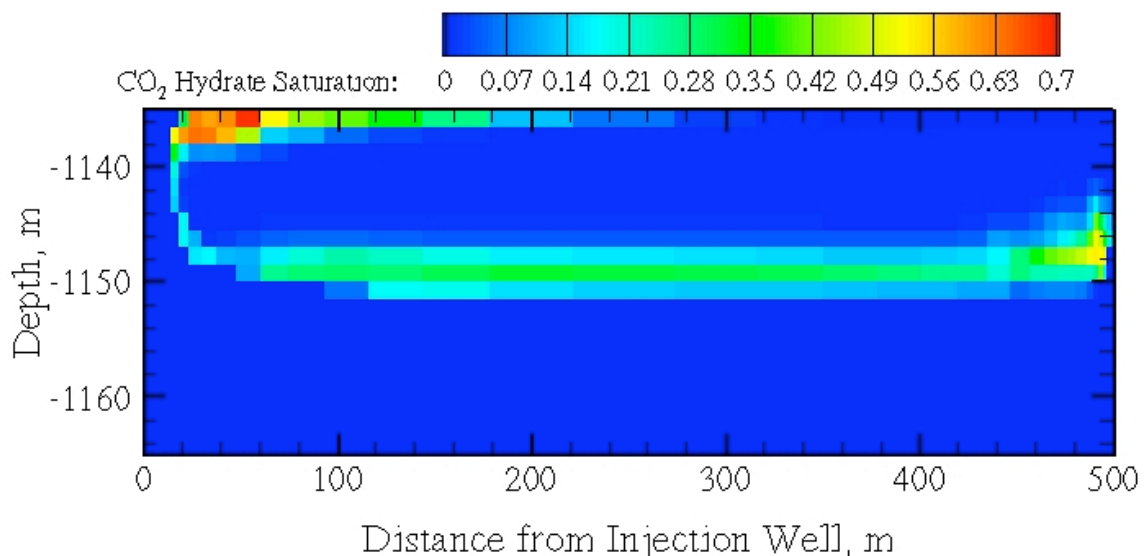


**Figure 3.17.** "CO<sub>2</sub> hydrate saturation" profile in the hydrate and gas zones after 50% volumetric CO<sub>2</sub> micro-emulsion at 6 MPa at 50° C for 6 months across the hydrate zone only, producing at 4 MPa across the hydrate zone only after the 6-month depressurization stage at 4 MPa [S28].

### 3.2.2.3 Dissolved CO<sub>2</sub> Injection [S31 through S36]

Injecting dissolved CO<sub>2</sub> over the hydrate zone only [S31 through S36] yielded similar results in terms of produced and evolved methane to those for injections over the combined hydrate and gas zones [S13 through S18], as shown by comparing Figures 3.14 and 3.18. The injected dissolved CO<sub>2</sub> dissociates hydrate near the injection well forming a flow channel to the lower effective permeability gas zone. The resulting flow pattern is such that the hydrate zone is largely bypassed, allowing the exchange of carbon dioxide and methane guest molecules to occur only along the interface between the gas and hydrate zones.

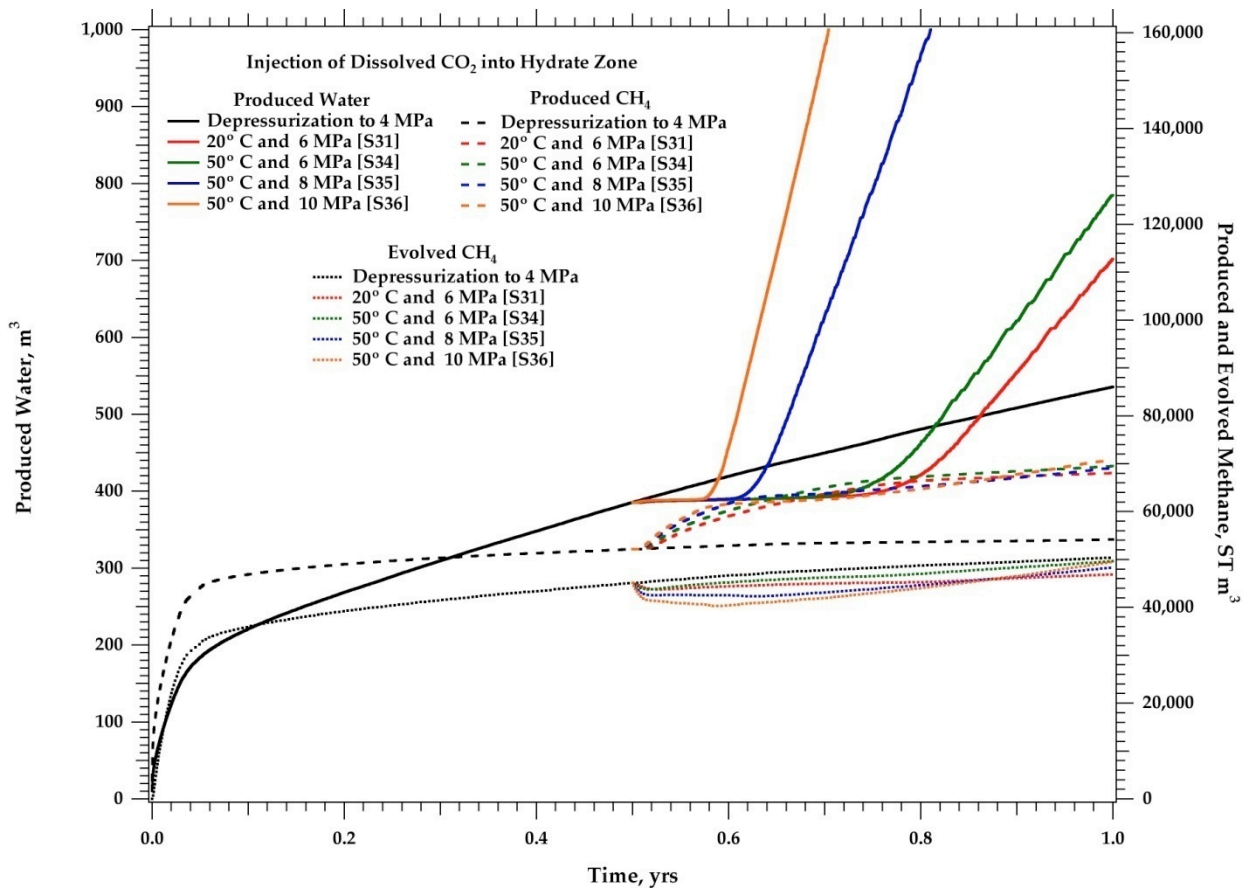


**Figure 3.18.** Produced water, produced methane, and evolved methane during dissolved CO<sub>2</sub> injection at 6, 8, and 10 MPa across the hydrate zone only, producing at 4 MPa across the hydrate zone only after the 6-month depressurization stage at 4 MPa [S31, S34, S35, and S36].

## 4.0 Class 3 Gas Hydrate Accumulations

Class 3 gas hydrate accumulations are characterized by a single permeable hydrate-bearing interval bounded above and below by impermeable intervals. Using numerical simulation Moridis demonstrated (Moridis, 2004) that thermal stimulation was more effective than depressurization for Class 3 gas hydrate accumulations because of the adverse permeability conditions that occur with high hydrate saturations. Simulations executed by Moridis considered an idealized two-dimensional Cartesian domain that represented a 10-m thick fractured hydrate zone with wells spaced 30 m apart. The underlying zones of high permeability, characteristic of the Class 1 and 2 gas hydrate accumulations, provided bypass mechanisms for injected CO<sub>2</sub>, as described in Section 3, above. The CO<sub>2</sub> injection simulations in this section were designed to investigate the feasibility using a straightforward injection and withdrawal production approach to applying both direct and indirect (e.g., EGHR) guest molecule exchange technologies to Class 3 gas hydrate accumulations. Whereas the simulations conducted in this study for Class 1 gas hydrates used the parameter descriptions developed by Moridis and Sloan (2007), the simulations for Class 3 gas hydrate accumulations described in this section differed from those used by Moridis (2004) for Class 3 gas hydrates accumulations. For ease of comparison between simulation results for these investigations, the formation structure and parameters used in the Class 3 gas hydrate accumulation simulations were those used for Class 1 (Section 3), but without the underlying hydrate-free permeable zone.

### 4.1 Simulation Scenarios

In keeping with the Class 1 simulations, the top of the hydrate-bearing layer was set at 1135m, but the thickness of the permeable layer was altered from a two-zone 30-m formation with a 15-m hydrate zone and 15-m gas zone, to a single 15-m hydrate zone formation. Although not generally typical of Class 3 gas hydrate accumulations, the boundary between the hydrate zone and the underlying impermeable interval was defined by hydrate stability for pure methane hydrate. Because of the underlying gas zone in the Class 1 simulations, an initialization simulation was required to establish equilibrium conditions between the gas and hydrate zones. To replicate field observations of Class 1 gas hydrate accumulations, having an aqueous-hydrate zone overlying an aqueous-gas zone, a gas hydrate saturation dependent entry pressure model was implemented, following Moridis et al. (2007). Whereas this function would not be strictly required to create stable initial conditions for the Class 3 simulations, this function was used to allow for a more direct comparison of simulation results. It should be noted that the function necessitates higher gas pressures to create a mobile gas phase. For the Class 3 simulations initial conditions were established without an initialization simulation, by specifying the initial temperature gradient, aqueous pressure gradient and hydrate saturation. As with the Class 1 simulations, the initial hydrate saturation of 0.7 yielded excessively low effective permeabilities, which necessitated first depressurizing the formation to produce hydrate through partial dissociation and to increase the effective permeability. For comparison purposes, the depressurization stage was limited to 0.5 years. The final stage, the production stage, followed the approach taken for the Class 1 simulations (Section 3); where, a suite of CO<sub>2</sub> injection scenarios were investigated. Table 4.1 shows the matrix of simulation scenarios for the carbon dioxide injection stage.

**Table 4.1.** Class 3 Gas Hydrate Accumulation Simulation Scenarios

<b>Injectant</b>	<b>CO<sub>2</sub> State</b>	<b>Injection Press, MPa</b>	<b>Injection Temp., C</b>	<b>Injectant Density, kg/m<sup>3</sup></b>	<b>Simulation ID</b>
Pure CO <sub>2</sub>	Liquid	6	20	778.8	R1
	Liquid	8	20	829.0	R2
	Liquid	10	20	856.4	R3
	Gas	6	50	135.0	R4
	Supercritical	8	50	217.3	R5
	Supercritical	10	50	383.3	R6
50% Micro-emulsion	Liquid	6	20	389.4	R7
	Liquid	8	20	414.5	R8
	Liquid	10	20	428.2	R9
	Gas	6	50	67.5	R10
	Supercritical	8	50	108.7	R11
	Supercritical	10	50	191.7	R12
Aqueous Dissolved CO <sub>2</sub>	Dissolved	6	20	66.1	R13
	Dissolved	8	20	69.5	R14
	Dissolved	10	20	72.6	R15
	Dissolved	6	50	37.0	R16
	Dissolved	8	50	44.8	R17
	Dissolved	10	50	50.2	R18

## 4.2 Simulation Results

The production protocol involved a 0.5-year depressurization stage followed by a 0.5-year injection stage. As with the Class 1 simulations, during the depressurization stage both ends of the domain were depressurized, producing methane gas. As a standard, a depressurization simulation was executed that involved depressurizing the formation for 1.0 year from both ends of the reservoir. A plot of the produced methane and water (i.e., extracted from the reservoir) and evolved methane (i.e., released from the hydrate) is shown in Figure 4.1 for this simulation. Initially the reservoir contains 136,000 ST m<sup>3</sup> of methane in gas hydrate, free gas, and dissolved form. This is 15% less than the total methane in the class 1 simulations. During the first six months of depressurization, approximately 10% of the initial methane is produced from the reservoir and 11% is evolved. The lack of an underlying permeable zone yielded about one third less than the production rates for the Class 1 hydrates.

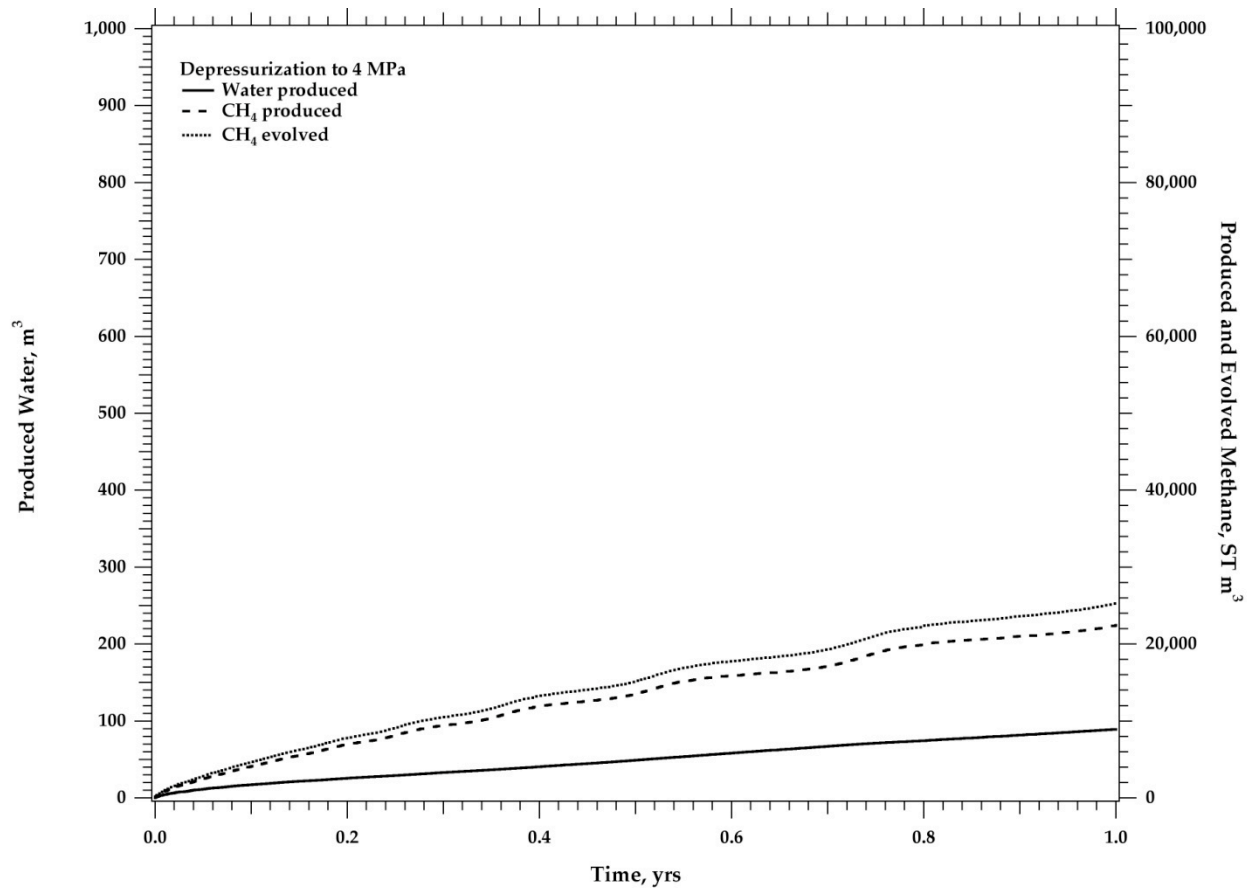


**Figure 4.1.** Produced water, produced methane, and evolved methane following depressurization at 4 MPa for 1 year across the hydrate zone [R0].

The gas saturation and hydrate saturation profiles after the depressurization period of 0.5 years are shown in Figures 4.2 and 4.3, respectively. These plots reinforce the results of Moridis (2004) for Class 3 hydrates, where production was hampered by low effective permeability of the hydrate zone. The effect of the depressurization only extends approximately 100 m from the well. Hydrate saturations are reduced to zero within this radius and near the top of the hydrate zone where heat transfer from the upper impermeable shale interval is rapid. Lower in the hydrate zone, and within the 100 m radius, hydrate saturations are reduced from the initial value of 0.7 to 0.5 through dissociation. This dissociation pattern unfortunately leaves the bulk of the hydrate zone unchanged from the initial condition (i.e., low effective permeability).

Injection of carbon dioxide was started from the depressurization conditions at 0.5 years, similar to the Class 1 simulations. Carbon dioxide in one of three forms (i.e., pure CO<sub>2</sub>, 50% volumetric CO<sub>2</sub> micro-emulsion, or dissolved CO<sub>2</sub>) was injected along the left-hand boundary, with the right-hand boundary being maintained at 4 MPa. The injection simulations were halted when one of two conditions was realized: 1) total simulation time reached 1 year or 2) secondary hydrate development clogged the injection.

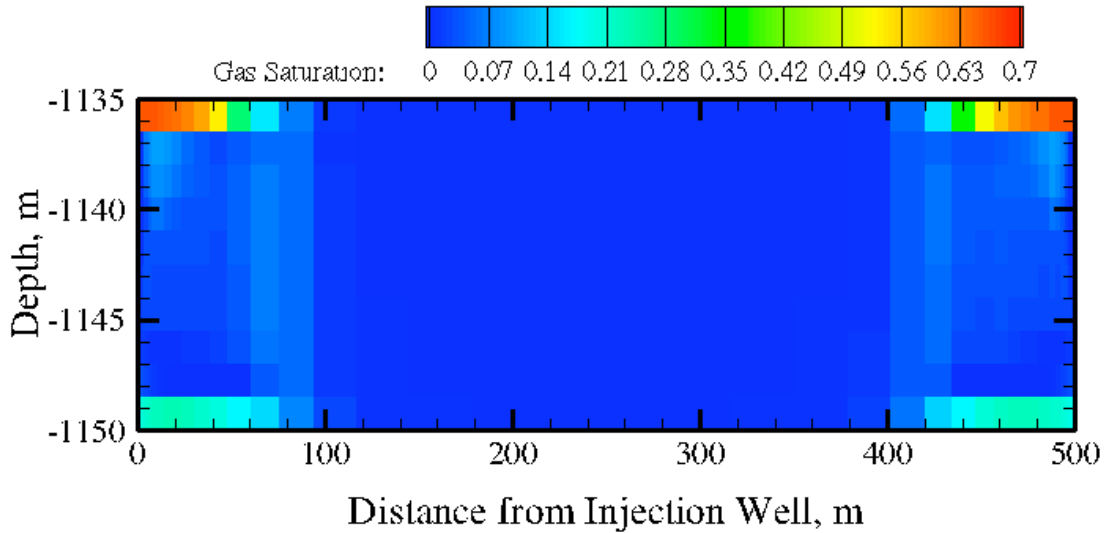


**Figure 4.2.** Gas saturation after depressurization at 4 MPa for 6 months across hydrate zone [R0].

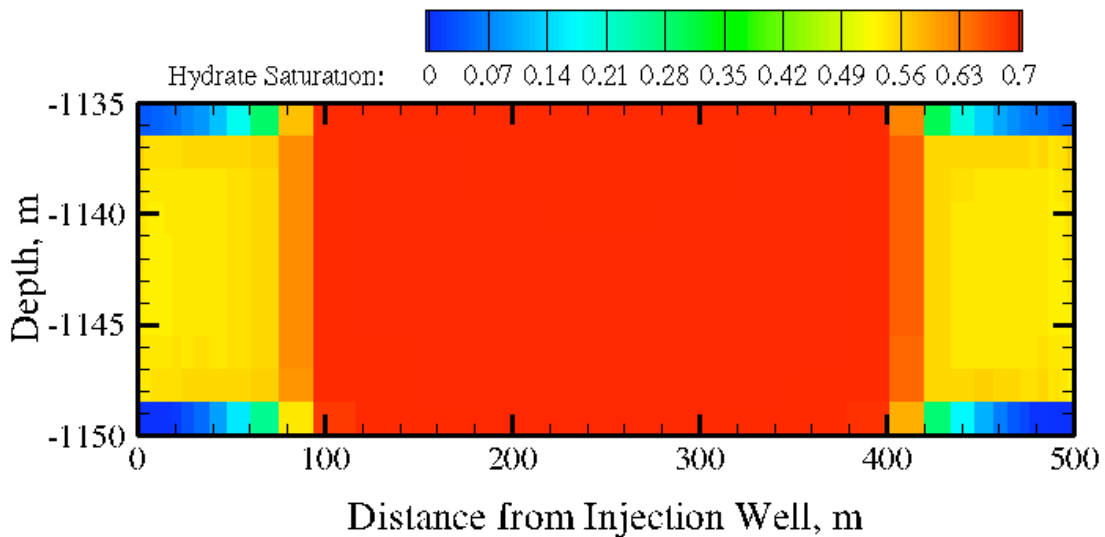


**Figure 4.3.** Hydrate saturation after depressurization at 4 MPa for 6 months at both ends across hydrate zone [R0].

#### 4.2.1 Pure CO<sub>2</sub> Injection [R1 through R6]

A series of six simulations [R1 through R6] were executed that investigated the injection of pure carbon dioxide directly into the reservoir through well-casing screens. For the range of conditions at the injection point (i.e., pressures of 6 MPa, 8 MPa, and 10 MPa; and temperatures of 20°C and 50°C), the thermodynamic state of the carbon dioxide varied from being liquid CO<sub>2</sub>, to subcritical gas, to supercritical gas, as shown in Table 4.1. Simulation results for the produced water, produced methane, and evolved methane for the injection of pure CO<sub>2</sub> at 20°C indicate nearly identical results for the 6 MPa [R1] and 10 MPa [R3] cases for the first 0.5 years of injecting, as shown in Figure 4.4.

The injection of pure CO<sub>2</sub> shows a decrease in production from continued depressurization; where, the decrease is due to the combined effects of switching to a single production well and the formation of secondary hydrate. Figure 4.5 shows the CO<sub>2</sub> fraction of formers (i.e., total amount of CO<sub>2</sub> divided by the total amount of CH<sub>4</sub> and CO<sub>2</sub>) after injecting pure CO<sub>2</sub> at 10 MPa for 6 months after a 6-month depressurization period [R3]. This plot indicates that even with a 6 MPa differential across the injection and production wells, the injected CO<sub>2</sub> does not penetrate the hydrate zone beyond where hydrate dissociation occurred during the depressurization stage. Figure 4.6, showing the hydrate saturation at the end of simulation R3, indicates reformation of nearly pure CH<sub>4</sub> hydrate in the upper portions of the formation and mixed CH<sub>4</sub>-CO<sub>2</sub> hydrate in the lower portion of the formation on the injection side. On the production side, hydrate dissociation and methane production continue along the upper and lower boundaries where heat from impermeable zones provides the required dissociation energy.

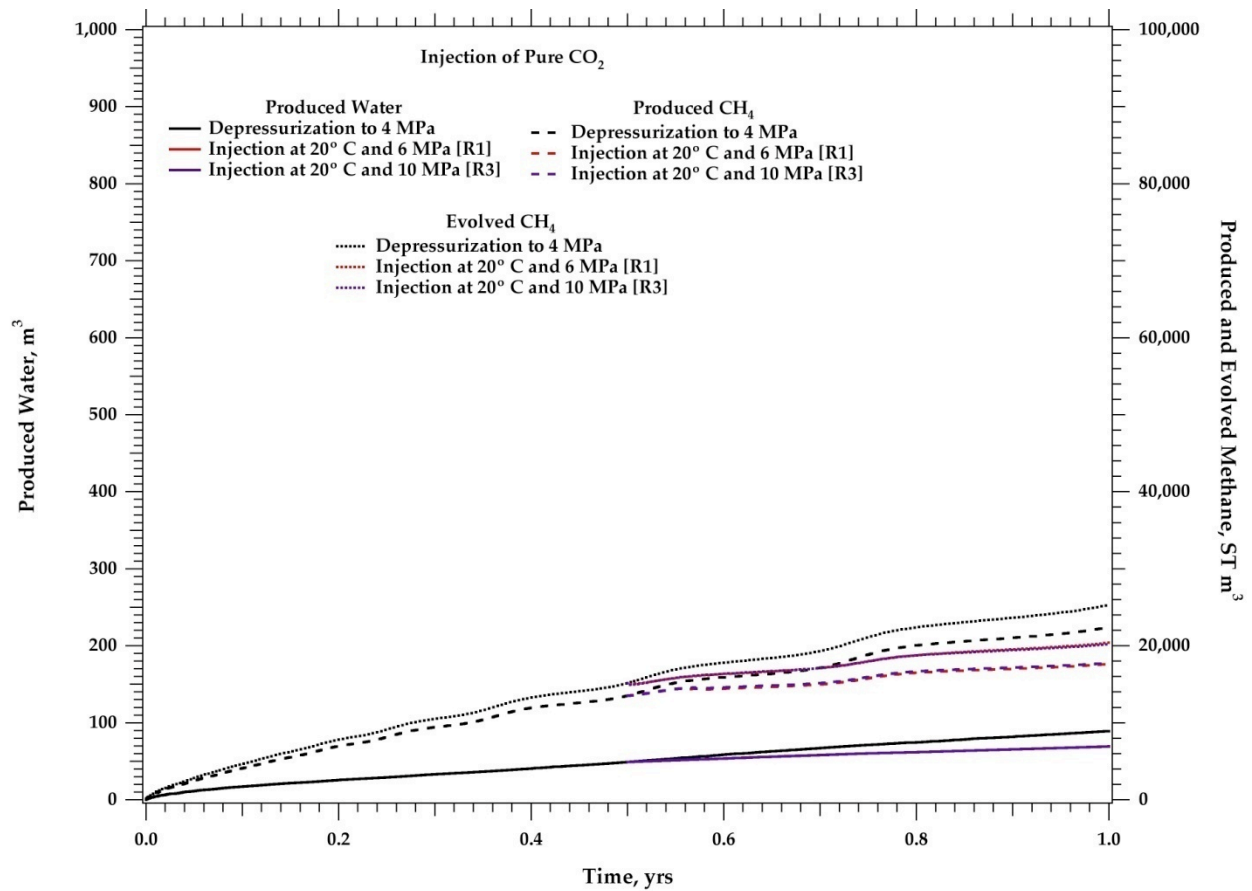


**Figure 4.4.** Produced water, produced methane, and evolved methane during pure CO<sub>2</sub> injection at 20° C, 6 MPa and 10 MPa, producing at 4 MPa, initiated from the 6-month depressurization stage at 4 MPa [R1 and R3].

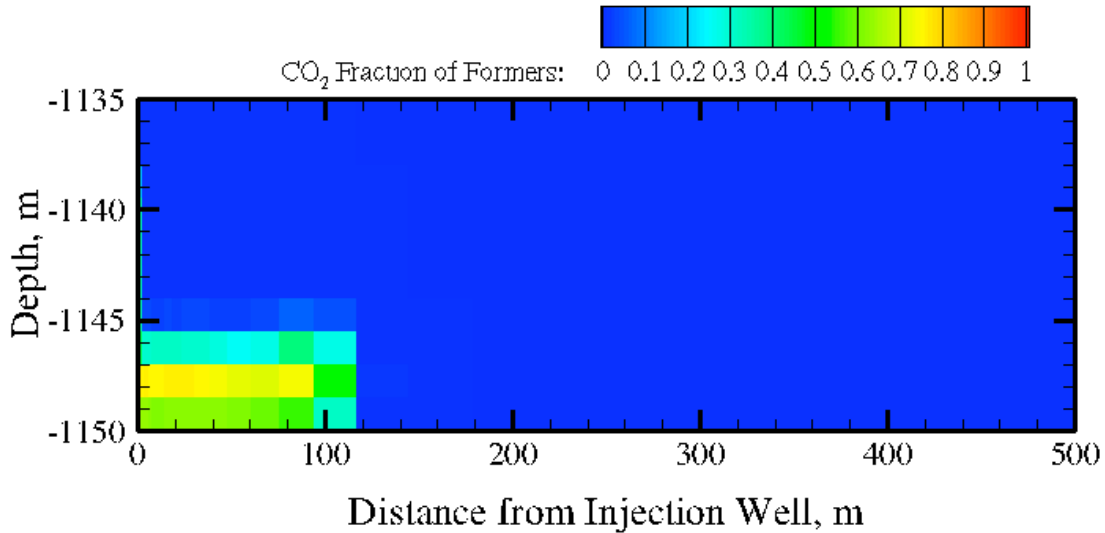


**Figure 4.5.** "CO<sub>2</sub> fraction of formers" profile after injection of pure CO<sub>2</sub> at 10 MPa at 20° C for 6 months, producing at 4 MPa, initiated from the 6-month depressurization stage [R3].

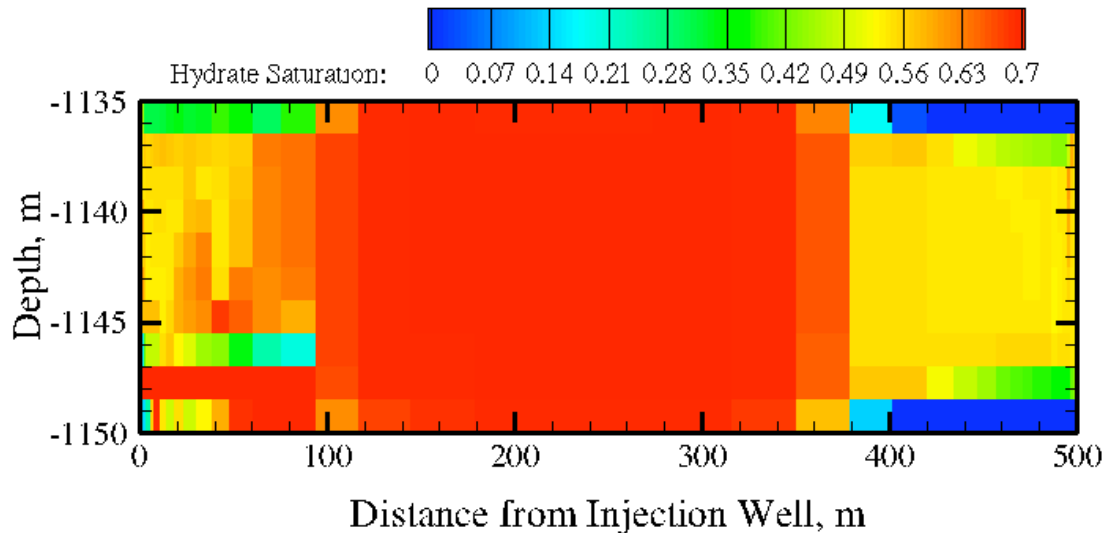


**Figure 4.6.** "Hydrate saturation" profile after injection of pure CO<sub>2</sub> at 10 MPa at 20° C for 6 months, producing at 4 MPa, initiated from the 6-month depressurization stage [R3].

#### 4.2.2 50% Volumetric CO<sub>2</sub> Micro-emulsion Injection [R7 through R12]

This section discusses the series of six simulations [R7 through R12] that investigated the injection of carbon dioxide as a 50% volumetric micro-emulsion into the reservoir through well-casing screens, similar to the Class 1 simulations. Simulation results for produced water, produced methane, and evolved methane with the injection of a 50% volumetric carbon dioxide micro-emulsion indicate the additional sensible heat provided with the injected water is not sufficient to increase production over the depressurization reference cases, even using a 50°C injectant, as shown in Figure 4.7 [R7-R11]. The lowest injection pressure and highest temperature combination [R10] yields

increased amounts of CO<sub>2</sub> in the formation, but no differences in the hydrate composition beyond 100 m from the injection side, as shown by the distributions of CO<sub>2</sub> hydrate saturation (i.e., the fraction of formers in the hydrate phase times the hydrate saturation) and hydrate saturation in Figures 4.8 and 4.9, respectively.

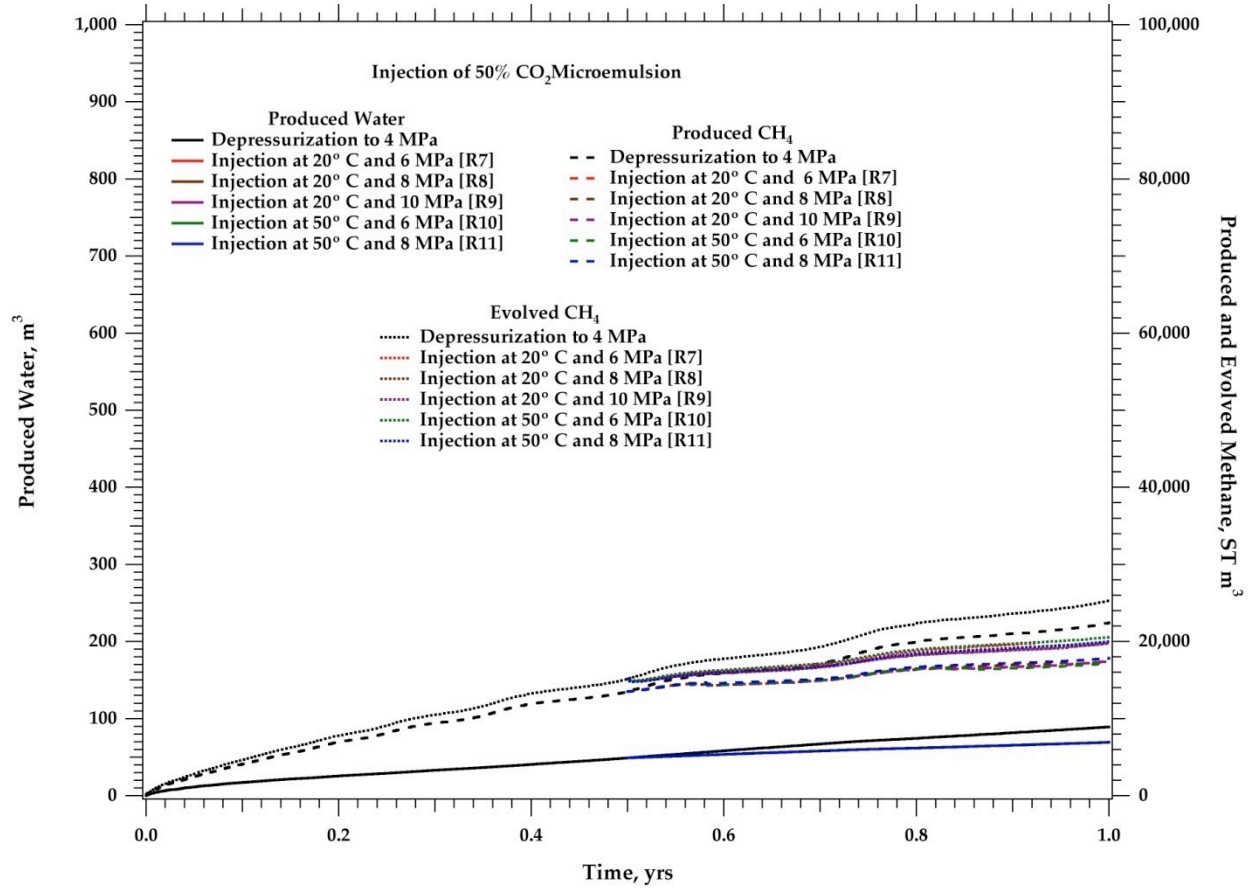


**Figure 4.7.** Produced water, produced methane, and evolved methane during 50% volumetric CO<sub>2</sub> micro-emulsion at 20° C, 6 MPa, 8 MPa, and 10 MPa, producing at 4 MPa, initiated from the 6-month depressurization stage at 4 MPa [R7 – R11].

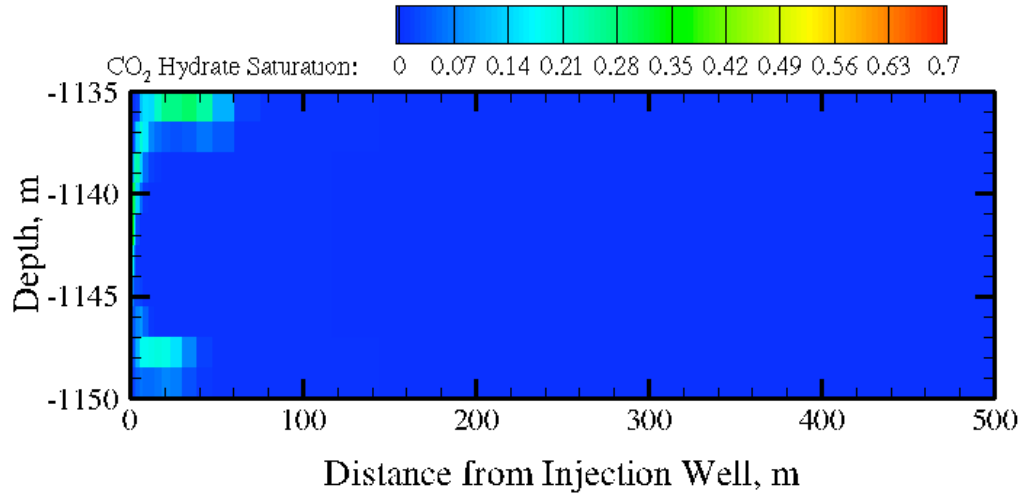


**Figure 4.8.** "CO<sub>2</sub> hydrate saturation" profile after injection of 50% volumetric CO<sub>2</sub> micro-emulsion at 6 MPa at 50° C for 6 months, producing at 4 MPa, initiated from the 6-month depressurization stage [R10].

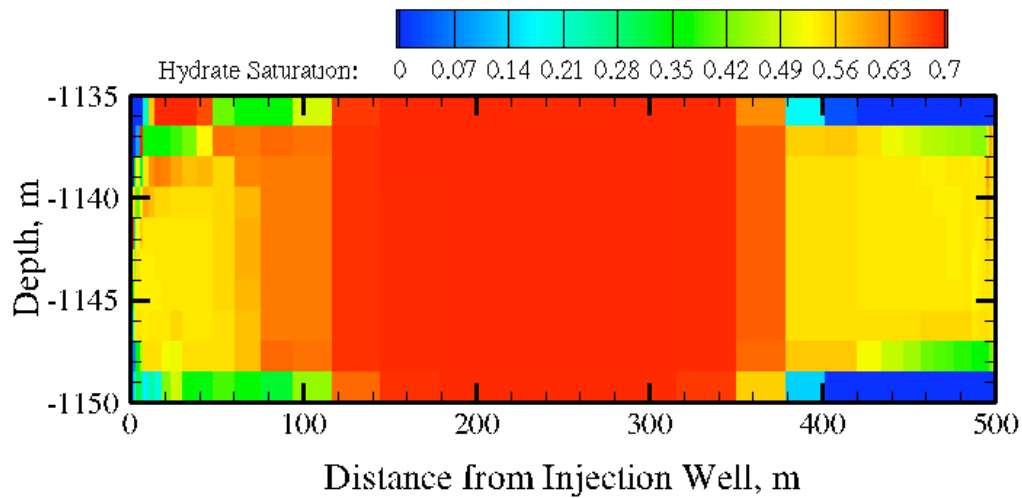


**Figure 4.9.** "Hydrate saturation" profile after injection of 50% volumetric CO<sub>2</sub> micro-emulsion at 6 MPa at 50° C for 6 months, producing at 4 MPa, initiated from the 6-month depressurization stage [R10].

#### 4.2.3 Dissolved CO<sub>2</sub> Injection [R13 through R18]

This section discusses the series of six simulations [R13 through R18] that investigated the injection of dissolved carbon dioxide into the reservoir through well-casing screens. As shown in Table 4.1, the injectant density of dissolved carbon dioxide goes up with injection pressure and down with injection temperature. Simulation results for produced water, produced methane, and evolved methane, with the injection of dissolved carbon dioxide at three pressures (i.e., 6 MPa, 8 MPa, and 10 MPa) and two temperatures (i.e., 20° C and 50° C) are shown in Figure 4.10 [R13 through R18]. The progression from pure CO<sub>2</sub> to CO<sub>2</sub> micro-emulsion to dissolved CO<sub>2</sub> injectant, translates to in-

jecting increased amounts of water per volume of injectant. At the highest temperatures and injection pressures the system is functioning more as a thermal stimulation scheme than a CO<sub>2</sub> injection scheme. Nevertheless the impact on produced methane over the short term (i.e., initial 6 months) is not minimal, as indicated by Figure 4.10. The injectant does yield increases in gas saturation near the injection well, principally through release of CH<sub>4</sub> from the dissociation of hydrate via thermal stimulation, as shown in Figure 4.11. However, the actual amount of injected CO<sub>2</sub> being incorporated into hydrate is small, as indicated by the distribution of CO<sub>2</sub> hydrate saturation (i.e., the fraction of formers in the hydrate phase times the hydrate saturation) shown in Figure 4.12.

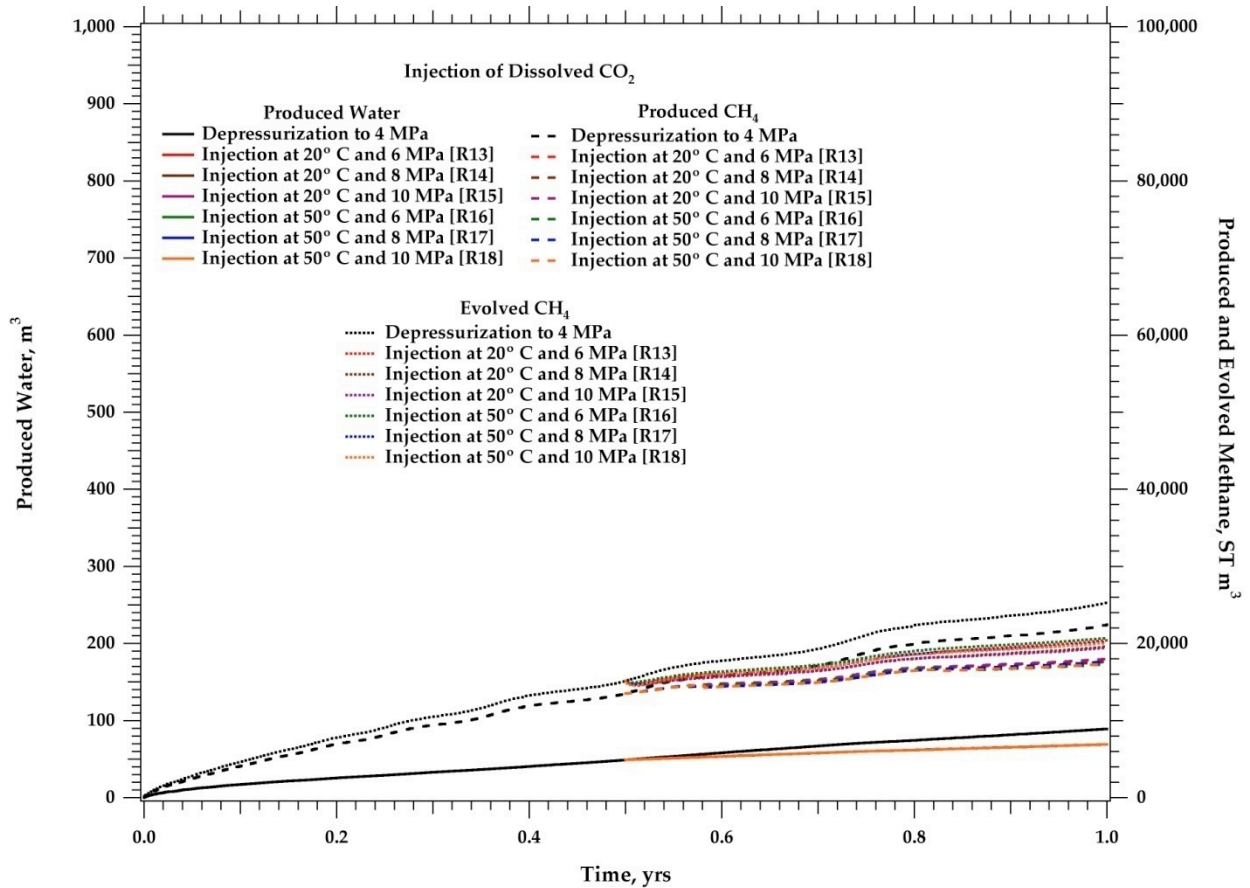


**Figure 4.10.** Produced water, produced methane, and evolved methane during dissolved CO<sub>2</sub> injection at 20° and 50° C, 6 MPa, 8 MPa, and 10 MPa, producing at 4 MPa, initiated from the 6-month depressurization stage at 4 MPa [R13 – R18].

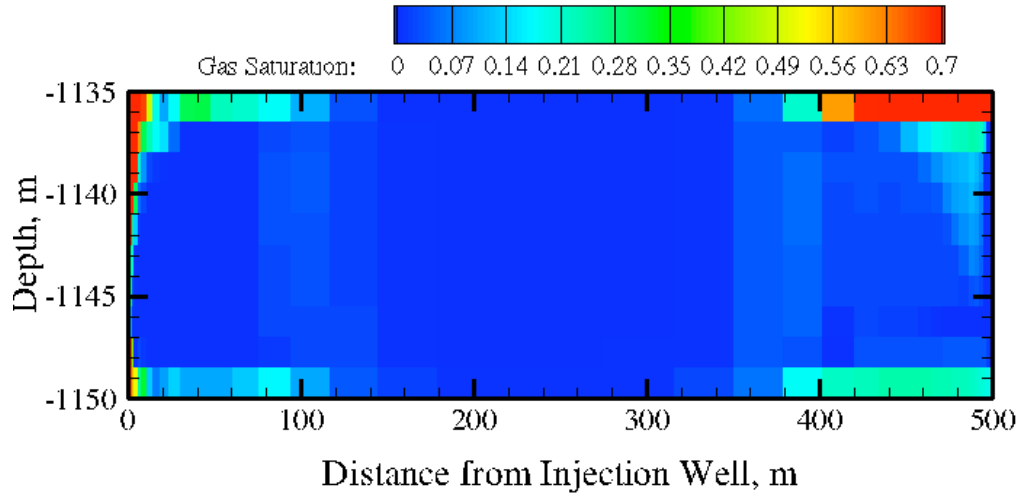


**Figure 4.11.** Gas saturation profile after injection of dissolved- $\text{CO}_2$  at 6 MPa at  $50^\circ\text{C}$  for 6 months, producing at 4 MPa, initiated from the 6-month depressurization stage [R16].

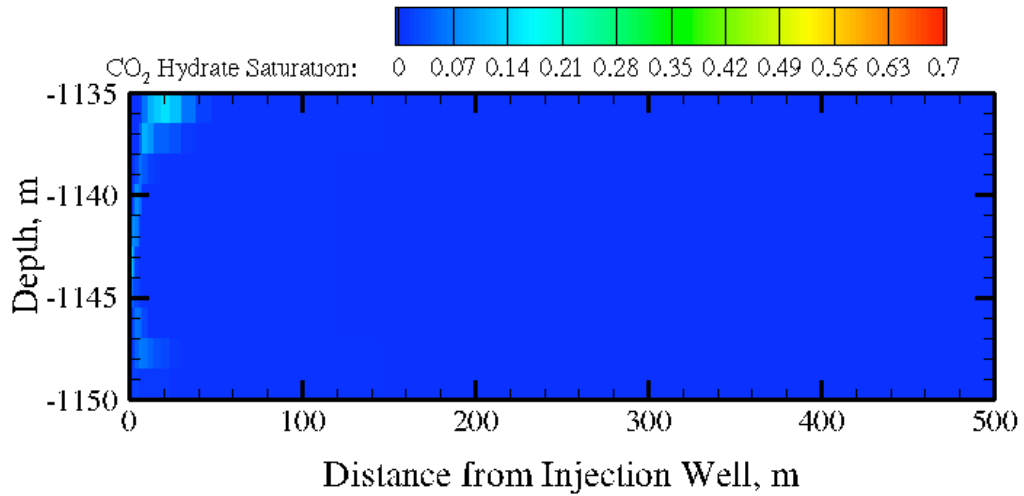


**Figure 4.12.** " $\text{CO}_2$  hydrate saturation" profile after injection of dissolved- $\text{CO}_2$  at 6 MPa at  $50^\circ\text{C}$  for 6 months, producing at 4 MPa, initiated from the 6-month depressurization stage [R16].

## 5.0 Class 4 Gas Hydrate Accumulations

Class 4 hydrate accumulations are disperse, frequently low saturation, accumulations in oceanic geologic media, having a variety of structural forms, as defined by Ginsburg and Soloviev (1998):

- massive: formed in coarse-grained sediments
- veined: occurring in fractures
- lenticular-bedded: formed as water segregates from host sediments
- porphyraceous: isometric inclusions ranging from 0.1 to 10 cm
- hydrate-rock: hydrate occupies more volume than sediment grains
- brecciated: cataclastic hydrate aggregates, common in fracture zones

A fundamental assumption associated with STOMP-HYD is that hydrate occurs in the geologic media as a pore filling deposit. This makes the simulator not directly applicable for all but the massive form of oceanic accumulations. Moridis and Sloan (2007) investigated the potential of producing oceanic accumulations (massive type) of hydrates using depressurization, considering the sensitivity to intrinsic permeability, porosity, formation pressure, formation temperature, hydrate saturation and production pressure. Their numerical simulation results indicated that despite varying the parameters to cover the spectrum of oceanic deposits, gas production was well below that needed for economic viability. From these results they concluded that disperse, low saturation oceanic accumulations would not be appropriate reservoirs for producing gas hydrates by means of depressurization. Production of oceanic hydrate accumulations using the CO<sub>2</sub> exchange technology has a potential advantage over dissociation-type production technologies in that the direct exchange of CO<sub>2</sub> with CH<sub>4</sub> as the guest molecule could maintain seafloor stability. Currently the STOMP-HYD simulator is not capable of addressing hydrate production problems where the hydrate form is not pore filling and where geomechanical strains need to be considered.



## 6.0 Conclusions

Estimates of vast amounts of global natural gas hydrate deposits make them an attractive unconventional energy resource. As with other unconventional energy resources, the challenge is to economically produce the natural gas fuel. The gas hydrate challenge is principally technical. Meeting that challenge will require innovation, but more importantly, primarily scientific research to understand the resource and its characteristics in porous media. Producing natural gas from gas hydrate deposits requires releasing methane from its clathrated form. The simplest way to release methane is to dissociate the hydrate by removing it from within the hydrate stability pressure and temperature conditions. The thermal stimulation production technology effectively dissociates the gas hydrate through heating. Whether the heat source is injected steam, an exothermic reaction, or electromagnetic, the effect is to raise the temperature of the gas hydrate above the equilibrium point, causing the hydrate to dissociate. This approach, however, suffers from poor recovery efficiencies and could possibly disrupt the hydraulic and mechanical properties of the produced reservoir. The depressurization production technology dissociates gas hydrate by lowering the pressure below the hydrate stability point. The self-regulating thermal nature of gas hydrates results in lower temperatures in the dissociation region and ultimately without an additional heat source, production rates will depend on heat transport into the reservoir (e.g., geothermal gradient). Depressurization is the most economical approach, but could also disrupt the produced reservoir. The inhibitor injection technology causes hydrate dissociation by shifting the equilibrium curve, but the approach is unattractive for environmental and economic reasons. The gas exchange technology releases methane by replacing it with a more thermodynamic molecule (e.g., carbon dioxide, nitrogen). This technology has three advantageous: 1) it sequesters greenhouse gas, 2) it releases energy via an exothermic reaction, and 3) it retains the hydraulic and mechanical stability of the hydrate reservoir. This technology currently has one disadvantage; its novelty. The gas exchange technology currently appears promising, but its success or failure will depend on the results of future scientific research and associated technology innovations.

### 6.1 Conclusions for Class 1 and 2 Gas Hydrate Accumulations

This investigation was focused on producing methane from an idealized Class 1 hydrate accumulation using a two-stage approach: 1) depressurization until production rates decreased and 2) carbon dioxide injection. To simplify the simulation complexity an idealized two-dimensional domain was modeled that ignored geologic heterogeneity and well geometric factors. The considered injection scenarios were limited to variations in the injectant form and screened intervals. The investigation did not consider the other production scenarios, which might include hydraulic fracturing and dormant pumping periods. Whereas the numerical simulations considered the processes of hydrate dissociation, formation, and guest molecule exchange, several assumptions were made in developing the mathematical models: 1) equilibrium distribution of carbon dioxide and methane in the aqueous, gas, liquid CO<sub>2</sub>, and gas hydrate phases, 2) equilibrium dissociation and formation of gas hydrate, 3) equilibrium large and small cage occupancies, 4) bulk hydrate properties. Given these constraints, a number of conclusions, listed below and illustrated in Figure 6.1, can be drawn about the effectiveness of producing methane from Class 1 hydrate accumulations:

1. An initial depressurization stage serves to rapidly produce methane through hydrate dissociation and increase the permeability of the hydrate zone.
2. Moderate injection pressures prevent the formation of pore plugging secondary gas hydrate.

3. Produced water was the lowest for the pure CO<sub>2</sub> injection scenarios, but the amount of produced water varied across the pure CO<sub>2</sub> injection temperatures and well screens dependent on the formation of secondary hydrate.
4. The additional produced methane with carbon dioxide injection is only about 10% of the original reservoir quantity, and largely due to the displacement of methane gas saturation in the gas zone.
5. Regardless of the injection well screening intervals the flow pattern for the injected carbon dioxide is predominately through the gas zone, bypassing the hydrate zone
6. The higher permeability gas zone reduces the contact of carbon dioxide with methane hydrate to the perimeter of the hydrate-bearing regions.
7. High pressure injection of carbon dioxide leads to secondary hydrate formation and pore plugging

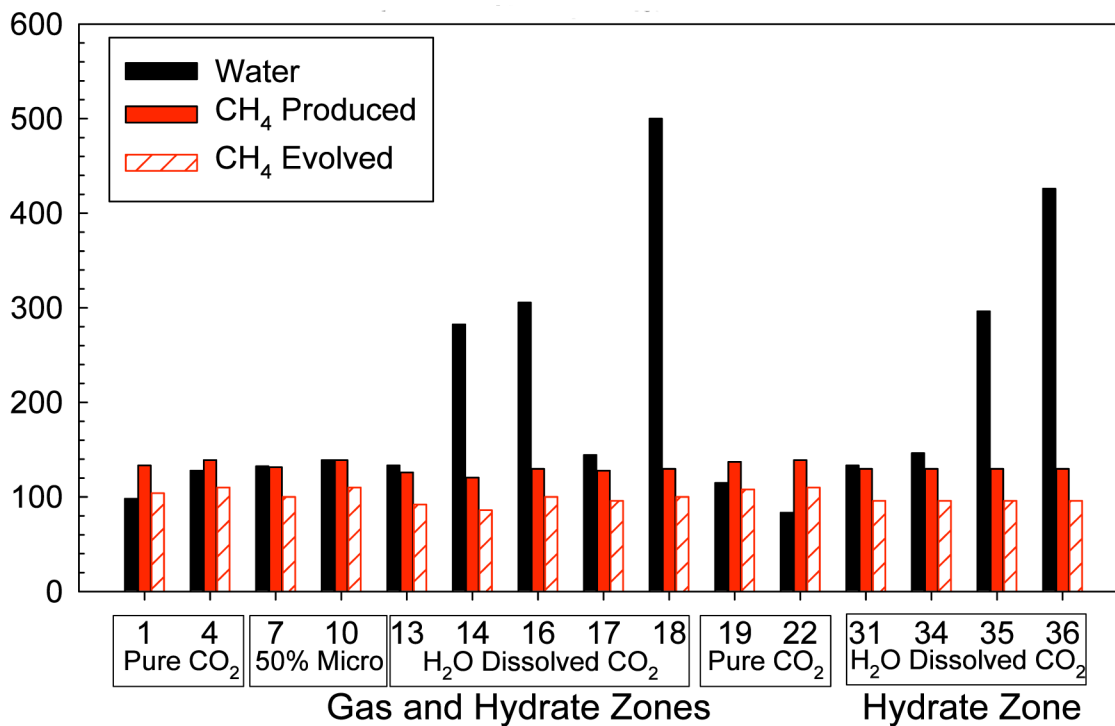


**Figure 6.1.** Summary of simulation results of class 1 hydrate accumulations

The numerical simulation of hydrate production via a hydrate dissociation process (e.g., thermal stimulation, depressurization, inhibitor injection) requires the solution of highly nonlinear coupled equations, using primary variable switching schemes to handle phase transitions. The injection of carbon dioxide increases the solution complexity by introducing an additional component (i.e., carbon dioxide) and the possibility of an additional phase (i.e., liquid CO<sub>2</sub>). The general observation is that time stepping and thus execution performance is limited by the resolution of phase transitions. Improvements to the phase transition algorithms could greatly improve execution performance.

## 6.2 Conclusions for Class 3 Gas Hydrate Accumulations

The permeable zones, characteristic of Class 1 and 2 hydrate accumulations, allowed for bypass of injected CO<sub>2</sub> and stimulated the formation of a mixed CH<sub>4</sub>-CO<sub>2</sub> barrier around the hydrate mass, both of which greatly diminished the contact of CO<sub>2</sub> with methane hydrate. It was anticipated that depressurization of a Class 3 hydrate over a short period would yield reduced hydrate saturations throughout the reservoir, providing increased effective permeability for the mobile fluids, including the injected forms of CO<sub>2</sub>. The numerical simulations, however, indicate that the short depressurization stage has little effect on the hydrate mass centered between the depressurization wells, not creating the desired increase in effective permeability. The subsequent injection of CO<sub>2</sub> as pure, 50% micro-emulsion or dissolved forms does not yield significant exchange of hydrate guest molecules nor increases in CH<sub>4</sub> production, as the centrally located hydrate mass remains relatively impermeable, not allowing the direct contact of injected CO<sub>2</sub> with CH<sub>4</sub> hydrate. These results indicate that direct injection techniques do not enhance CH<sub>4</sub> production and direct guest molecule exchange is inhibited by the low effective permeability of the hydrate zone. Missing from these investigations are those approaches that involve fracturing of the formation to create high permeability paths, diffusive migration of CO<sub>2</sub> through the hydrate zone, and the possibility for CH<sub>4</sub>-CO<sub>2</sub> separation technologies for the produced gas stream.

## 6.3 Conclusions for Class 4 Gas Hydrate Accumulations

Oceanic accumulations of gas hydrates are possibly the prevalent form on the planet and estimates by Kvenvolden (1988) put the amounts of methane in oceanic gas hydrates at two orders of magnitude greater than those in permafrost gas hydrates. When viewed from the perspective of countries without permafrost accumulations (e.g., Japan, Korea, India) the oceanic gas hydrates have greater attractiveness. The numerical simulation investigations of Moridis and Sloan (2007) have essentially eliminated using depressurization as a production technology for the disperse, low saturation accumulations. The complications with secondary hydrate formation that have been observed in the numerical simulation of Class 1, 2, and 3 gas hydrate accumulations are likely to prevent the use of classical petroleum production approaches (such as continuous injection/withdrawal of CO<sub>2</sub>) for realizing the potential of oceanic gas hydrates. One definitive reason for continuing to pursue gas hydrate guest molecule exchange technologies for producing oceanic accumulations is its potential to preserve the seafloor structure. Whereas the application of classical petroleum production approaches does not appear viable with respect to oceanic resources, there may be other innovative production approaches that yield methane and sequester carbon dioxide without disrupting the seafloor environment.

The overriding conclusion from these first simulation results suggests the principle difficulty to overcome with CO<sub>2</sub> injection to improve gas hydrate production is flow bypass around the gas hydrate-zone, which greatly limits the interfacial contact area achieved between the injected fluid phase and the gas hydrate. This problem has parallels with similar issues encountered in CO<sub>2</sub> floods used for enhanced oil production. Clearly additional work is needed to explore methods of artificially introducing high-permeability pathways in gas hydrate zones that may be exploited for injection of CO<sub>2</sub> in either gas, liquid, or micro-emulsion form to enhance gas hydrate production rates.



## 7.0 References

- Anderson, B., J. Wilder, M. Kurihara, M. White, G. Moridis, S. Wilson, M. Pooladi-Davish, Y. Masuda, T. Collett, T. Hunter, H. Narita, K. Rose, and R. Boswell, 2008, Analysis of modular dynamic formation test results from the mount elbert-01 stratigraphic test well, Milne Point unit, North Slope Alaska, Proceeding of the 6th International Conference on Gas Hydrates (ICGH 2008), Vancouver, British Columbia.
- Bear, J., and J. J. Nitao, 1995, On Equilibrium And Primary Variables In Transport In Porous-Media: *Transport In Porous Media*, v. 18, p. 151-184.
- Brooks, R. H., and A. T. Corey, 1966, Properties of Porous Media Affecting Fluid Flow: *Journal of Irrigation and Drainage Engineering*, v. 92, p. 61-88.
- Castaldi, M. J., Y. Zhou, and T. M. Yegulalp, 2007, Down-hole combustion method for gas production from methane hydrates: *Journal of Petroleum Science and Engineering*, v. 56, p. 176-185.
- Chatterji, J., and J. E. Griffith, 1988, *Methods of decomposing gas hydrates*, USA.
- Circone, S., S. H. Kirby, and L. A. Stern, 2005a, Direct measurement of methane hydrate composition along the hydrate equilibrium boundary: *Journal Of Physical Chemistry B*, v. 109, p. 9468-9475.
- Circone, S., S. H. Kirby, and L. A. Stern, 2005b, Thermal regulation of methane hydrate dissociation: Implications for gas production models: *Energy & Fuels*, v. 19, p. 2357-2363.
- Clennell, M. B., M. Hovland, J. S. Booth, P. Henry, and W. J. Winters, 1999, Formation of natural gas hydrates in marine sediments 1. Conceptual model of gas hydrate growth conditioned by host sediment properties: *Journal of Geophysical Research-Solid Earth*, v. 104, p. 22985-23003.
- Collett, T. S., 2004, Gas hydrates as a future energy resource: *Geotimes*, v. 49, p. 24-27.
- Ginsburg, G. D., and V. A. Soloviev, 1998, *Submarine Gas Hydrates*: St.Petersburg, VNIIOkeangeologia, 216 p.
- Goel, N., 2006, In situ methane hydrate dissociation with carbon dioxide sequestration: Current knowledge and issues: *Journal Of Petroleum Science And Engineering*, v. 51, p. 169-184.
- Graue, A., B.Kvamme, B. Baldwin, J. Stevens, J. Howard, E. Aspenes, G. Ersland, J. Husebø, and D. Zornes, 2006, Environmentally friendly CO<sub>2</sub> storage in hydrate reservoirs benefits from associated spontaneous methane production, *Proceedings of the Offshore Technology Conference (OTC-18087)*, Houston, Texas.
- Hirohama, S., Y. Shimoyama, A. Wakabayashi, S. Tatsuta, and N. Nishida, 1996, Conversion of CH<sub>4</sub>-hydrate to CO<sub>2</sub>-hydrate in liquid CO<sub>2</sub>: *Journal Of Chemical Engineering Of Japan*, v. 29, p. 1014-1020.

- Hunter, R. B., S. A. Digert, R. Boswell, and T. S. Collett, 2008, Alaska gas hydrate research and stratigraphic test preliminary results: 2007–2008 Arctic Energy Summit Proceedings.
- Ji, C., G. Ahmadi, and D. H. Smith, 2001, Natural gas production from hydrate decomposition by depressurization: *Chemical Engineering Science*, v. 56, p. 5801-5814.
- Jiang, Q., L. H. Liang, and M. Zhao, 2001, Modeling of the melting temperature of nano-ice in MCM-41 pores: *Journal Of Physics-Condensed Matter*, v. 13, p. L397-L401.
- KIGAM, 2006, *Studies on Gas Hydrate Development and Production Technology*: Korean Institute for Geosciences and Mineral Resources.
- Klauda, J. B., and S. I. Sandler, 2001, Modeling gas hydrate phase equilibria in laboratory and natural porous media: *Industrial & Engineering Chemistry Research*, v. 40, p. 4197-4208.
- Klauda, J. B., and S. I. Sandler, 2003, Phase behavior of clathrate hydrates: a model for single and multiple gas component hydrates: *Chemical Engineering Science*, v. 58, p. 27-41.
- Komai, T., Y. Yamamoto, and S. Ikegami, 1997, Equilibrium properties and kinetics of methane and carbon dioxide gas hydrate formation/dissociation: *Proceedings of American Chemical Society Fuel Chemistry Division*, p. 568-572.
- Kurihara, M., K. Funatsu, and K. Kusaka, 2005, Well-test analysis for gas hydrate reservoirs: Examination of parameters suggested by conventional analysis for the JAPEx/JNOC/GSC et al. Mallik 5L-38 gas hydrate production test results, *in* S. R. Dallimore, and T. S. Collett, eds., *Scientific Results from the Mallik 2002 Gas Hydrate Production Research Well Program*, Mackenzie Delta, Northwest Territories, Canada: Canada, Geological Survey of Canada Bulletin 585.
- Kvenvolden, K. A., 1988, Methane Hydrate - A Major Reservoir Of Carbon In The Shallow Geosphere: *Chemical Geology*, v. 71, p. 41-51.
- Lee, H., Y. Seo, Y. T. Seo, I. L. Moudrakovski, and J. A. Ripmeester, 2003, Recovering methane from solid methane hydrate with carbon dioxide: *Angewandte Chemie-International Edition*, v. 42, p. 5048-5051.
- Liu, J., L. J. Yan, G. J. Cheng, and T. M. Guo, 2002, Kinetics of methane hydrate dissociation in active carbon: *Acta Chimica Sinica*, v. 60, p. 1385-1389.
- McCabe, W. L., J. C. Smith, and P. Harriot, 2005, *Unit Operations of Chemical Engineering*: New York, McGraw, 163-165 p.
- McGrail, B. P., H. T. Schaefer, M. D. White, T. Zhu, A. S. Kulkarni, R. B. Hunter, S. L. Patil, A. T. Owen, and P. F. Martin. 2007. *Using Carbon Dioxide to Enhance Recovery of Methane from Gas Hydrate Reservoirs: Final Summary Report*. PNNL-17035, Pacific Northwest National Laboratory, Richland, Washington.
- McGrail, B. P., S. Ahmed, H. T. Schaefer, A. T. Owen, P. F. Martin, and T. Zhu, 2007, Gas hydrate property measurements in porous sediments with resonant ultrasound spectroscopy: *Journal of Geophysical Research-Solid Earth*, v. 112.

- McGrail, B. P., T. Zhu, R. B. Hunter, M. D. White, and S. L. Patil. 2004. *A New Method for Enhanced Production of Gas Hydrates with CO<sub>2</sub>*. PNNL-SA-41275, Pacific Northwest National Laboratory, Richland, WA.
- Milkov, A. V., G. E. Claypool, Y. J. Lee, W. Y. Xu, G. R. Dickens, and W. S. Borowski, 2003, In situ methane concentrations, at Hydrate Ridge, offshore Oregon: New constraints on the global gas hydrate inventory from an active margin: *Geology*, v. 31, p. 833-836.
- Moridis, G. J., 2002, Numerical simulation studies of thermally induced gas production from hydrate accumulations with no free gas zones at the Mallik Site, Mackenzie Delta, Canada: SPE 2002 Asia Pacific Oil and Gas Conference and Exhibition (SPE paper 77861 – LBNL-50256).
- Moridis, G. J., 2003, Numerical studies of gas production from methane hydrates: *SPE Journal*, v. 8, p. 359-370.
- Moridis, G. J., 2004, Numerical studies of gas production from Class 2 and Class 3 hydrate accumulations at the Mallik site, Mackenzie Delta, Canada: *Spe Reservoir Evaluation & Engineering*, v. 7, p. 175-183.
- Moridis, G. J., and T. S. Collett, 2003, Strategies for gas production from hydrate accumulations under various geologic conditions, Berkeley, CA, Lawrence Berkeley National Laboratory.
- Moridis, G. J., T. S. Collett, S. R. Dallimore, T. Satoh, S. Hancock, and B. Weatherill, 2004, Numerical studies of gas production from several CH<sub>4</sub> hydrate zones at the Mallik site, Mackenzie Delta, Canada: *Journal Of Petroleum Science And Engineering*, v. 43, p. 219-238.
- Moridis, G. J., M. B. Kowalsky, and K. Pruess, 2007, Depressurization-induced gas production from class 1 hydrate deposits: *Spe Reservoir Evaluation & Engineering*, v. 10, p. 458-481.
- Moridis, G. J., and E. D. Sloan, 2007, Gas production potential of disperse low-saturation hydrate accumulations in oceanic sediments: *Energy Conversion and Management*, v. 48, p. 1834-1849.
- Nakano, S., K. Yamamoto, and K. Ohgaki, 1998, Natural gas exploitation by carbon dioxide from gas hydrate fields - high-pressure phase equilibrium for an ethane hydrate system: *Proceedings Of The Institution Of Mechanical Engineers Part A-Journal Of Power And Energy*, v. 212, p. 159-163.
- Ohgaki, K., K. Takano, H. Sangawa, T. Matsubara, and S. Nakano, 1996, Methane exploitation by carbon dioxide from gas hydrates - Phase equilibria for CO<sub>2</sub>-CH<sub>4</sub> mixed hydrate system: *Journal Of Chemical Engineering Of Japan*, v. 29, p. 478-483.
- Ostergaard, K. K., R. Masoudi, B. Tohidi, A. Danesh, and A. C. Todd, 2005, A general correlation for predicting the suppression of hydrate dissociation temperature in the presence of thermodynamic inhibitors: *Journal Of Petroleum Science And Engineering*, v. 48, p. 70-80.
- Phale, H. A., T. Zhu, M. D. White, and B. P. McGrail, 2006, Simulation study on injection of CO<sub>2</sub>-microemulsion for methane recovery from gas-hydrate reservoirs: *Proceedings of 2006 SPE Gas Technology Symposium*.

- Pooladi-Darvish, M., 2004, Gas production from hydrate reservoirs and its modeling: *Journal Of Petroleum Technology*, v. 56, p. 65-71.
- Rice, W., 2003, Proposed system for hydrogen production from methane hydrate with sequestering of carbon dioxide hydrate: *Journal Of Energy Resources Technology-Transactions Of The Asme*, v. 125, p. 253-257.
- Rice, W., 2006, Hydrogen production from methane hydrate with sequestering of carbon dioxide: *International Journal Of Hydrogen Energy*, v. 31, p. 1955-1963.
- Rutqvist, J., and G. J. Moridis, 2007, Numerical studies of geochemical stability of hydrate-bearing sediments, *Offshore Technology Conference (OTC-18860)*, Houston, TX.
- Seo, Y. T., H. Lee, and J. H. Yoon, 2001, Hydrate phase equilibria of the carbon dioxide, methane, and water system: *Journal Of Chemical And Engineering Data*, v. 46, p. 381-384.
- Setzmann, U., and W. Wagner, 1991, A New Equation Of State And Tables Of Thermodynamic Properties For Methane Covering The Range From The Melting Line To 625-K At Pressures Up To 1000-Mpa: *Journal Of Physical And Chemical Reference Data*, v. 20, p. 1061-1155.
- Sloan, D. E., 1997, *Clathrate Hydrates of Natural Gases*: New York, Marcel Dekker, Inc.
- Sloan, E. D., and C. A. Koh, 2007, *Clathrate hydrates of natural gases*, CRC Press, 721 p.
- Smith, D. H., K. Seshadri, and J. W. Wilder, 2001, Assessing the thermodynamic feasibility of the conversion of methane hydrate into carbon dioxide hydrate in porous media, *Proceedings of First National Conference on Carbon Sequestration*, Washington D.C., National Energy Technology Laboratory.
- Span, R., and W. Wagner, 1996, A new equation of state for carbon dioxide covering the fluid region from the triple-point temperature to 1100 K at pressures up to 800 MPa: *Journal Of Physical And Chemical Reference Data*, v. 25, p. 1509-1596.
- Stevens, J., J. Howard, B. Baldwin, G. Ersland, J. Husebø, and A. Graue, 2008, Experimental hydrate formation and production scenarios based on CO<sub>2</sub> sequestration: *Proceeding of the 6th International Conference on Gas Hydrates (ICGH 2008)*.
- Sung, W. M., H. Lee, S. Kim, and H. Kang, 2003, Experimental investigation of production behaviors of methane hydrate saturated in porous rock: *Energy Sources*, v. 25, p. 845-856.
- Tang, L. G., R. Xiao, C. Huang, Z. P. Feng, and S. S. Fan, 2005, Experimental investigation of production behavior of gas hydrate under thermal stimulation in unconsolidated sediment: *Energy & Fuels*, v. 19, p. 2402-2407.
- Tohidi, B., R. Anderson, M. B. Clennell, R. W. Burgass, and A. B. Biderkab, 2001, Visual observation of gas-hydrate formation and dissociation in synthetic porous media by means of glass micromodels: *Geology*, v. 29, p. 867-870.
- Tsympkin, G. G., 2000, Mathematical models of gas hydrates dissociation in porous media: *Gas Hydrates: Challenges For The Future*, v. 912, p. 428-436.

- Turner, C. A., and E. D. J. Sloan, 2002, Hydrate phase equilibria measurements and predictions in sediments, Proceedings of 4th International Conference on Gas Hydrates Yokohama, Japan.
- White, M. D., and B. P. McGrail, 2006, STOMP-HYD: A new numerical simulator for analysis of methane hydrate production from geologic formations Proceedings of 2nd International Symposium on Gas Hydrate Technology Daejeon, Korea, KIGAM
- White, M. D., and B. P. McGrail, 2008a, Designing a pilot-scale experiment for the production of natural gas hydrates and sequestration of CO<sub>2</sub> in Class 1 Hydrate Accumulations, 9th International Conference on Greenhouse Gas Control Technologies, Washington D.C., GHGT-9.
- White, M. D., and B. P. McGrail, 2008b, Numerical simulation of methane hydrate production from geologic formations via carbon dioxide injection (OTC-19458), Proceedings of the Offshore Technology Conference, Houston, TX, OTC.
- White, M. D., and M. Oostrom, 2000, STOMP Subsurface Transport Over Multiple Phases, Version 2.0, Theory Guide, Richland, WA, Pacific Northwest National Laboratory.
- White, M. D., S. K. Wurstner, and B. P. McGrail, 2009, Numerical studies of methane production from Class 1 gas hydrate accumulations enhanced with carbon dioxide injection: Marine and Petroleum Geology (submitted).
- Wilder, J. W., G. J. Moridis, S. J. Wilson, M. Kurihara, M. D. White, Y. Masuda, and B. J. Anderson, 2008, An international effort to compare gas hydrate reservoir simulators, Proceedings of the 6th International Conference on Gas Hydrates, Vancouver, British Columbia, Canada, ICGH.
- Wilder, J. W., K. Seshadri, and D. H. Smith, 2002, Thermodynamics of the sequestration of carbon dioxide in methane hydrates in porous media. : ACS Fuel Chemistry Division Preprints, v. 47.



## **Appendix A**

# Numerical studies of methane hydrate production at moderate temperatures via carbon dioxide exchange

Mark D. White<sup>‡a</sup>, B. Peter McGrail<sup>b</sup>, Tao Zhu<sup>c</sup>, Hemant Phale<sup>c</sup>

<sup>a</sup>*Hydrology Group, Pacific Northwest National Laboratory, Richland, Washington*

<sup>b</sup>*Applied Geology and Geochemistry, Pacific Northwest National Laboratory, Richland, Washington*

<sup>c</sup>*Department of Petroleum Engineering, University of Alaska, Fairbanks, Fairbanks, Alaska*

## Abstract

Methane hydrate dissociation under moderate thermal stimulation is numerically simulated for a series of problems that investigate different production strategies involving carbon dioxide injection and molecular exchange. Methane hydrate production is predicted for a five-spot well configuration pattern; where, microemulsions of carbon dioxide are injected with water at temperatures below 30°C. Numerical simulations were executed using a new operational mode, referred to as STOMP-HYD, of the multifluid subsurface flow and reactive transport simulator, STOMP. The simulator using Newton-Raphson iteration to solve the coupled nonlinear governing equations, describing the conservation of water, methane, carbon dioxide and sodium chloride mass and thermal energy for a geologic system comprising aqueous, liquid carbon dioxide, gas, hydrate, ice and solid matrix phases. Hydrate saturation is computed from the ratio of hydrate equilibrium pressures *in-situ* and *ex-situ*, assuming the hydrate phase is completely occluded by aqueous phase. Relative permeability of the mobile phases are computed using multifluid constitutive relations, assuming a the wettability order: aqueous, liquid carbon dioxide, gas. Kinetics of hydrate dissociation/formation and hydrate molecular exchange is considered. Simulation results indicate that methane production at moderate injection temperatures is feasible using water and carbon dioxide as co-injectants.

*Keywords: gas hydrate mixture, methane, carbon dioxide, multifluid subsurface flow and transport, numerical simulation*

## 1. Introduction

Gas hydrates are crystalline structures comprising water and gas; where, gas molecules are completely surrounded by a lattice of water molecules forming a cage-like structure or clathrate. Naturally occurring methane (CH<sub>4</sub>) hydrates form under low temperature and high pressure conditions and have been found in large deposits in sediments beneath the ocean floor and permafrost. One liter of CH<sub>4</sub> hydrate under in-situ conditions can contain as much as 164 liters of CH<sub>4</sub> gas under standard temperature and pressure (STP) conditions (Collett, 1993). The clathrate structure, therefore, has enormous storage capacity for CH<sub>4</sub>, making the world's hydrate deposits a vast source of natural gas. Conversely, the same clathrate structure can hold other gas molecules, such as carbon dioxide (CO<sub>2</sub>), making the stability regions for hydrates a vast reservoir for CO<sub>2</sub> sequestration.

## 2. Multifluid transport equations

---

<sup>‡</sup> Corresponding author. Address: Pacific Northwest National Laboratory, MSIN K9-33, P.O. Box 999, Richland, WA 99352, USA. Tel: 509-372-6070. Fax: 509-372-6089. E-mail: mark.white@pnl.gov.

Four mass conservation and one energy conservation equations are used to describe the subsurface hydrate system; where, the conserved mass components are water, CO<sub>2</sub>, CH<sub>4</sub>, and salt. Transport is assumed to occur over three mobile phases, aqueous, liquid CO<sub>2</sub>, and gas; and four immobile phases, hydrate, ice, precipitated salt, and host porous media. The aqueous phase comprises liquid water, dissolved CO<sub>2</sub>, dissolved CH<sub>4</sub>, and dissolved salt. The gas phase comprises water vapor, gaseous CO<sub>2</sub>, and gaseous CH<sub>4</sub>. The hydrate phase comprises water, CO<sub>2</sub>, and CH<sub>4</sub> in a crystalline clathrate structure. The liquid CO<sub>2</sub> phase is considered a nonaqueous phase liquid comprising only liquid CO<sub>2</sub>; dissolution of CH<sub>4</sub> is ignored. Ice and precipitated salt phases are single component phases comprising water and salt, respectively.

### 2.1 Energy conservation equation

Energy transport occurs over all seven mobile and immobile phases according to an energy conservation equation, which can be expressed in differential form as:

$$\begin{aligned} \frac{\partial}{\partial t} \left[ \sum_{\gamma=l,g,n,h,i,p} \left( \phi \rho_{\gamma} s_{\gamma} u_{\gamma} \right) + (1-\phi) \rho_s u_s \right] = & - \sum_{\gamma=l,g,n} \left[ \nabla \left( h_{\gamma} \mathbf{F}_{\gamma} \right) \right] \\ - \sum_{\xi=w,a,o} \nabla \left( h_g^{\xi} \mathbf{J}_g^{\xi} \right) - \nabla \left( \mathbf{k}_e \nabla T \right) + \sum_{\gamma=l,g,n} \left( h_{\gamma} \dot{m}_{\gamma} \right) + \dot{q} \end{aligned} \quad (1)$$

Equation (1) states that the accumulation of energy in the mobile and immobile phases in a control volume is balanced with the energy advected into the control volume by the mobile phases, diffused into the control volume via the gas phase, conducted into the control volume, plus the energy associated with mobile phase sources and thermal energy sources. It should be noted that the energy associated with diffusion of components in the aqueous and liquid CO<sub>2</sub> phases is ignored and the porous media is assumed to be void of unconnected pore space.

### 2.2 Mass conservation equations

Mass transport of the conserved components (i.e., water, CO<sub>2</sub>, CH<sub>4</sub>, and salt) occurs over the three mobile phases and three immobile phases, excluding the host porous media, according to a mass conservation equation, which can be expressed in differential form as:

$$\begin{aligned} \frac{\partial}{\partial t} \left[ \sum_{\gamma=l,g,n,h,i,p} \left( \phi \rho_{\gamma} s_{\gamma} \omega_{\gamma}^{\xi} \right) \right] = & - \sum_{\gamma=l,g,n} \left[ \nabla \left( \omega_{\gamma}^{\xi} \mathbf{F}_{\gamma} \right) \right] \\ - \sum_{\gamma=l,g} \left[ \nabla \left( \mathbf{J}_{\gamma}^{\xi} \right) \right] + \sum_{\gamma=l,g,n} \left( \omega_{\gamma}^{\xi} \dot{m}_{\gamma} \right); \text{ for } \xi = w, a, o, s \end{aligned} \quad (2)$$

As with energy, the component mass conservation equations state that the accumulation of component mass is balanced with the component mass advected into the control volume via mobile phases, diffused into the control volume via the aqueous and gas phases, plus the component mass associated with mobile phase sources. Sorption of component on the host porous media is ignored, which eliminates the porous media phase from the governing equations for component mass. Diffusion transport through the liquid CO<sub>2</sub> phase is ignored, consistent with the pure CO<sub>2</sub> assumption for the NAPL.

### 2.3 Advective and diffusive-dispersive fluxes

Advective mass flux for the mobile phases occurs in response to gradients in phase pressure and gravitational body forces (i.e., buoyance forces):

$$\mathbf{F}_\gamma = -\frac{\rho_\gamma k_{r\gamma} \mathbf{k}_i}{\mu_\gamma} \left( \nabla P_\gamma + \rho_\gamma g \mathbf{z}_g \right); \text{ for } \gamma = l, g, n \quad (3)$$

Diffusive component mass flux for the aqueous and gas phases occurs in response to gradients in the component mole fraction:

$$\mathbf{J}_\gamma^\xi = -\tau_\gamma \phi \rho_\gamma s_\gamma \left( \frac{M^\xi}{M_\gamma} \right) \mathbf{D}_\gamma^\xi \left( \nabla \chi_\gamma^\xi \right); \text{ for } \gamma = l \text{ and } \xi = w, a, o, s \quad (4)$$

$$\text{for } \gamma = g \text{ and } \xi = w, a, o$$

Field variables (e.g., pressure, temperature, density, viscosity) are computed at the grid cell centroid. Flux variables (e.g., advective mass flux, diffusive component flux, thermal energy flux) are computed at the surface centroids between two grid cells. Field variables used in computing flux variables are averaged to the flux variable locations. Donor-cell averaging is used to compute density and relative permeability field variables at flux locations; whereas, harmonic averaging is used for all other field variables at the flux locations.

## 3. Constitutive equations

Constitutive equations mathematically relate the variables in the governing conservation equations. The governing energy and component mass conservation equations are solved for five primary variables. The constitutive equations close the system of equations, by relating the primary variables to the secondary variables. A primary variable switching scheme is used to handle phase transitions and disappearances.

### 3.1 Phase saturation

Phase saturation describes the fraction of pore volume occupied by a phase. Phase saturation relations are dependent on a phase distribution and wettability conceptual model for the hydrate hydrologic system. The phase distribution conceptual model is assumed to follow the model proposed by Clennell (1999); where hydrate is assumed to be totally occluded by aqueous, and the wettability order is aqueous, liquid CO<sub>2</sub>, gas. This conceptual model of phase distribution is depicted in Fig. 1. Following this conceptual model we define the sum of the effective hydrate and effective aqueous saturations as the apparent aqueous saturation; the sum of the apparent aqueous saturation and effective liquid CO<sub>2</sub> saturation as apparent total liquid saturation; and one minus the apparent total liquid saturation as the effective gas saturation:

$$\bar{s}_t = \bar{s}_n + \bar{s}_l = \bar{s}_n + \bar{s}_l + \bar{s}_h = \frac{s_n}{(1-s_{lr})} + \frac{s_l - s_{lr}}{(1-s_{lr})} + \frac{s_h}{(1-s_{lr})} = 1 - \bar{s}_g = 1 - \frac{s_g}{(1-s_{lr})} \quad (5)$$

The apparent total liquid saturation is a function of the scaled interfacial pressure difference between the gas and liquid CO<sub>2</sub> phases; and the apparent aqueous saturation is a function of the scaled interfacial pressure difference between the liquid CO<sub>2</sub> and aqueous phases:

$$\bar{s}_t = \text{func} \left[ \beta_{gn} (P_g - P_n) \right]; \bar{s}_l = \text{func} \left[ \beta_{nl} (P_n - P_l) \right] \quad (6)$$

where; the interfacial scaling factors are described by the interfacial tension and reference fluid-pair interfacial tension:

$$\beta_{gn} = \frac{\sigma_{ref}}{\sigma_{gn}}; \beta_{nl} = \frac{\sigma_{ref}}{\sigma_{nl}}; \beta_{gl} = \frac{\sigma_{ref}}{\sigma_{gl}} \quad (7)$$

In the absence, of liquid CO<sub>2</sub>, the liquid CO<sub>2</sub> pressure is set to the critical pressure, which is equivalent to making the apparent total liquid and apparent aqueous saturations a function the scaled interfacial pressure difference between gas and aqueous:

$$P_n = P_n^c = \max \left[ \frac{\beta_{gn} P_g + \beta_{nl} P_l}{\beta_{gn} + \beta_{nl}}, P_l + \frac{\psi_{ref}}{\beta_{nl}} \right] \quad (8)$$

This scaling approach allows soil-moisture characteristics to be measured on other reference fluid pairs (e.g., water-air), and the functional expressions for the phase saturation can include familiar forms (van Genuchten 1980; Brooks and Corey 1964; Haverkamp et al. 1977).

### 3.2 Hydrate saturation

Conceptually the hydrate saturation could be determined from the scaled difference between the aqueous and hydrate pressures; where, the hydrate pressure refers to the hydrate phase pressure. The difficulty with this approach is determining the hydrate phase pressure. The pressure difference across the hydrate-aqueous interface can be determined from the hydrate-aqueous radius of curvature:

$$(P_h - P_l) = \frac{\xi_{hl} \sigma_{hl} \cos(\theta_{hl})}{r_{hl}} \quad (9)$$

Assuming a shape factor, for spherical contact, equal to 2 and a contact angle equal to 0, Equation (9) can be reduced

$$(P_h - P_l) = \frac{2 \sigma_{hl}}{r_{hl}} \quad (10)$$

Klauda and Sandler (2001) computed equilibrium pressures for hydrates *ex-situ* and *in-situ* using an equilibrium condition between the water in the aqueous phase and hydrate

$$f_h^w(T, P_{eq}, \bar{\chi}_g^o)^{ex} = f_l^w(T, P_{eq}, \bar{\chi}_g^o)^{ex} \quad (11)$$

$$f_h^w(T, P_{eq}, \bar{\chi}_g^o)^{in} = f_l^w(T, P_{eq}, \bar{\chi}_g^o)^{in} \exp\left(-\frac{v_l^w \xi_{hl} \alpha_{hl} \cos(\theta_{hl})}{r_{hl} RT}\right) \quad (12)$$

Using the computer code developed by Klauda and Sandler (2003) to compute equilibrium pressure *ex-situ* and *in-situ* over a range of temperature, CH<sub>4</sub> gas phase mole fractions (excluding water), the following functional form was derived, relating the ratio of *in-situ* over *ex-situ* equilibrium pressures with the radius of curvature for the hydrate-aqueous interface:

$$\frac{P_{eq}^{in}}{P_{eq}^{ex}} = 1 + \frac{a}{\left(1 + \exp\left(\frac{\ln(r_{hl}) + b}{c}\right)\right)}; \text{ where, } \begin{aligned} a &= 0.1145 \\ b &= 17.09 \\ c &= 0.8817 \end{aligned} \quad (13)$$

The equilibrium pressure ratio function is shown in Fig. 2 and indicates a sharp change in the equilibrium pressure ratio for pore radii smaller than about 6000 Å. In contrast Turner and Sloan (2002) predicted that significant deviations from *ex-situ* equilibrium conditions were not likely for pore radii greater than 600 Å. Equation (13) provides a relationship between the equilibrium pressure ratio and the hydrate-aqueous interfacial radius, needed to compute capillary pressure difference between the hydrate and aqueous phases, per Equation (10), which then was used in the user-specified soil moisture retention function to calculate hydrate saturation. In Equation (13), the *ex-situ* equilibrium pressure was computed from the mole fraction of hydrate formers (excluding water) and the temperature, from a tabular data generated from Sloan (1997). The *in-situ* equilibrium pressure was computed as the sum of the gas-phase partial pressures of CO<sub>2</sub> and CH<sub>4</sub>.

**3.3 Hydrate composition, density, enthalpy, and thermal conductivity**

Three dimensional hydrate property data tables were generated from Sloan (1997) based on temperature, gas-phase mole fraction (excluding water) of CH<sub>4</sub>, and aqueous-phase mass fraction of salt. Trilinear interpolation of the table data was used to generate the *ex-situ* equilibrium pressure, hydrate mole fraction (excluding water) of CH<sub>4</sub>, CO<sub>2</sub> small- and large-cage occupancy numbers, and CH<sub>4</sub> small- and large-cage occupancy numbers. Hydration number and hydrate mole fraction of water were computed from the small and large-cage occupancy numbers, according to Sloan (1997):

$$n_h^w = \frac{23}{3(y_L^a + y_L^o) + (y_S^a + y_S^o)}; \chi_h^w = \frac{n_h^w}{1 + n_h^w} \quad (14)$$

Hydrate density was computed from the small and large cage occupancy number, assuming sl hydrate crystal cell structure, according to Sloan (1997):

$$\rho_h = 10^3 \frac{46 M^w + (2 y_S^a + 6 y_L^a) M^a + (2 y_S^o + 6 y_L^o) M^o}{(12.8 \times 10^{-8})^3 N} \quad (15)$$

where; 46 is the number of water molecules per unit cell in the sI hydrate structure and  $12.8 \times 10^{-8}$  m is the volume of a unit cell in the sI hydrate structure. Hydrate enthalpy was computed using the heat of dissociation from Yoon et al. (2003), and the specific heat of hydrate from Handa (1986):

$$h_h = \omega_h^w h_o^w + \omega_h^a h_o^a + \omega_h^o h_o^o + \frac{[57.66 \times 10^{-6} \chi_h^a + 53.81 \times 10^{-6} \chi_h^o]}{M_h} \quad (16)$$

$$h_o^w = h_{liq}^w (273.15 \text{ K}, 101325 \text{ Pa})$$

$$+ (c_p)_h (T - T_o); \text{ where, } h_o^a = h_{gas}^a (273.15 \text{ K}, 101325 \text{ Pa})$$

$$h_o^o = h_{gas}^o (273.15 \text{ K}, 101325 \text{ Pa})$$

Thermal conductivity of the hydrate phase was considered independent of hydrate composition, but slightly dependent on temperature (Waite et al 2002):

$$k_h = 0.5 - 3.75 \times 10^{-4} (T, ^\circ C) \quad (17)$$

### 3.4 CO<sub>2</sub> and CH<sub>4</sub> thermodynamic and transport properties

Two-dimensional thermodynamic property data tables based on temperature and pressure were generated from Span and Wagner (1996) for CO<sub>2</sub> and Setzmann and Wagner (1991) for CH<sub>4</sub>. Density, enthalpy, internal energy and fugacity for pure liquid and vapor CO<sub>2</sub>, and vapor CH<sub>4</sub> were determined from bilinear interpolation on temperature and pressure using these tables. The viscosity of pure liquid and vapor CO<sub>2</sub> was computed from temperature and density using the formulation of Feghhour et al. (1998):

$$\mu^a = \mu_o^a + \mu_e^a$$

$$\mu_o^a = \frac{1.00697 \times 10^{-6} T^{1/2}}{\exp \left[ \sum_{i=0}^4 a_i (\ln(T_r))^i \right]}$$

$$a_o = 0.235156, a_1 = -0.491266, a_2 = 0.05211155, a_3 = 0.05347906$$

where,

$$a_4 = -0.01537102, T_r = \frac{kT}{\varepsilon}, \frac{k}{\varepsilon} = 251.196 \text{ K} \quad (18)$$

$$\mu_e^a = d_{11} \rho^a + d_{21} (\rho^a)^2 + \frac{d_{64} (\rho^a)^2}{(T_r)^3} + d_{81} (\rho^a)^8 + \frac{d_{82} (\rho^a)^8}{(T_r)^8}$$

where,

$$d_{11} = 0.4071119 \times 10^{-8}, d_{21} = 0.7198037 \times 10^{-10}$$

$$d_{64} = 0.2411697 \times 10^{-22}, d_{81} = 0.2971072 \times 10^{-28}, d_{82} = -0.1627888 \times 10^{-28}$$

Similarly, the viscosity of pure vapor CH<sub>4</sub> was computed from temperature and density using the formulation of Kiselev et al. (1998):

$$\mu^o = \mu_o^o + \mu_e^o$$

$$\mu_o^o = \frac{0.757016 \times 10^{-6} T^{1/2}}{\frac{a_o}{(T_r)^{a_1}} + a_2 \exp(-a_3 (T_r)) + a_4 \exp(-a_5 (T_r))}$$

$$a_o = 1.16145, a_1 = 0.14874, a_2 = 0.52487, a_3 = 0.77320$$

where,

$$a_4 = 2.16178, a_5 = 2.43787, T_r = \frac{kT}{\varepsilon}, \frac{k}{\varepsilon} = 148.6 \text{ K} \quad (19)$$

$$\mu_e^o = 10^{-7} \exp \left( d_1 + \frac{d_2}{T} \right) \left[ \exp \left[ \left( d_3 + \frac{d_4}{T^{3/2}} \right) (\bar{\rho}^o)^{0.1} + \left( \frac{\bar{\rho}^o}{\bar{\rho}_c^o} - 1 \right) (\bar{\rho}^o)^{0.5} \left( d_5 + \frac{d_6}{T} + \frac{d_7}{T^2} \right) \right] - 1 \right]$$

where,

$$d_1 = -11.1460, d_2 = 442.232, d_3 = 11.9729, d_4 = -40000.8$$

$$d_5 = 0.01285, d_6 = 13.2309, d_7 = 1873.14$$

Two-dimensional thermal conductivity data based on temperature and density were generated for liquid and vapor CO<sub>2</sub>, using the correlations of Vesovic et al. (1990). Thermal conductivity of liquid and vapor CO<sub>2</sub> were computed using bilinear interpolation on temperature and density using these tables. Thermal conductivity of vapor CH<sub>4</sub> was computed using the formulation of Kiselev et al. (1998):

$$k^o = k_o^o + k_e^o$$

$$k_o^o = 10^3 \left[ f_1(T) \left[ c_{p_o}(T) - \frac{5}{2} R \right] + \frac{15}{4} R \right] \frac{\mu_o^o(T)}{M^o};$$

$$f_1(T) = 1.35558587 - 0.11306676 \frac{T_c^o}{T};$$

$$c_{p_o}(T) = g_1 T^{0.1} + \sum_{j=1}^3 g_{2j} \exp\left(\frac{g_{2j+1}}{T}\right) \frac{\left(\frac{g_{2j+1}}{T}\right)^2}{\left(\exp\left(\frac{g_{2j+1}}{T}\right) - 1\right)^2}; \quad (20)$$

$$\text{where, } g_1 = 4.0, g_2 = 3.00573, g_3 = 1870.0, g_4 = 1.85529$$

$$g_5 = 2180.0, g_6 = 4.07954, g_7 = 4170.0$$

$$k_e^o = 10^{-3} \frac{\bar{\rho}^o}{\bar{\rho}_c^o} \left[ b_1 + b_2 \left(\frac{\bar{\rho}^o}{\bar{\rho}_c^o}\right)^2 + \left(b_3 + b_4 \frac{T_c^o}{T}\right) \left(\frac{\bar{\rho}^o}{\bar{\rho}_c^o}\right)^3 + \left(b_5 + b_6 \frac{T_c^o}{T}\right) \left(\frac{\bar{\rho}^o}{\bar{\rho}_c^o}\right)^4 \right];$$

$$\text{where, } b_1 = 21.30511, b_2 = 11.07070, b_3 = -5.744289$$

$$b_4 = 0.140431, b_5 = 1.670839, b_6 = -0.095669$$

which requires the calculation of zero-density limit viscosity of CH<sub>4</sub> per Equation (19).

### 3.5 Water thermodynamic and transport properties

The thermodynamic and transport properties of liquid water and water vapor were generally obtained from the ASME Steam Table Formulations (Meyer et al., 1993), as described in the STOMP Theory Guide (White and Oostrom, 2000), including density, viscosity, enthalpy, internal energy, and thermal conductivity.

### 3.6 Aqueous-phase thermodynamic and transport properties

The aqueous phase was assumed to comprise liquid water, dissolved salt, dissolved CO<sub>2</sub> and dissolved CH<sub>4</sub>. The primary unknown for all phase conditions for the salt mass balance equation is total nodal salt mass, expressed in terms of the aqueous mass fraction of salt. The solubility limit for salt in the aqueous phase is computed according to the correlation of McKibbin and McNabb (1993):

$$\max \omega_l^s = 2.6218 \times 10^{-1} + 7.2 \times 10^{-5} (T, C) + 1.06 \times 10^{-6} (T, C)^2 \quad (21)$$

Total salt mass that results in aqueous phase salt mass fractions above the solubility limit is considered to be precipitated. Precipitated salt can reduce the intrinsic permeability through a reduction

factor correlation by Verma and Pruess (1988). The aqueous concentrations of dissolved CO<sub>2</sub> and CH<sub>4</sub> are computed from the component fugacity and a component specific Henry's coefficient that's dependent on temperature, aqueous salt concentration and pressure, through the Poynting correction factor (Reid et al., 1987):

$$\chi_l^a = \frac{f_g^a}{H_l^a}; \chi_l^o = \frac{f_g^o}{H_l^o} \quad (22)$$

For phase conditions without liquid CO<sub>2</sub>, the primary unknowns for CO<sub>2</sub> and CH<sub>4</sub> mass are the gas-phase partial pressures of the components. Component fugacity is computed from temperature and component partial pressure from the component property data tables, as described in section 3.4. The pressure independent Henry's coefficient for CO<sub>2</sub>, including the salting-out coefficient, was computed from the formulation of Battistelli et al. (1997):

$$H_l^a = \sum_{i=0}^5 b_i (T, C)^i \left[ 10^{\left( m_l^a \sum_{i=0}^4 c_i (T, C)^i \right)} \right]; \text{ where,} \quad (23)$$

$$b_0 = 7.83666 \times 10^7, b_1 = 1.96025 \times 10^6, b_2 = 8.20574 \times 10^4, b_3 = -7.40674 \times 10^2$$

$$b_4 = 2.18380, b_5 = -2.20999 \times 10^{-3}, c_0 = 1.19784 \times 10^{-1}, c_1 = -7.17823 \times 10^{-4}$$

$$c_2 = 4.93854 \times 10^{-6}, c_3 = -1.03826 \times 10^{-8}, c_4 = 1.08233 \times 10^{-11}$$

Conversely, the pressure independent Henry's coefficient for CH<sub>4</sub>, including the salting-out coefficient, was computed using the formulation of Sloan (1998):

$$H_l^o = \exp \left( - \left[ \frac{d_0}{R^o} + \frac{d_1}{R^o T} + \frac{d_2}{R^o} \ln(T) + \frac{d_3 T}{R^o} \right] \right) \left[ 10^{\left( m_l^o \sum_{i=0}^3 e_i (T, C)^i \right)} \right]; \text{ where,} \quad (24)$$

$$d_0 = -3.65183 \times 10^2, d_1 = 1.81067 \times 10^4, d_2 = 4.97554 \times 10^1, d_3 = -2.85 \times 10^{-4}$$

$$e_0 = 1.668 \times 10^{-1}, e_1 = -1.09236 \times 10^{-3}, e_2 = 7.81043 \times 10^{-6}, e_3 = -1.5234 \times 10^{-8}$$

Aqueous density was computed starting with pure liquid water density as a function of temperature and pressure from the ASME Steam Table Formulations (Meyer et al., 1993). Pure water liquid density was then corrected for salt concentration using the formulations of Haas (1976):

$$\rho_b = 10^3 \left( \frac{10^3 + m_l^s M^s}{10^3 v^w + m_l^s \bar{v}_l^s} \right)$$

$$\bar{v}_l^s = c_0 + c_1 v^w + c_2 (v^w)^2 + (c_3 + c_4 v^w) \left( \frac{v_c^w}{v_c^w - v^w} \right)^2 ; \quad (25)$$

where,  $c_0 = -167.219$ ,  $c_1 = 448.55$ ,  $c_2 = -261.07$ ,

$$c_3 = -13.644, c_4 = 13.97, v_c^w = 3.1975 \frac{\text{cm}^3}{\text{gm}}$$

where, the pure water liquid density was used to compute the vapor saturated specific volume of liquid water. Brine (saline aqueous) density was then corrected for dissolved CO<sub>2</sub> and CH<sub>4</sub>, using a temperature dependent partial molar volume formulation for CO<sub>2</sub> (Anderson et al., 1992) and a constant partial molar volume for CH<sub>4</sub>:

$$\rho_l = \frac{\rho_b}{\left( 1 + \frac{\rho_b \bar{v}_l^a \omega_l^a}{M^a} + \frac{\rho_b \bar{v}_l^o \omega_l^o}{M^o} - \omega_l^a - \omega_l^o \right)} \quad (26a)$$

$$\bar{v}_l^a = 10^{-3} \sum_{i=0}^4 b_i (T, ^\circ\text{C})^i$$

$$b_0 = 37.36, b_1 = -7.109 \times 10^{-2}, b_2 = -3.812 \times 10^{-5} \quad (26b)$$

$$b_3 = 3.296 \times 10^{-6}, b_4 = -3.702 \times 10^{-9}, \bar{v}_l^o = 37.3 \times 10^{-3} \frac{\text{m}^3}{\text{kmol}}$$

Aqueous viscosity was computed starting with pure liquid water viscosity as a function of temperature and pressure from the ASME Steam Table Formulations (Meyer et al., 1993). Pure water liquid viscosity was then corrected for salt concentration using the formulations of Phillips et al. (1981):

$$\mu_b = \mu_l^w \left( 1 + a_0 m_l^s + a_1 (m_l^s)^2 + a_2 (m_l^s)^3 + a_3 (T, ^\circ\text{C}) \left( 1 - \exp(a_4 m_l^s) \right) \right); \quad (27)$$

where,  $a_0 = 0.0816$ ,  $a_1 = 0.0122$ ,  $a_2 = 0.000128$ ,  $a_3 = 0.000629$ ,  $a_4 = -0.7$

Brine (saline aqueous) viscosity was then corrected for dissolved CO<sub>2</sub> and CH<sub>4</sub>, using the formulation of Grunberg and Nissan (Reid et al., 1987):

$$\mu_l = \exp \left( \left( 1 - \chi_l^a - \chi_l^o \right) \ln(\mu_b) + \chi_l^a \ln(\mu_g^a) + \chi_l^o \ln(\mu_g^o) \right) \quad (28)$$

Aqueous thermal conductivity was computed starting with pure liquid water thermal as a function of temperature and pressure from the ASME Steam Table Formulations (Meyer et al., 1993), and then corrected for salt concentration using the formulations of Ozbek and Phillips (1980):

$$k_l = k_l^w \left[ 1 - \left( c_0 + c_1 (T, ^\circ C) + c_2 (T, ^\circ C)^2 \right) \omega_l^s + \left( c_3 + c_4 (T, ^\circ C) + c_5 (T, ^\circ C)^2 \right) \left( \omega_l^s \right)^2 \right];$$

$$\text{where, } c_0 = 2.343 \times 10^{-1}, c_1 = -7.924 \times 10^{-4}, c_2 = 3.924 \times 10^{-6}$$

$$c_3 = 1.06 \times 10^{-1}, c_4 = -2.0 \times 10^{-4}, c_5 = 1.2 \times 10^{-6}$$
(29)

No further corrections are made to the aqueous thermal conductivity to account for the dissolved gases (i.e., CO<sub>2</sub> and CH<sub>4</sub>).

Aqueous enthalpy was computed starting with pure liquid water enthalpy as a function of temperature and pressure from the ASME Steam Table Formulations (Meyer et al., 1993). Aqueous internal energy and enthalpy were assumed to be equal. The pure liquid water enthalpy was then corrected for salt concentration using the formulation of Michaelides (1981):

$$h_b = \left( 1 - \omega_l^s \right) h_l^w + \omega_l^s h_p^s + m_l^s \Delta h_l^s$$
(30a)

$$\Delta h_l^s = \left( \frac{4.184 \times 10^3}{10^3 + M^s m_l^s} \right) \sum_{i=0}^3 \sum_{j=0}^2 a_{i,j} (T, ^\circ C)^i \left( m_l^s \right)^j;$$

$$\text{where, } a_{0,0} = 9633.6, a_{0,1} = -4080.0, a_{0,2} = 286.49$$

$$a_{1,0} = 166.58, a_{1,1} = 68.577, a_{1,2} = -4.6856$$
(30b)

$$a_{2,0} = -0.90963, a_{2,1} = -0.36524, a_{2,2} = 0.249667 \times 10^{-1}$$

$$a_{3,0} = 0.17965 \times 10^{-2}, a_{3,1} = 0.71924 \times 10^{-3}, a_{3,2} = -0.4900 \times 10^{-4}$$

$$h_p^s = \left( \frac{4.184 \times 10^3}{M^s} \right) \sum_{k=1}^3 b_k (T, ^\circ C)^k;$$
(30c)

$$\text{where, } b_1 = -25.9293, b_2 = 0.16792, b_3 = -0.83624 \times 10^{-3}$$

The brine (saline aqueous) enthalpy was then corrected for dissolved CO<sub>2</sub> and CH<sub>4</sub>; where, the heat of solution was calculated from the partial differential of Henry's constant at constant pressure with respect to temperature (Himmelblau, 1959):

$$h_l = \left( 1 - \omega_l^a - \omega_l^o \right) h_b + \omega_l^a \left( h_g^a + \Delta h_b^a \right) + \omega_l^o \left( h_g^o + \Delta h_b^o \right)$$
(31a)

$$\Delta h_b^a = - \frac{RT^2}{M^a} \left( \frac{\partial H_b^a}{\partial T} \right)_P; \Delta h_b^o = - \frac{RT^2}{M^o} \left( \frac{\partial H_b^o}{\partial T} \right)_P$$
(31b,c)

The aqueous-phase diffusion coefficient for salt was assumed to be equal to the binary diffusion coefficient for salt in brine (saline aqueous), following the empirical equation proposed by Gordon to account for salt concentration (Reid et al., 1987):

$$D_l^s = {}^oD_l^s \left( \frac{{}^o\mu_l^w}{{}^o\mu_b} \right) \left( 1 + m_l^s \frac{\partial \ln(\gamma_l^s)}{\partial m_l^s} \right) \left( \frac{T}{{}^oT} \right) \left( \frac{{}^o\mu_b}{\mu_b} \right) \quad (32a)$$

$${}^oD_l^s = 2.254 \times 10^{-9} \frac{m^2}{s} \quad (32b)$$

$$\begin{aligned} \frac{\partial \ln(\gamma_l^s)}{\partial m_l^s} = & \left( \frac{-a_0}{\sqrt{m_l^s} (1 + \sqrt{m_l^s})} \right) + \frac{a_0}{(1 + \sqrt{m_l^s})^2} + \frac{0.06 + 0.6 a_1}{(1 + 1.5 m_l^s)^2} \\ & - 3(0.06 + 0.6 a_1) \frac{m_l^s}{(1 + 1.5 m_l^s)^3} + a_1; \end{aligned} \quad (32c)$$

where,  $a_0 = 0.2555$ ,  $a_1 = 0.0574 \frac{kg}{mol}$ ,  ${}^o\mu_l^w = 0.8904 \times 10^{-3}$ ,  ${}^oT = 298.15 K$

where, the partial derivative of the mean ionic activity coefficient of salt was computed from Bromley (1973).

The aqueous-phase diffusion coefficients for dissolved CO<sub>2</sub> and CH<sub>4</sub>, were computed from the binary diffusion coefficients for the dissolved gas in pure liquid water, ignoring the interaction with dissolved salt. For CO<sub>2</sub> the correlation of Renner (1988) was used, and for CH<sub>4</sub> the estimation method of Wilke and Chang (Reid et al. 1987) was used:

$$D_l^a = \min \left[ a_0 \left( \frac{(\mu_g^a 10^3)^{a_1}}{(\mu_l 10^3)^{a_2}} \right), 10^{-8} \right]; \text{ where, } a_0 = 6391, a_1 = 6.911, a_2 = 0.1584 \quad (33)$$

$$D_l^o = 7.4 \times 10^{-15} \frac{(2.6 M^w)^{1/2} T}{\mu_l (\bar{v}_b^o)^{0.6}}; \text{ where, } \bar{v}_b^o = 0.285 (\bar{v}_c^o)^{1.048} \quad (34)$$

The correlation of Renner (1988) was based on measurements up to 5.9 MPa at 37.8 °C. Extrapolation to the supercritical region does not yield consistent results; therefore, the correlation is limited to the experimental value obtained by Renner (1988) at the highest pressure.

### 3.7 Gas-phase thermodynamic and transport properties

The gas phase was assumed to comprise CO<sub>2</sub>, CH<sub>4</sub>, and water vapor in varying proportions. The gas-phase density was computed assuming ideal mixing from the pure component densities:

$$\rho_g = \rho_g^a + \rho_g^o + \rho_g^w \quad (35)$$

Water-vapor density was computed using the ASME Steam Table Formulations (Meyer et al., 1993); where, the water-vapor partial pressure was reduced by the salt concentration and capillary pressure. The water vapor partial pressure was computed by first computing the pure-water vapor partial pressure (*ex-situ*), using the ASME Steam Table Formulations (Meyer et al., 1993), and then correcting for salinity and capillary pressure. The correction for salinity was computed from the correlation of Haas (1976):

$$\left( P_g^w \right)_{b,ex} = P_{sat}^w \left[ T_e^w \right]_{ASME} \quad (36a)$$

$$T_e^w = \exp \left( \frac{\ln(T)}{a + bT} \right) \quad (36b)$$

$$a = \sum_{i=1}^3 a_i m_i^i; \quad (36c)$$

where,  $a_1 = 5.9358 \times 10^{-6}$ ,  $a_2 = -5.19386 \times 10^{-5}$ ,  $a_3 = 1.23156 \times 10^{-5}$

$$b = \sum_{i=1}^5 b_i m_i^i; \quad (36d)$$

where,  $b_1 = 1.15420 \times 10^{-6}$ ,  $b_2 = 1.41254 \times 10^{-7}$ ,  $b_3 = -1.92476 \times 10^{-8}$

$b_4 = -1.70717 \times 10^{-9}$ ,  $b_5 = 1.05390 \times 10^{-10}$

where the brine vapor pressure equals the pure-water vapor pressure at the equivalent pure-water temperature. The correction for capillary pressure was computed using the Kelvin equation for vapor pressure lowering (Battistelli et al. 1997):

$$P_g^w = \left( P_g^w \right)_{b,ex} \exp \left( \frac{-M_l P_{gl}}{\rho_l R T} \right) \quad (37)$$

Having established an *in-situ* water vapor partial pressure, considering the combined effects of capillary pressure and salinity, the water vapor density was then computed using the ASME Steam Table Formulations (Meyer et al., 1993), using the *in-situ* water vapor pressure and temperature.

$$\rho_g^w = \rho_g^w \left[ P_g^w, T \right]_{ASME} \quad (38)$$

The gas partial density for CO<sub>2</sub> was computed from the gas CO<sub>2</sub> partial pressure and temperature using the tabular data from Span and Wagner (1996), where the gas CO<sub>2</sub> partial pressure was a primary unknown for phase conditions without liquid CO<sub>2</sub>:

$$\rho_g^a = \rho_g^a \left[ P_g^a, T \right]_{\text{Span-Wagner}} \quad (39)$$

The gas CO<sub>2</sub> partial pressure for phase conditions with liquid CO<sub>2</sub> was the saturated vapor pressure, corrected for vapor pressure lowering with the Kelvin equation:

$$P_g^a = \left( P_g^a \right)_{ex} \exp\left( \frac{-M_n P_{gn}}{\rho_n R T} \right); \left( P_g^a \right)_{ex} = P_{sat}^a [T]_{\text{Span-Wagner}} \quad (40)$$

The gas partial density for CH<sub>4</sub> was computed from the gas CH<sub>4</sub> partial pressure and temperature using tabular data from Setzmann and Wagner (1991), where the CH<sub>4</sub> partial pressure was a primary unknown for all phase conditions:

$$\rho_g^o = \rho_g^o \left[ P_g^o, T \right]_{\text{Setzmann-Wagner}} \quad (41)$$

The gas-phase viscosity was computed by combining pure component vapor viscosities, according to the mixing rules of Wilke (Reid et al., 1987):

$$\mu_g = \frac{\chi_g^a \mu_g^a}{\chi_g^a + \chi_g^o \varphi_g^{oa} + \chi_g^w \varphi_g^{wa}} + \frac{\chi_g^o \mu_g^o}{\chi_g^a \varphi_g^{ao} + \chi_g^o + \chi_g^w \varphi_g^{wo}} + \frac{\chi_g^w \mu_g^w}{\chi_g^a \varphi_g^{aw} + \chi_g^o \varphi_g^{ow} + \chi_g^w} \quad (42a)$$

$$\varphi_g^{ij} = \frac{\left[ 1 + \left( \frac{\mu_g^i}{\mu_g^j} \right)^{1/2} \left( \frac{M^j}{M^i} \right)^{1/4} \right]^2}{\left[ 8 \left( 1 + \frac{M^i}{M^j} \right) \right]^{1/2}} \quad (42b)$$

The water vapor viscosity was computed from the *in-situ* water vapor partial pressure and temperature using the ASME Steam Table Formulations (Meyer et al., 1993):

$$\mu_g^w = \mu_g^w \left[ P_g^w, T \right]_{\text{ASME}} \quad (43)$$

The CO<sub>2</sub> vapor viscosity was computed from the CO<sub>2</sub> component vapor density and temperature using the correlation of Fenghour et al. (1998), as described in Equation (18). The CH<sub>4</sub> vapor viscosity was computed from the CH<sub>4</sub> component density and temperature using the correlations of Kiselev and Huber (1998), as described in Equation (19).

Gas phase thermal conductivity was computed from the pure component vapor thermal conductivities using the modifications of Mason and Saxena to the Waasiljewa equation mixing equation (Reid et al., 1987):

$$k_g = \frac{\chi_g^a k_g^a}{\chi_g^a + \chi_g^o \phi_g^{oa} + \chi_g^w \phi_g^{wa}} + \frac{\chi_g^o k_g^o}{\chi_g^a \phi_g^{ao} + \chi_g^o + \chi_g^w \phi_g^{wo}} + \frac{\chi_g^w k_g^w}{\chi_g^a \phi_g^{aw} + \chi_g^o \phi_g^{ow} + \chi_g^w} \quad (44a)$$

$$\phi_g^{ij} = \frac{\left[ 1 + \left( \frac{\lambda_g^i}{\lambda_g^j} \right)^{1/2} \left( \frac{M^j}{M^i} \right)^{1/4} \right]^2}{\left[ 8 \left( 1 + \frac{M^i}{M^j} \right) \right]^{1/2}} \quad (44b)$$

$$\frac{\lambda_g^i}{\lambda_g^j} = \frac{\Gamma_g^i \left[ \exp \left( 0.0464 \frac{T}{T_c^i} \right) - \exp \left( -0.2412 \frac{T}{T_c^i} \right) \right]}{\Gamma_g^j \left[ \exp \left( 0.0464 \frac{T}{T_c^j} \right) - \exp \left( -0.2412 \frac{T}{T_c^j} \right) \right]} \quad (44c)$$

$$\Gamma_g^i = 210 \left( \frac{T_c^i (M^i)^3}{(P_c^i)^4} \right)^{1/6} \quad (44d)$$

The water vapor thermal conductivity was computed from the *in-situ* water vapor partial pressure and temperature using the ASME Steam Table Formulations (Meyer et al., 1993):

$$k_g^w = k_g^w \left[ P_g^w, T \right]_{ASME} \quad (45)$$

The CO<sub>2</sub> vapor thermal conductivity was computed from the CO<sub>2</sub> component vapor density and temperature using bilinear interpolation of the correlation of Vesovic et al. (1990). The CH<sub>4</sub> vapor thermal conductivity was computed using the correlation of Kiselev et al. (1998), as described in Equation (20).

Gas phase enthalpy and internal energy were computed from pure component vapor enthalpies using mass fraction weighting, ignoring the enthalpy of formation:

$$h_g = \omega_g^a h_g^a + \omega_g^o h_g^o + \omega_g^w h_g^w \quad (46a)$$

$$u_g = \omega_g^a u_g^a + \omega_g^o u_g^o + \omega_g^w u_g^w \quad (46b)$$

Water vapor enthalpy and internal energy were computed from the *in-situ* water vapor partial pressure and temperature using the ASME Steam Table Formulations (Meyer et al., 1993):

$$h_g^w = h_g^w [P_g^w, T]_{ASME} \quad (47a)$$

$$u_g^w = h_g^w - \frac{P_g^w}{\rho_g^w} \quad (47b)$$

CO<sub>2</sub> and CH<sub>4</sub> vapor enthalpy and internal energy were computed from the CO<sub>2</sub> and CH<sub>4</sub> vapor partial pressure and temperature using the tabular data from Span and Wagner (1996) and Setzmann and Wagner (1991), respectively:

$$h_g^a = h_g^a [P_g^a, T]_{Span-Wagner}; \quad h_g^o = h_g^o [P_g^o, T]_{Setzmann-Wagner} \quad (48a,b)$$

$$u_g^a = u_g^a [P_g^a, T]_{Span-Wagner}; \quad u_g^o = u_g^o [P_g^o, T]_{Setzmann-Wagner} \quad (48c,d)$$

Gas phase diffusion coefficients were calculated from binary diffusion coefficients following Blanc's law (Reid et al., 1987):

$$D_g^o = \left( \frac{\chi_g^a}{D_g^{oa}} + \frac{\chi_g^w}{D_g^{ow}} \right)^{-1}; \quad D_g^a = \left( \frac{\chi_g^o}{D_g^{ao}} + \frac{\chi_g^w}{D_g^{aw}} \right)^{-1}; \quad D_g^w = \left( \frac{\chi_g^a}{D_g^{wa}} + \frac{\chi_g^o}{D_g^{wo}} \right)^{-1} \quad (49a,b,c)$$

Vapor binary diffusion coefficients for component pairs were computed using the Wilke and Lee correlations (Reid et al., 1987):

$$D_g^{ij} = \frac{\left[ 3.03 - \left( \frac{0.98}{(M^{ij})^{1/2}} \right) \right] 10^{-2} T^{3/2}}{P (M^{ij})^{1/2} (\sigma^{ij})^2 \Omega_D}; \quad \text{where, } M^{ij} = 2 \left[ \left( 1/M^i \right) + \left( 1/M^j \right) \right] \quad (50a,b)$$

$$\sigma^{ij} = \frac{1.18 (\bar{v}_b^i)^{1/3} + 1.18 (\bar{v}_b^j)^{1/3}}{2}; \quad \text{where, } \bar{v}_b^i = 0.285 (\bar{v}_c^i)^{1.048} \quad (50c,d)$$

$$\Omega_D = \frac{a_0}{(T_r)^{a_1}} + \frac{a_2}{\exp(a_3 T_r)} + \frac{a_4}{\exp(a_5 T_r)} + \frac{a_6}{\exp(a_7 T_r)};$$

$$\text{where, } T_r = \frac{kT}{\varepsilon^{ij}}, \varepsilon^{ij} = (\varepsilon^i \varepsilon^j)^{1/2}, \varepsilon^i = 1.15 T_b^i k \quad (50\text{e,f,g,h})$$

$$a_0 = 1.06036, a_1 = 0.15610, a_2 = 0.19300, a_3 = 0.47635$$

$$a_4 = 1.03587, a_5 = 1.52996, a_6 = 1.76474, a_7 = 3.89411$$

### 3.8 Ice saturation

Ice is assumed to be totally occluded by the aqueous phase and occur in pore radii smaller than hydrate. With this conceptual model as a basis, the ice saturation was computed from the pressure difference across the ice-aqueous interface; where, the ice-aqueous pressure difference was computed from the ice-aqueous radius of curvature:

$$(P_i - P_l) = \frac{\xi_{il} \sigma_{il} \cos(\theta_{il})}{r_{il}} \quad (51)$$

As with the hydrate-aqueous interface, assuming the shape factor equals 2 (spherical contact) and the contact angle equals 0, then Equation (51) can be simplified:

$$(P_i - P_l) = \frac{2 \sigma_{il}}{r_{il}} \quad (52)$$

There is a known hysteresis in the freezing and melting point of water in porous media (Klauda and Sandler, 2001). The ice-aqueous radius of curvature for freezing and melting conditions was computed using the correlations of Brun et al. (1977) for water:

$$r_{il} = \frac{64.67 \times 10^{-9}}{(T_{fp}^{ex} - T_{fp}^{in})} + 0.57 \times 10^{-9} \{ \text{freezing conditions} \} \quad (53a)$$

$$r_{il} = \frac{64.67 \times 10^{-9}}{2(T_{fp}^{ex} - T_{fp}^{in})} + 0.685 \times 10^{-9} \{ \text{melting conditions} \} \quad (53b)$$

These equations indicate an incremental temperature increase is required to melt ice within a porous media. Under conditions where the ice-aqueous radius is smaller than the hydrate-aqueous radius, then ice saturation occurs, using the ice-aqueous capillary pressure in the user-specified soil moisture retention function. Upon freezing ice was assumed to occur in the largest pore spaces occupied by aqueous phase, and upon melting ice disappears from the smallest pore spaces occupied by ice.

### 3.9 Ice thermodynamic and transport properties

The density of ice was computed as a function of temperature from a polynomial correlation (ASHRAE, 1977):

$$\rho_i = \left( \sum_{i=0}^2 a_i T^i \right)^{-1}; \text{ where,} \quad (54)$$

$$a_0 = 1.06472 \times 10^{-3}, a_1 = 1.23173 \times 10^{-8}, a_2 = 3.0203 \times 10^{-10}$$

The thermal conductivity of ice was computed as a function of temperature from a polynomial correlation (Dickerson, 1969):

$$k_i = \sum_{i=0}^2 a_i T^i; \text{ where,} \quad (55)$$

$$a_0 = 7.39519, a_1 = -2.86936 \times 10^{-2}, a_2 = 3.54452 \times 10^{-5}$$

Ice enthalpy was computed from a polynomial fit from tabular data (ASHRAE, 1977) that included the heat of dissociation:

$$h_i = \sum_{i=0}^2 a_i T^i; \text{ where, } a_0 = -6.36443 \times 10^5, a_1 = 1.14468 \times 10^2, a_2 = 3.64104 \quad (56)$$

#### 4. Numerical solution

The five governing conservation equations for component mass and thermal energy were discretized following the integrated finite difference technique of Patankar (1980), which is locally and globally conserving. In brief the Patankar scheme uses first-order spatial differencing and fully implicit temporal differencing. Details of the discretization are described in the STOMP Theory Guide (White and Oostrom, 2000). The discretization process transforms governing conservation equations from nonlinear partial differential equations to nonlinear algebraic equations. Nonlinearities in the algebraic equations were resolved using multivariable Newton-Raphson iteration, details of which are described in the STOMP Theory Guide (White and Oostrom, 2000). The Newton-Raphson solution scheme is iterative and requires the construction of a Jacobian matrix, which comprises partial differentials of the residuals of the algebraic forms of the discretized governing conservation equations with respect to the primary variables. The partial derivatives that compose the Jacobian matrix are computed using numerical differentiation. A critical requirement for the solution scheme is that the primary variable set define the system (i.e., all secondary variables must be mathematically dependent on the primary variables through the constitutive relations). To account for phase appearances, disappearances, and transitions, a primary variable switching scheme is employed; where, the primary variable set is allowed to switch between Newton-Raphson iterations.

#### 5. Numerical studies

#### 6. Discussion

## 7. Acknowledgements

### Nomenclature

#### Roman

$c_p$  specific heat, J/kg K

$D_l^a$  aqueous molecular diffusion coefficient for CO<sub>2</sub>, m<sup>2</sup>/s

$D_l^o$  aqueous molecular diffusion coefficient for CH<sub>4</sub>, m<sup>2</sup>/s

$\mathbf{D}_\gamma^\xi$  diffusion-dispersion tensor of component  $\zeta$  in phase  $\gamma$ , m<sup>2</sup>/s

$\mathbf{F}_\gamma$  advective mass flux vector in phase  $\gamma$ , kg/s m<sup>2</sup>

$g$  acceleration of gravity, (9.81 m/s<sup>2</sup>)

$h$  enthalpy, J/kg

$h_b$  enthalpy of brine (saline aqueous), J/kg

$h_o^a$  reference enthalpy of CO<sub>2</sub> for hydrate dissociation (-21.89891 x 10<sup>3</sup> J/kg)

$h_o^o$  reference enthalpy of CH<sub>4</sub> for hydrate dissociation (-56.10314 x 10<sup>3</sup> J/kg)

$h_o^w$  reference water enthalpy for hydrate dissociation (1.0 J/kg)

$h_p^s$  precipitated salt enthalpy, J/kg

$\Delta h_b^a$  enthalpy of solution of CO<sub>2</sub> in brine (saline aqueous), J/kg

$\Delta h_b^o$  enthalpy of solution of CH<sub>4</sub> in brine (saline aqueous), J/kg

$\Delta h_l^s$  enthalpy of mixing of salt in liquid water, J/kg

$\mathbf{J}_\gamma^\xi$  diffusive mass flux vector of component  $\zeta$  in phase  $\gamma$ , kg/s m<sup>2</sup>

$\mathbf{k}_e$  equivalent thermal conductivity tensor, W/m K

$k_h$  thermal conductivity of hydrate phase, W/m K

$\mathbf{k}_i$  intrinsic permeability tensor, m<sup>2</sup>

$k^o$  thermal conductivity of CH<sub>4</sub> vapor, W/m K

$k_o^o$  zero-density-limit portion thermal conductivity of CH<sub>4</sub> vapor, W/m K

$k_e^o$  excess portion of the thermal conductivity of CH<sub>4</sub> vapor, W/m K

$k_{r\gamma}$  relative permeability of phase  $\gamma$

$\dot{m}$  phase mass source rate, kg/s

$m_l^a$  molality of CO<sub>2</sub> in aqueous phase, mol/kg

$m_l^o$  molality of CH<sub>4</sub> in aqueous phase, mol/kg  
 $M$  molecular weight, kg/kmol  
 $N$  Avagadro's number (6.023 x 10<sup>23</sup> molecules/mole)  
 $n_h^w$  hydration number (i.e., molecules water per molecule hydrate former)  
 $P_\gamma$  pressure of phase  $\gamma$ , Pa  
 $P_{gl}$  gas-aqueous capillary pressure, Pa  
 $P_{gn}$  gas-liquid CO<sub>2</sub> capillary pressure, Pa  
 $P_n^c$  critical liquid CO<sub>2</sub> pressure, Pa  
 $\dot{q}$  energy source rate, J/s  
 $r_{hl}$  radius of curvature for the hydrate-aqueous interface, m  
 $s$  phase saturation  
 $\bar{s}$  effective phase saturation  
 $\bar{\bar{s}}$  apparent phase saturation  
 $s_{lr}$  aqueous residual saturation  
 $t$  time, s  
 $T$  temperature, K  
 $T_c^a$  critical temperature of CO<sub>2</sub> (304.1 K)  
 $T_c^o$  critical temperature of CH<sub>4</sub> (190.564 K)  
 $T_e^w$  equivalent pure water temperature, K  
 $T_o$  reference temperature for hydrate dissociation (273.15 K)  
 $u$  internal energy, J/kg  
 $v^w$  vapor saturated specific volume of liquid water, cm<sup>3</sup>/gm  
 $\bar{v}_b^o$  molar volume of CH<sub>4</sub> at normal boiling point, cm<sup>3</sup>/mol  
 $\bar{v}_c^o$  critical molar volume of CH<sub>4</sub>, cm<sup>3</sup>/mol  
 $\bar{v}_l^a$  partial molar volume of CO<sub>2</sub> in aqueous phase, m<sup>3</sup>/kmol  
 $\bar{v}_l^o$  partial molar volume of CH<sub>4</sub> in aqueous phase, m<sup>3</sup>/kmol  
 $y$  hydrate cage occupancy (i.e., fractional filling of cage)  
 $\mathbf{z}_g$  gravitational unit vector  
  
*Greek*  
 $\beta$  fluid-pair scaling factor  
 $\partial$  differential operator  
 $\theta_{hl}$  hydrate-aqueous interfacial contact angle, rad

$\xi_{hl}$  hydrate-aqueous interfacial shape factor (2.0)  
 $\phi$  porosity  
 $\mu_b$  brine (saline aqueous viscosity), Pa s  
 $\mu_e^a$  excess portion of the dynamic viscosity of CO<sub>2</sub>, Pa s  
 $\mu_e^o$  excess portion of the dynamic viscosity of CH<sub>4</sub>, Pa s  
 $\mu_l^w$  pure liquid water viscosity, Pa s  
 $\mu_0^a$  zero-density-limit portion of the dynamic viscosity of CO<sub>2</sub>, Pa s  
 $\mu_0^o$  zero-density-limit portion of the dynamic viscosity of CH<sub>4</sub>, Pa s  
 $\mu_\gamma$  dynamic viscosity of phase  $\gamma$ , Pa s  
 $\rho_b$  brine (saline aqueous) density, kg/m<sup>3</sup>  
 $\rho_\gamma$  density of phase  $\gamma$ , kg/m<sup>3</sup>  
 $\bar{\rho}^o$  molar density of CH<sub>4</sub>, mol/L  
 $\bar{\rho}_c^o$  critical molar density of CH<sub>4</sub>, (10.08 mol/L)  
 $\sigma$  fluid-pair interfacial tension, N/m  
 $\sigma_{hl}$  hydrate-aqueous interfacial tension, N/m  
 $\sigma_{ref}$  reference fluid-pair interfacial tension, N/m  
 $\tau_\gamma$  tortuosity factor of phase  $\gamma$   
 $\omega_\gamma^\xi$  mass fraction of component  $\xi$  in phase  $\gamma$   
 $\chi_\gamma^\xi$  mole fraction of component  $\xi$  in phase  $\gamma$   
 $\bar{\chi}_g^o$  mole fraction of CH<sub>4</sub> in gas phase, excluding water  
 $\psi_{ref}$  reference fluid pair entry pressure, Pa  
 $\nabla$  gradient operator, 1/m

*Subscripts*

$g$  gas phase  
 $gl$  gas-aqueous fluid pair  
 $gn$  gas-liquid CO<sub>2</sub> fluid pair  
 $h$  hydrate phase  
 $hl$  hydrate-aqueous fluid pair  
 $i$  ice phase  
 $l$  aqueous phase  
 $L$  large cage  
 $n$  liquid CO<sub>2</sub> phase (nonaqueous phase liquid)

*nl* liquid CO<sub>2</sub>-aqueous fluid pair  
*p* precipitated salt phase  
*S* small cage  
*t* total-liquid  
 $\gamma$  phase indicator

#### *Superscripts*

*a* CO<sub>2</sub> component  
*ex* *ex-situ* (i.e., laboratory conditions)  
*in* *in-situ* (i.e., porous media conditions)  
*o* CH<sub>4</sub> component  
*s* salt component  
*w* water component  
 $\zeta$  component indicator

#### **References**

Andersen, G., Probst, A., Murray, L., Butler, S., 1992. An accurate PVT model for geothermal fluids as represented by H<sub>2</sub>O-CO<sub>2</sub>-NaCl mixtures. In Proceedings of Seventeenth Workshop on Geothermal Reservoir Engineering, Stanford University, Stanford, California.

ASHRAE, 1977. ASHRAE Handbook, 1977 Fundamentals. American Society of Heating, Refrigerating, and Air-Conditioning Engineers, Inc., 345 East 47th Street, New York, NY 10017.

Battistelli, A., Calore, C., Pruess, K., 1997. The simulator TOUGH2/EWASG for modelling geothermal reservoirs with brines and noncondensable gas. *Geothermics*. 26(4),437-464.

Bromley, L. A., 1973. Thermodynamic properties of strong electrolytes in aqueous solutions. *AIChE*. 19(2),313-320.

Brooks, R. H., Corey, A. T., 1964. Hydraulic Properties of Porous Media. Colorado State University, Hydrology Paper, No. 3, Fort Collins, Colorado.

Brun, M., Lallemand, A., Quinson, J. F., Eyraud, C., 1977. A new method for the simultaneous determination of the size and shape of pores: The thermoporometry. *Thermochimica Acta*. 21(1):59-88.

Clennell, M. B., Hovland, M., Booth, J. S., Henry, P., Winters, W. J., 1999. Formation of natural gas hydrates in marine sediments 1. Conceptual model of gas hydrate growth conditioned by host sediment properties. *Journal of Geophysical Research*. 104 (B10), 22,985-23,003.

Collett, T. S., 1993. Natural gas hydrates of the Prudhoe Bay and Kuparuk River Area, North Slope, Alaska. *The American Association of Petroleum Geologists Bulletin*. 77 (5), 793-812.

Dickerson, R. W., Jr., 1969. Thermal Properties of Food in The Freezing Preservation of Foods, 4<sup>th</sup> Edition, Volume 2, Tressler, D. K, van Arnsdel, W. B., Copley, M. J., Editors, AVI Publishing Co., Westport, CN.

Fenghour, A., Wakeman, W. A., Vesovic, V., 1998. The viscosity of carbon dioxide. *J. Phys. Chem. Ref. Data*. 27(1),31-41.

Haas Jr., J. L., 1976. Physical Properties of the Coexisting Phases and Thermochemical Properties of the H<sub>2</sub>O Component in Boiling NaCl Solutions: Preliminary Steam Tables for NaCl Solutions. Geological Survey Bulletin 1421-A, U. S. Geological Survey.

Handa, Y. P., 1986. Compositions, enthalpies of dissociation, and heat capacities in the range 85 to 270K for clathrate hydrates of methane, ethane, and propane, and enthalpy of dissociation of isobutane hydrate as determined by a heat-flow calorimeter. J. Chem. Thermodynamics. 18,915-921.

Haverkamp, R., Vauclin, M., Touma, J., Wierenga, P. J., Vachaud, G, 1977. A comparison of numerical simulation models for one-dimensional infiltration. Soil Sci. Soc. Am. J. 41,285-294.

Himmelblau, D. M., 1959. Partial molal heats and entropies of solution for gases dissolved in water from the freezing to near critical point. Journal of Physical Chemistry. 63,1803-1808.

Kiselev, S. B., Huber, M. L, 1998. Transport properties of carbon dioxide + ethane and methane + ethane mixtures in the extended critical region. Fluid Phase Equilibria. 142,253-280.

Klauda, J. B., Sandler, S. I., 2001. Modeling gas hydrate phase equilibria in laboratory and natural porous media. Ind. Eng. Chem. Res. 40,4197-4208.

Klauda, J. B., Sandler, S. I.. 2003. Phase behavior of clathrate hydrates: a model for single and multiple gas component hydrates. Chemical Engineering Science. 58,27-41.

McKibbin, R., McNabb, A., 1993. Modeling the phase boundaries and fluid properties of the system H<sub>2</sub>O-NaCl at high temperatures and pressures. Proceedings 15th NZ Geothermal Workshop, University of Auckland, New Zealand.

Meyer, C. A., McClintock, R. B., Silvestri, G. J., Spencer, R. C., 1993. ASME Steam Tables, The American Society of Mechanical Engineers, New York.

Michaelides, E. E., 1981. Thermodynamic properties of geothermal fluids. Geothermal Resources Council Transactions. 5,361-364.

Ozbek, H., Phillips, S. L., 1980. Thermal conductivity of aqueous sodium chloride solutions from 20 to 330 C. J. Chem. Engr. Data. 25,263-267.

Patankar, S. V., 1980. Numerical heat transfer and fluid flow. Hemisphere Publishing Corporation, Washington, D.C.

Phillips, S. L., Igbene, A., Fair, J. A., Ozbek, H., Tavana, M., 1981. A Technical Databook for Geothermal Energy Utilization. Lawrence Berkeley Laboratory, University of California, LBL-12810, UC-66a, Berkeley, California.

Reid, R. C., Prausnitz, J. M., Poling, B. E., 1987. The Properties of Gases & Liquids. McGraw-Hill Book Company, New York.

Renner, T. A., 1988. Measurement and correlation of diffusion coefficients for CO<sub>2</sub> and rich-gas applications. SPE Reservoir Engineering. 517-523.

- Setzmann, U., Wagner, W., 1991. A new equation of state and tables of thermodynamic properties for methane covering the range from melting line to 625 K at pressures up to 1000 MPa. *J. Phys. Chem. Ref. Data.* 20(6),1061-155.
- Sloan, E. D., Jr., 1997. *Clathrate Hydrates of Natural Gases.* Marcel Dekker, Inc., New York.
- Sloan, E. D., Jr., 2000. Clathrate hydrates: The other common solid water phase. *Ind. Eng. Chem. Res.* 39,3123-3129.
- Span, R., Wagner, W., 1996. A new equation of state for carbon dioxide covering the fluid region from the triple-point temperature to 1100 K at pressures up to 800 MPa. *J. Phys. Chem. Ref. Data.* 25(6),1509-1596.
- Turner, D. J., Sloan, E. D., Jr. 2002. Hydrate phase equilibria measurements and predictions in sediments. In *Proceedings of 4th International Conference on Gas Hydrates, Yokohama, Japan.*
- van Genuchten, M. T. A., 1980. A closed-form equation for predicting the hydraulic conductivity of unsaturated soils. *Soil Sci. Soc. Am. J.* 44,892-898.
- Verma, A., Pruess, K., 1988. Thermohydrological conditions and silica redistribution near high-level nuclear waste emplaced in saturated geological formations. *Journal of Geophysical Research.* 93(B2),1159-1173.
- Vesovic, V., Wakeman, W. A., Olchoway, G. A., Sengers, J. V., Watson, J. T. R., Millat, J., 1990. The transport properties of carbon dioxide. *J. Phys. Chem. Ref. Data.* 19(3),763-808.
- Waite, W. F., deMartin, B. J., Kirby, S. H., Pinkston, J., Ruppel, C. D., 2002. Thermal conductivity measurements in porous mixtures of methane hydrate and quartz sand. *Geophysical Research Letters.* 29,2229.
- White, M. D., Oostrom, M., 2000. *STOMP Subsurface Transport Over Multiple Phases, Version 2.0, Theory Guide.* Pacific Northwest National Laboratory, PNNL-12030, UC-2010, Richland, Washington.
- Yoon, J., Yamamoto, Y., Komai, T., Haneda, H., 2003. Rigorous approach to the prediction of the heat of dissociation of gas hydrates. *Ind. Eng. Chem. Res.* 42,1111-1114.

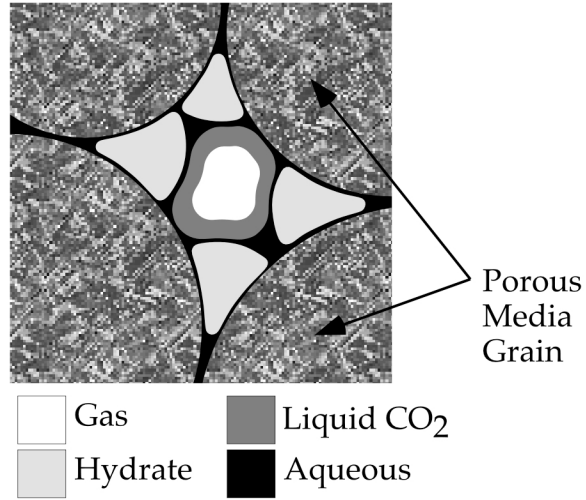


Fig. 1. Conceptual model for pore-space phase distribution.

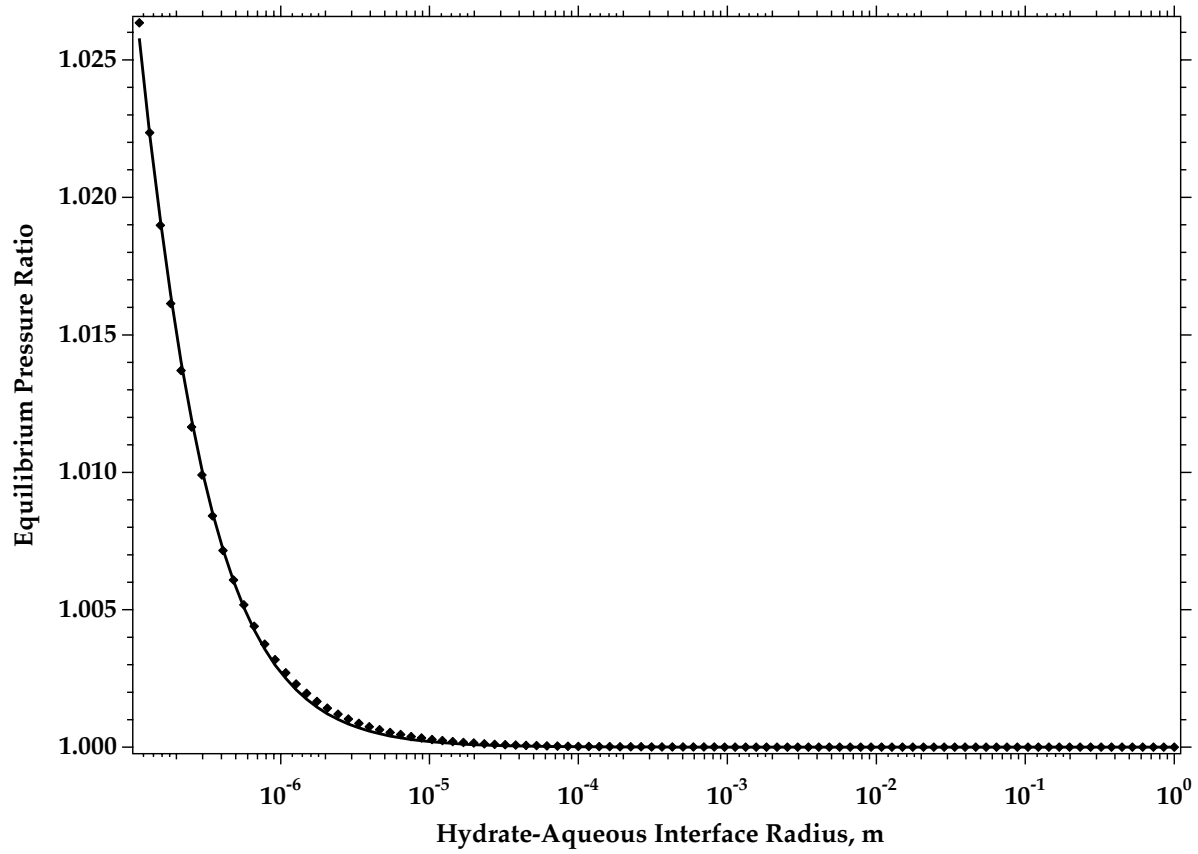


Fig. 2. Equilibrium pressure ratio versus pore radius

## **National Energy Technology Laboratory**

626 Cochrans Mill Road  
P.O. Box 10940  
Pittsburgh, PA 15236-0940

3610 Collins Ferry Road  
P.O. Box 880  
Morgantown, WV 26507-0880

One West Third Street, Suite 1400  
Tulsa, OK 74103-3519

1450 Queen Avenue SW  
Albany, OR 97321-2198

2175 University Ave. South  
Suite 201  
Fairbanks, AK 99709

Visit the NETL website at:  
[www.netl.doe.gov](http://www.netl.doe.gov)

Customer Service:  
1-800-553-7681

